DRES

DEFENCE RESEARCH ESTABLISHMENT SUFFIELD

CR 98-31

UNCLASSIFIED

Computational Study of Supersonic Combustion Phenomena

BY:

Paul Thibault & John Penrose
Combustion Dynamics Ltd.

SUBMITTED TO:
SCIENTIFIC AUTHORITY

John Slater
Defence Research Establishment Suffield
Box 4000, Medicine Hat, Alberta, T1A 8K6

June 1998

WARNING

"The use of this information is permitted subject to recognition of proprietary and patent rights."

CRAD

National Defence Défense nationale

Canada

102-02546/

CDL

COMPUTATIONAL STUDY OF SUPERSONIC COMBUSTION PHENOMENA

R7-
Contract No. W7702-[redacted]298/01-XSG

June 1998

Combustion Dynamics Ltd.

Computational Study of Supersonic Combustion Phenomena, Phase I

W7702-R7-298

Final Report

30 June 1998

Combustion Dynamics Ltd.

1.0 Introduction

This report summarizes the work performed under the contract entitled "Computational Study of Supersonic Combustion Phenomena, Phase I" sponsored by DRES with Dr. Denis Bergeron as Scientific Authority. The main objective of this contract was to provide computational tools for the modelling of supersonic combustion phenomena related to detonation driven projectiles. Work performed under this contract included:

- Calculations for a novel detonation-driven projectile,
- Implementation of complex 2-D and 3-D slanted boundary algorithms in IFSAS,
- Implementation of combustion models in IFSAS,
- Development of a prototype code for gas dynamic and combustion calculations.

This report summarizes the software development performed under this contract along with subsequent developments made possible from contracts from CDL funding and other sources.

2.0 Detonation Driven Projectile Calculations

This work involved computations for a free-flying hollow detonation-driven projectile. The motivation for this work is to develop a nozzle geometry that could eventually be used to model a detonation driven engine. The approach consists of using the imploding bow shock from the leading edge to initiate a detonation. Positive thrust is achieved by stabilizing the detonation downstream of the nozzle throat. Parametric studies were performed to investigate the role of projectile geometry, the inlet Mach number and surface friction on the stabilization of the detonation front. This work, performed in collaboration with DRES and McGill University, resulted in four papers [1-4] and one US patent.

3.0 Implementation of 2-D Slanted Boundary Algorithms

This work involved the implementation of a slanted boundary algorithm in IFSAS to allow free-slip conditions for surfaces not aligned with the grid. This approach is required for a large number of applications to accurately resolve oblique shock reflections and to prevent the artificial ignition of a combustible gas at stagnation points created by a "staircase" representation of an oblique boundary. The latter concern is of particular importance for detonation driven projectile calculations.

3.1 Brief description of method

The governing Euler equations were solved using a second order Lax-Wendroff Finite Difference scheme in conjunction with the 6th order (phase error) of the Flux Corrected Transport (FCT) algorithm. As shown in Figure 1, the solution is on a fixed rectangular mesh and uses a "slanted boundary" algorithm for solid boundaries that are not aligned with the grid. This algorithm maintains free-slip conditions in the direction tangent to the boundary and solves the Riemann problem for the normal component.

The overall solution method uses a "split" algorithm which constructs a 2-D solution through separate sweeps in the x and y directions. The intersection of the slanted boundary with a rectangular grid can introduce computational cells that are significantly smaller than the "standard" cells away from the boundary. This can result in very small time steps due to the explicit nature of the finite difference scheme. As illustrated in Figure 1, this problem is eliminated by merging the small end cell with the neighbouring cell in the vertical and horizontal direction.

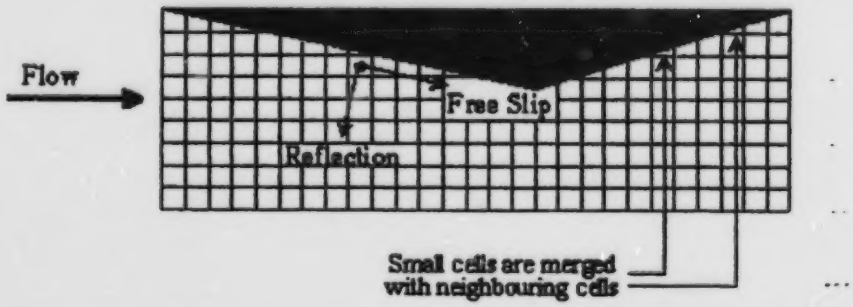

Figure 1. Slanted boundary algorithm for Eulerian Grid calculations

3.2 Test case CFD94

The slanted boundary algorithm was tested based on experiments performed at UTIAS. The experiment, which involves the diffraction of a shock with a double wedge, was used as a benchmark problem for the CFD94 conference in Toronto. The figures below show the excellent agreement between the experimental interferograms and the contour plots computed with the Lax Wendroff/FCT scheme and the slanted boundary algorithm.

Figure 2: Comparison of computed and experimental results for CFD94 problem

3.3 Complex flow

The slanted boundary algorithm can be used for very complex geometries involving a combination of shapes such as lines, ellipses, rectangles, triangles and polygons. The shapes in IFSAS are extremely versatile and can be used to define rigid or deformable solids or a fluid "cloud" with a predefined thermodynamic state defined in the STATE module. "Cut-out" shapes can be defined by inserting a cloud shape with a state corresponding to that of the ambient fluid. Figure 3 illustrates the use of the slanted boundary algorithm with the IFSAS primitives. The use of these primitives is fully documented in the IFSAS on-line Graphical Help System and the Reference and User Manuals [5,6] distributed to DRES personnel at the IFSAS/SuperSTATE course in October 1997.

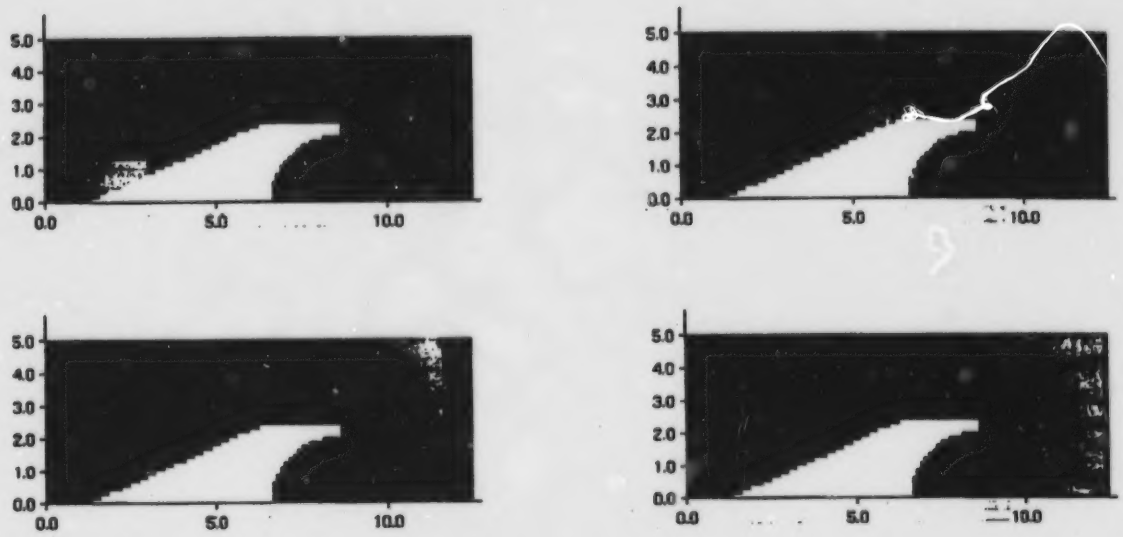

Figure 3: Use of IFSAS primitives to define complex 2-D shape (barrier problem in course); distance in metres

3.4 New Developments

Since the completion of this contract, the 2-D slanted boundary algorithm has been extended to interact with moving and deformable structures, static and dynamic grid refinement, and shock trackers.

CDL computations performed with 2-D deformable structures include the work of Tran et al. [8] and Link et al. [9] presented at CFD94 and CFD95 respectively. Tran et al. presented calculations for an underwater shock interacting with a deformable cylinder and an air-filled shell. Link et al. presented results for the propulsion of cylindrical venting panels by a fuel-air explosion. As shown in Figure 4, which displays results for a shock interacting with an air-filled rectangular box, the 2-D FSI capabilities in IFSAS can deal with large structural deformations.

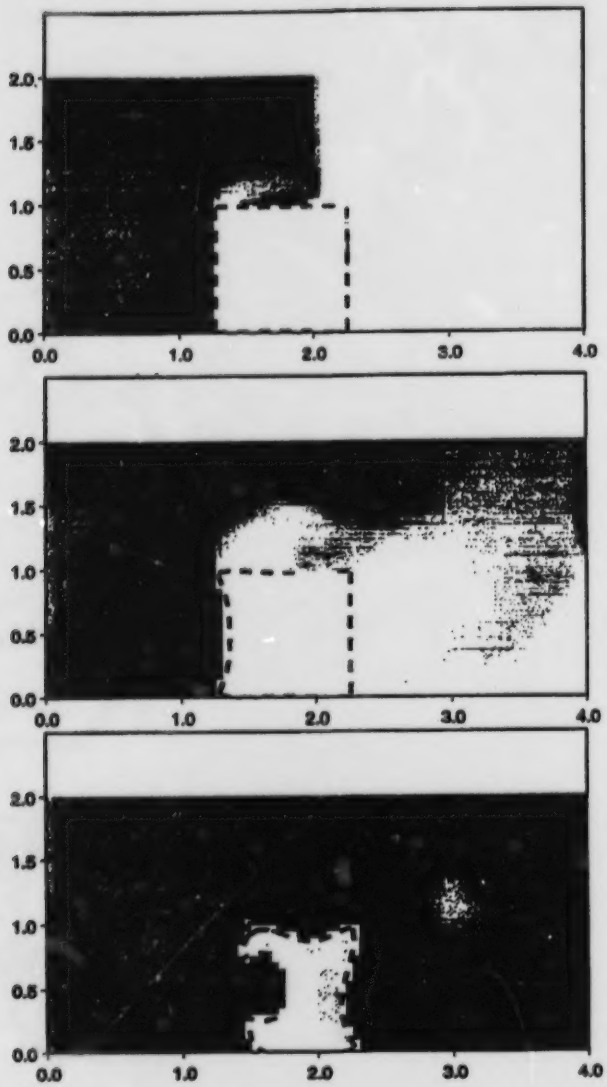

Figure 4: FSI calculations for a shock interacting with an air-filled rectangular box (distance in metres)

CDL has implemented the slanted boundary algorithm in the cell-based adaptive gridding scheme. This scheme presented in the CFD95 paper by Zhang et al. [10], uses a 2nd order Godunov scheme with a quadtree (2-D) or octree (3-D) data structure. More recently, Hawken et al. [11] extended this work to combine the slanted boundary and adaptive gridding scheme with a level set font tracking/reconstruction algorithm developed by Smiljanivski et al. [12] and Moser et al. [13]. Figure 5a displays the results obtained with these combined advanced algorithms for a shock interacting with a wedge. Figure 5b displays the experimental results obtained by Deschambault and Glass [14] for the same configuration.

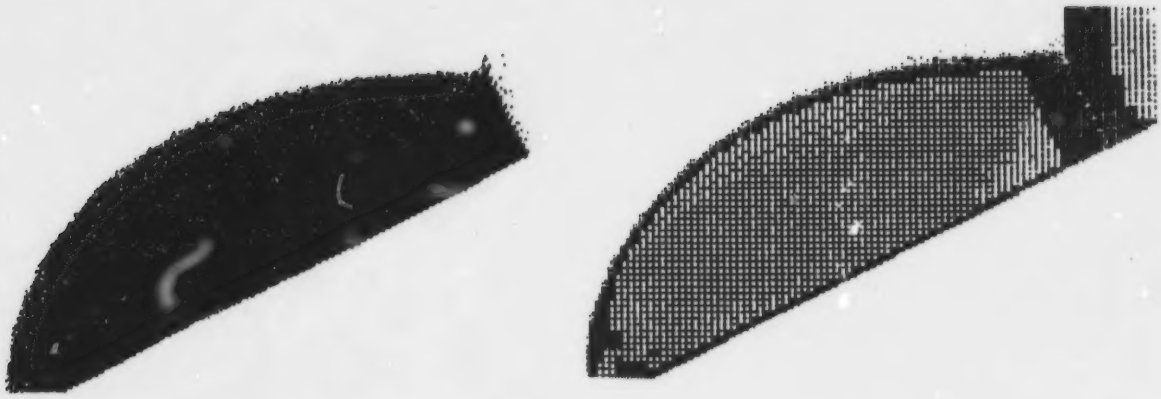

Figure 5a: Computational results for a shock interacting with a wedge (shock tracking and adaptive gridding)

Figure 5b: Experimental results for a shock interacting with a wedge

4.0 Implementation of 3-D Slanted Boundaries

4.1 3-D Primitives

The algorithm described above for 2-D shapes was extended to accommodate 3-D geometries. As in the case of 2-D shapes, complex 3-D shapes can be constructed using primitives such as blocks, ellipsoids, cones, cylinders and bodies of revolution based on a 2-D shape. The use of these primitives is discussed in the IFSAS Reference Manual, User Manual and on-line Help System. Figure 5 displays results for a complex 3-D blast barier constructed from these primitives.

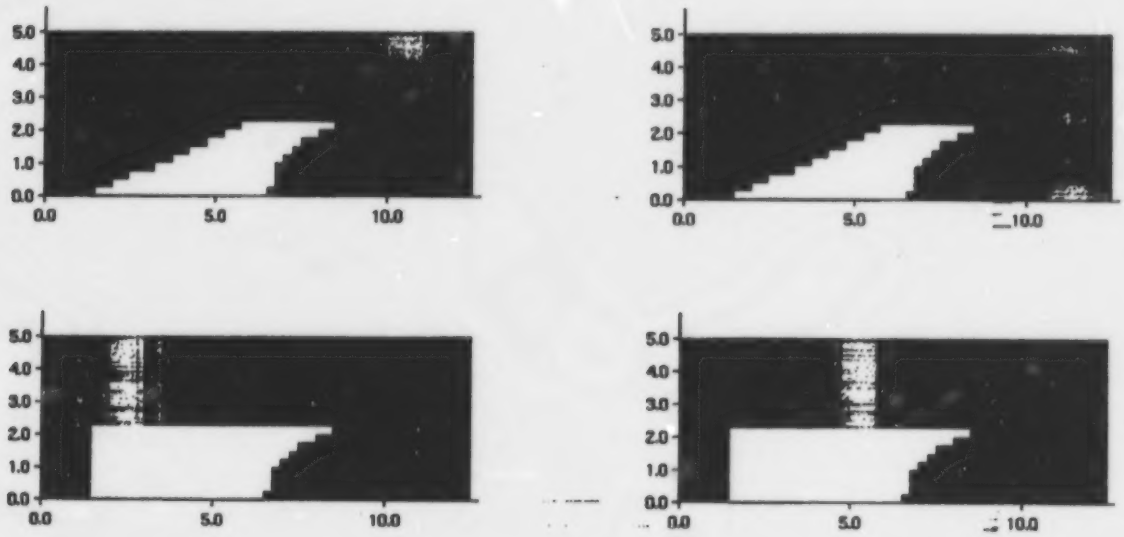

Figure 6: Shock interacting with a 3-D barrier (distance in metres)

4.2 New Developments

The 3-D slanted boundary algorithm has been extended to accommodate moving and deformable structures and adaptive grids. Results for 3-D Fluid-Structure Interaction (FSI) calculations have been presented by Link et al. [9] for an underwater shock interacting with an underwater spherical explosion. These calculations were performed using the 3-D Lax-Wenfroff/FCT algorithm and the VAST Computational Solid Mechanics (CSM) code [15]. Figure 7 shows results from more recent calculations for a spherical explosion in a deformable cubical box. These calculations were performed using a 2nd order Godunov CFD algorithm and the LSDYNA code [16].

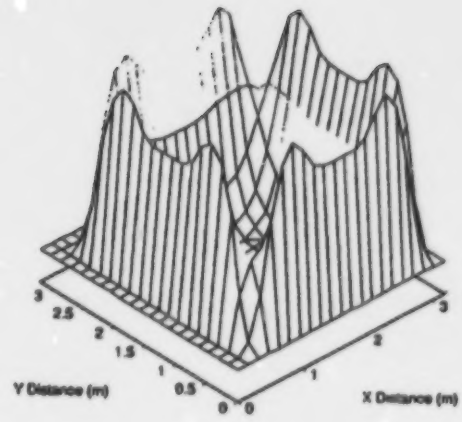

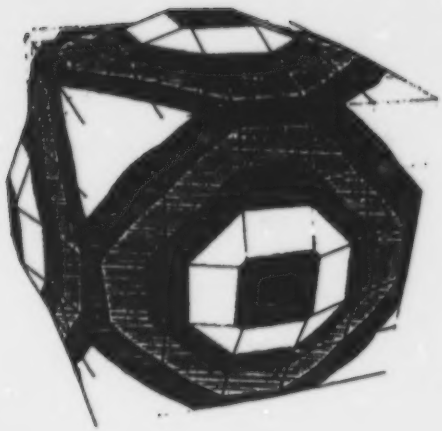

Time = 0.300 ms

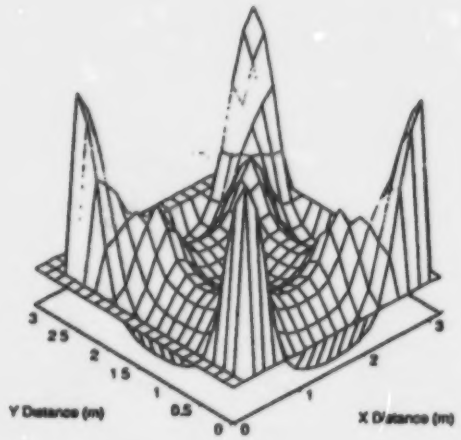

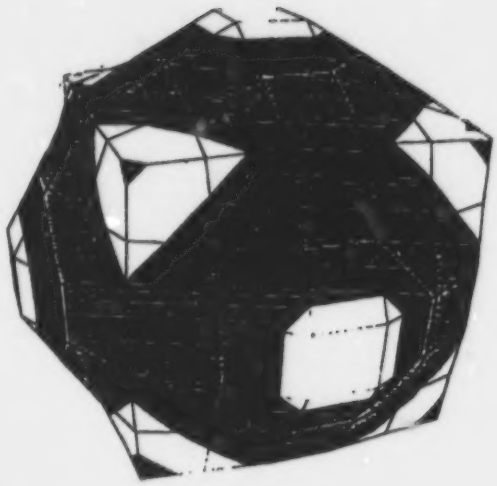

Time = 0.850 ms

Figure 7: Spherical blast wave interacting with deformable box structure (IFSAS/LSDYNA) coupling

5.0 Implementation of Combustion Models in IFSAS

5.1 Models developed under this contract

The following two combustion models were developed under this contract for single phase systems:

1. A Constant Reaction Time model, which is suited to perform calculations of blast waves produced by gaseous detonations.

2. A One-Step Arrhenius model, which can be used to investigate shock ignition and the propagation of unstable gaseous detonations which exhibit oscillatory and cellular detonation structures.

   Figure 8 displays results obtained with the Constant Reaction Time model for a simple detonation driven engine. The FSI calculation included the structural response of the engine's axi-symmetric converging/diverging nozzle.

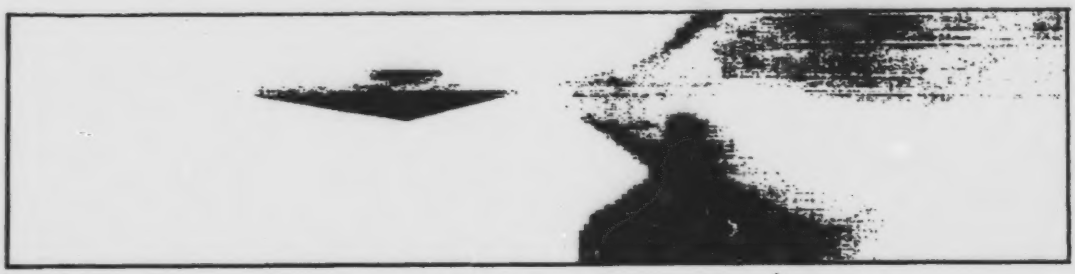

Figure 8: Fluid-structure interaction calculations of a detonation driven engine with nozzle response

5.2 New Developments

Combustion model development after the completion of this contract focused on:

1. Incorporation of single phase models in the 2nd order Adaptive Gridding Scheme (AGS),

2. Implementation of multi-phase models,

3. Support for FSI/combustion calculations.

Figure 9 displays results for a detonation propagating in a non-uniform fuel-air cloud using a 3-D AGS algorithm [17].

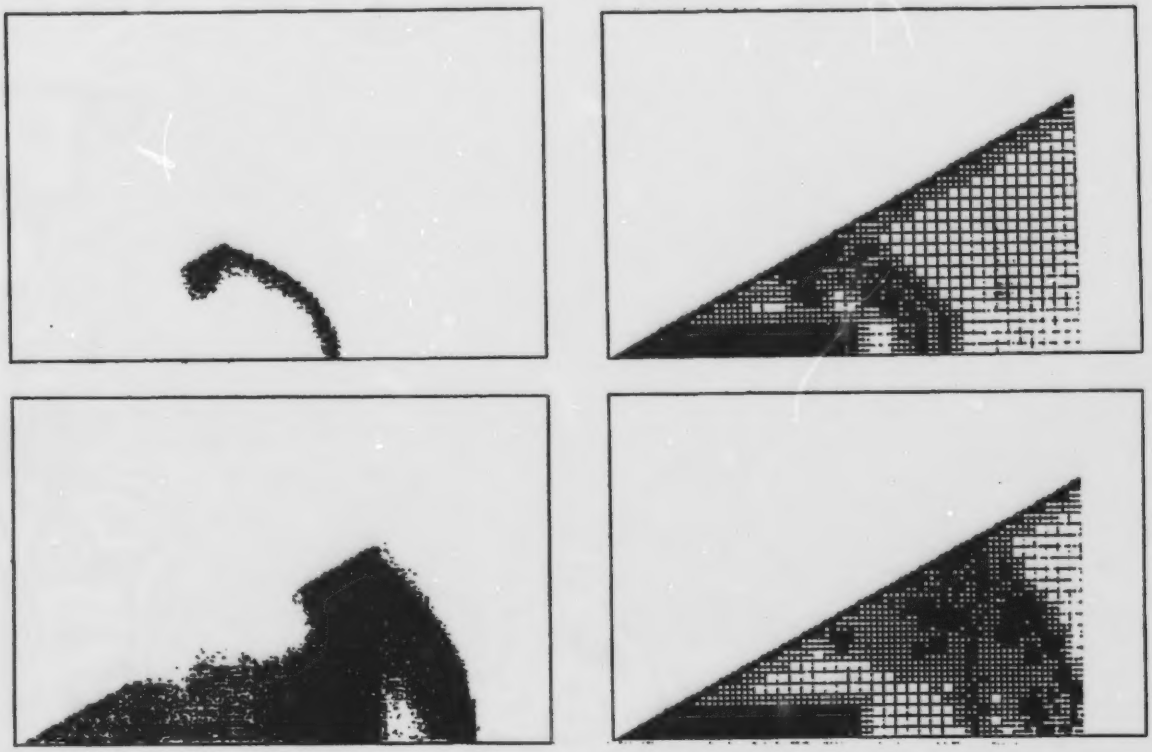

Figure 9: 3-D fuel-air detonation calculation with adaptive gridding

The new multi-phase modelling capabilities in the IFSAS CFD module are designed to consider a wide variety of particle suspensions in fluids which may be classified as follows:

1. Inert fluid with inert particles,
2. Reactive fluid with inert particles,
3. Reactive fluid with reactive particles.

A fluid may be reactive either because it can react by itself or because it can provide an oxidizer to the particles. In the first case, the combustion can be modelled using a One-Step Arrhenius law. In the second case, the oxidizer model uses the oxygen in the fluid to oxidize the particle. Particles are allowed to react with the oxygen, carbon dioxide and water vapour in the fluid. The combustion model accounts for the melting and vaporization of the particles, radiation, and the momentum and heat transfer between the particle and the surrounding fluid. Typical applications of this multi-phase model can be found in the paper by Zhang et al. [18,19] and have also been discussed in the IFSAS course presented at DRES.

6.0 Prototype Code for Gasdynamic and Combustion Calculations

6.1 Prototype Development

This contract initiated the development of a prototype code for gasdynamic and equilibrium calculations. The prototype was developed using the commercial TkSolver platform which allowed rapid implementation and testing of the various algorithms. The prototype considered frozen and equilibrium material descriptions with a variety of processes such as shock waves, isentropic compression, constant volume combustion, constant pressure combustion and detonations.

6.2 New Developments

Due to funding from DERA (UK) and CDL, the prototype code was eventually replaced by a fully graphical and object oriented C++ tool called SuperSTATE, for gasdynamics, chemical equilibrium and chemical kinetics. This code has recently been expanded to include condensed and metallized explosives using an equilibrium solver provided by DSTO (Australia). User [20] and Theory [21] manuals and a training video were provided to DRES during the IFSAS/SuperSTATE course in October 1997.

7.0 Navier Stokes Code

One task of this contract was to investigate the feasibility of implementing a Navier Stokes solver in IFSAS. The main motivation for this capability was to include viscous effects (turbulent and laminar) on the performance of detonation driven projectiles. Due to funding from DERA (UK), a turbulent combustion code was eventually implemented in a prototype version of IFSAS for single and multi-phase systems. This new capability, which will be incorporated in the next release of IFSAS, is based on the following model components:

1. Two-parameter ($k-\varepsilon$) model for compressible flows
2. Eddy break-up combustion model for gas phase
3. Magnussen-Hjertager quenching model for gas phase
4. Smooth and Smith's particle dispersion model

Details of the above model can be found in the theory documents by Hawken [22] and Zhang [23]. An example of the application of this model is shown in Figure 10, which displays the turbulent ingress of combustion products in a compartment from a metallized explosive.

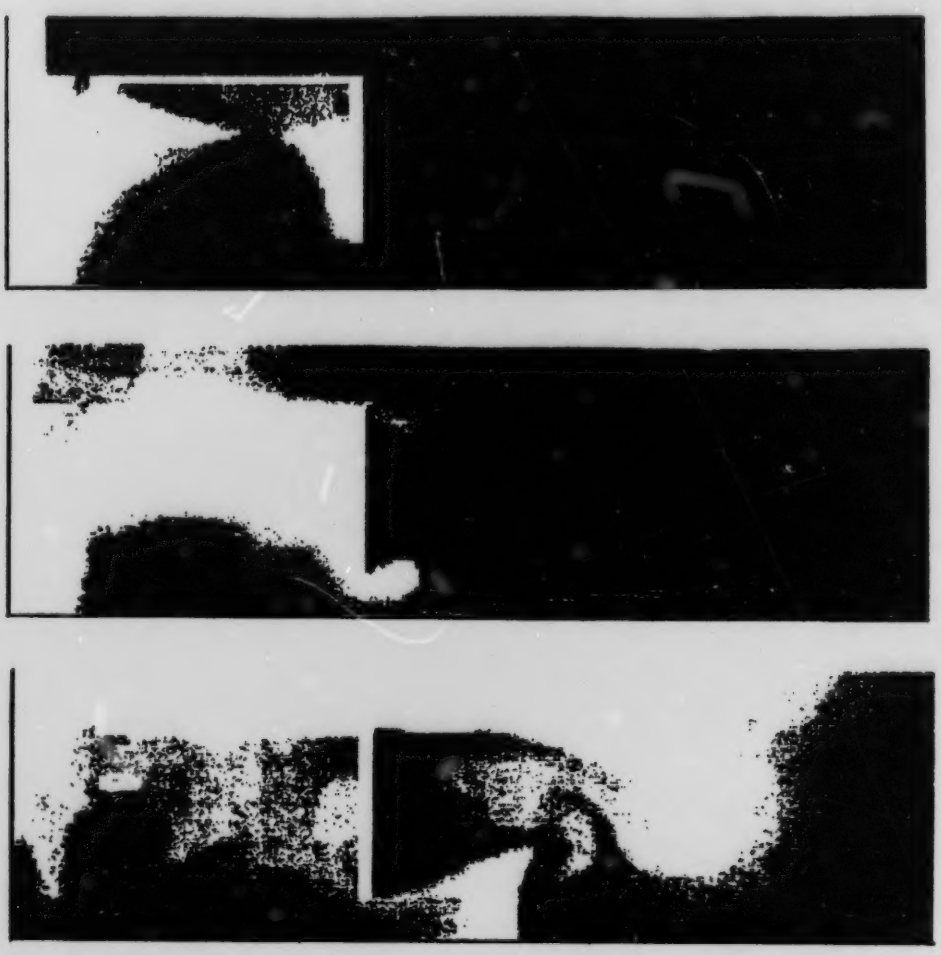

Figure 10: Combustion product ingress into cylindrical chamber

8.0 Future Work

The current IFSAS capabilities developed through funding from DND, UK, Australia and CDL greatly exceed the overall requirements for this contract. One area that would require additional work is the development of a suitable interface between the CFD module and SuperSTATE which would allow CFD calculations using SuperSTATE models. This would greatly increase the combustion modelling capabilities of the CFD module and reduce the cost of directly implementing the same models in both codes. CDL is also considering the possibility of supporting user-defined SuperSTATE models which would allow users to develop, link and test their own models using SuperSTATE and subsequently access them with the CFD module. Another area of improvement is the consolidation of the various solvers, models and features in the CFD module. Numerous solvers have been implemented in IFSAS to address specific user requirements. These include the Lax-Wendroff/FCT scheme in the "hydro" code, the Godunov scheme in the AGS module, the Godunov/MacCormack/FCT scheme for multi-phase

calculations and the modified PISO semi-implicit scheme for low Mach Number flows. Unfortunately, some features, such as fluid structure interaction and non-ideal gas equations of state, have only been implemented for selected solvers. Due to work involved in supporting multiple CFD codes, the algorithms will be consolidated into a single code. For this purpose, the AGS code has been selected as the development platform. The code consolidation work is being funded through a new contract from DRES. CDL is also currently coupling the CFD code with a newly developed 6N DOF rigid body solver. As illustrated in Figure 11, this solver is being used to model the motion of complex structures such as human mannequins.

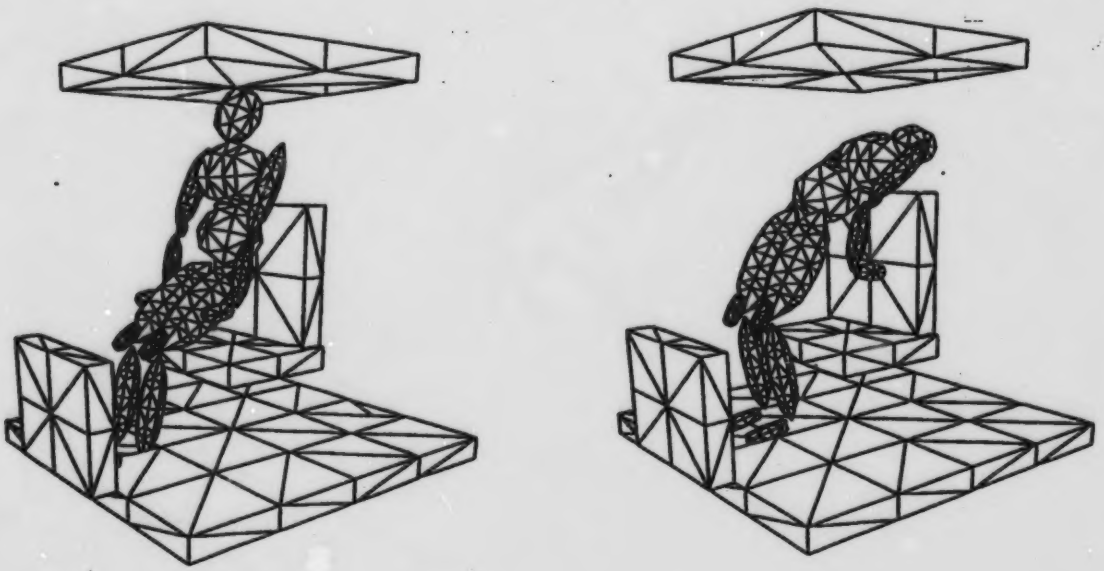

Figure 11. Response of a seated human mannequin to sudden vertical impulse

9.0 References

1. Zhang, F., Thibault, P., Yee. C., Chue, R.S., Frost, D.L. and Lee, J.H.S., "One-Dimensional Stability Analysis of Detonation-Driven Projectiles", AIAA 94-3223, 30th AIAA/ASME/SAE/ASEE Joint Propulsion Conference, June 27-29, Indianapolis, IN, 1994.
2. Thibault, P.A., Penrose, J.D., Sulmistras, A., Murray, S.B. and Labbe, J.L.D.S., "Studies on Detonation Driven Hollow Projectiles", Combustion in High-Speed Flows, J.Buckmaster et al. (eds.), Kluwer Academic Publishers, Netherlands, pp. 421-443, 1994.
3. Thibault, P.A., Zhang, F., Penrose, J. and Sulmistras, A., "Numerical Modelling of Detonation Driven Hollow Projectiles", Proceedings of CFD 94, Second Annual Conference of the CFD Society of Canada, Toronto, Ontario, June 1-3, pp. 395-402, 1994.
4. Zhang, F, Chue, R.S., Frost, D.L., Lee, J.H.S., Thibault, P., Yee, C. "Effects of Area Change and Friction on Detonations Stability in Supersonic Ducts", Proc. R. Soc. London. A, Vol. 449, pp. 31-49, 1995.
5. Murray, S.B, Labbe, J.L.D.S and Thibault, P.A. "Free Flying Tubular Vehicle" US Patent 5,317,866, 1994.
6. IFSAS Reference Manual, Combustion Dynamics Ltd., 1997
7. IFSAS User Manual, Combustion Dynamics Ltd., 1997
8. Tran, D., Link, R., Penrose, J. and Thibault, P.A., "CFD Modelling of Fluid-Structure and Liquid-Gas Interactions", Proceedings of CFD 94, Second Annual Conference of the CFD Society of Canada, Toronto, Ontario, June 1-3, pp. 171-178, 1994.
9. Link , R., Tran, D., Chen, L., Thibault, P.A., Norwood, M. and Slater, J.: "Solution of 2-D and 3-D Fully Coupled FSI Problems for Compressible Flows", Proceedings of CFD 95, Third Annual Conference of the CFD Society of Canada, Banff, Alberta, Vol. II, pp. 71-78, June 25-27, 1995.
10. Zhang, F., Tran, D., Chen, L., Penrose, J. and Thibault, P.A.: "A Cell-Based Adaptively-Refined Cartesian Algorithm for Unsteady Euler Equations", Proceedings of CFD 95, Third Annual Conference of the CFD Society of Canada, Banff, Alberta, Vol. I, pp. 239-246,, June 25-27, 1995.
11. Hawken, D., Zhang, F., Penrose, J. and Thibault, P.A.: "A Level-Set Front-Tracking Algorithm Unstructured Cartesian Grid" Proceedings of CFD98, Sixth International Conference of the Computational Fluid Dynamics Society of Canada, Quebec City, 7-9 June 1998.
12. Smiljanivski, V., Moser, V. and Klein, R.: "A Capturing/Tracking Hybrid Scheme for Deflagration Discontinuities", Comb. Theor. and Mod., Vol. 1 1997.
13. Moser, V., Zhang, F. and Thibault, P., "A Level Set Approach for Detonation Front Tracking", Accepted for CFD 95, Third Annual Conference of the CFD Society of Canada, Banff Alberta, Canada, June 25-27, 1995.
14. Deschambault, R.L. and Glass, I.I.: "An Update on Non-Stationary Oblique-Shock-Wave Reflections: Actual Isopicnics and Numerical Experiments", Journal of Fluid Mechanics, 1983.
15. "Vibration and Strength Analysis Program (VAST): User's Manual Version #7.1", Martec Ltd. October 1995.

16. "LS-DYNA3D User's Manual (Nonlinear Dynamic Analysis of Structures in Three Dimensions", Livermore Software Technology Corporation, January 1, 1996.
17. Blast Waves Produced by Detonations in Three-Dimensional Non-Uniform Fuel-Air Clouds, Combustion Dynamics Ltd. Report, July 1997.
18. Zhang, F., Tran, D., Penrose, J., Yee, C. and Thibault, P.A., "Numerical Studies of Detonation Propagation in Mixtures of Combustible Gases and Inert Dust", Proceedings of CFD 94, Second Annual Conference of the CFD Society of Canada, Toronto, Ontario, June 1-3, pp. 261-268, 1994.
19. Zhang, F., Tran, D., Thibault, P., "Multiphase Models for Detonations and Explosions in a Dusty or Porous Medium", Presented at Combustion Canada '96, Ottawa, Ontario, June 1996.
20. SuperSTATE User Manual
21. SuperSTATE Theory Manual
22. Hawken, D.: "Implementation of Fast Multiphase Reactive Flow Model", Combustion Dynamics Ltd. Report CDL97-SR003, February 1997.
23. Zhang, F.: "Modeling of Fast Multi-Phase Turbulent Reactive Flow,, Part II: Turbulent Particle Dispersion", Combustion Dynamics Ltd. Report CDL97-SR004, February 1997.

Appendix

ONE-DIMENSIONAL STABILITY ANALYSIS OF DETONATION-DRIVEN PROJECTILES

F. Zhang*, P. Thibault†, and C. Yee‡

Combustion Dynamics Ltd., Medicine Hat, Alberta, Canada T1A 8B5

R.S. Chue§, D.L. Frost¶, and J.H.S. Lee#

Mechanical Engineering, McGill University, Montreal, Quebec, Canada H3A 2K6

Abstract

The stability of a detonation-driven projectile passing through a premixed detonable mixture is numerically studied by a transient quasi-one-dimensional model, taking into account the unsteady motion of the projectile and using a single step Arrhenius reaction scheme. The analysis indicates that in the nozzle of the supersonic projectile, raising the rate of area change drives a detonation wave towards instability, while adding roughness behind the shock front increases the detonation velocity and stabilizes the detonation wave. The stable detonation wave configuration can be analyzed by replacing the classical CJ criterion with a generalized sonic choking condition based on the competition between area change, friction and heat release.

Introduction

The use of a stabilized detonation wave (either normal or oblique) for supersonic aircraft propulsion,[1-3] a ram accelerator,[4] or a detonation-driven hollow projectile,[7] relies on the establishment of the detonation wave behind the throat of the nozzle to provide positive thrust. The stability of the detonation wave is essential since it determines whether or not the standing wave configuration can be obtained within an engine from the transient starting conditions. Unfortunately, due to the complex multidimensional wave pattern involved, the stability of a detonation wave in the engine remains poorly understood. The basic instability phenomena associated with detonation-driven engines can be discussed, however, using a one-dimensional theory based on the conservation laws for the average flow quantities across the cross section.

The stability of the standing wave configuration depends on the sensitivity of the reactive mixture, the engine geometry, the boundary layer effects and the operating conditions. Within the frame of the quasi-one-dimensional Euler equations, the controlling mechanisms may be represented by source terms for the chemically exothermic reaction, the area change, and a friction force, while operating conditions are converted into the initial and boundary conditions. The rate of a chemical reaction in a gaseous mixture is an increasing function of temperature, usually $w \sim \exp[-E/(RT)]$, where the parameter E is its activation energy. The larger the activation energy, the stronger the temperature-dependence of the reaction rate. Hence the activation energy is one of the most important parameters controlling detonation stability. Beyond a certain value of the activation energy (i.e., the stability limit), an oscillatory detonation wave solution occurs (e.g., see Fickett and Wood [8]). Other factors which result in a drop of the post-shock temperature have the same effect on the reaction rate as that of an increase of the activation energy, since the reaction rate is exponentially proportional to E/(RT). Therefore, the instability of a

---

* Senior Research Scientist, † President, ‡ Research Scientist

§ Research Associate, ¶ Associate Professor, # Professor

Copyright © 1994 by the American Institute of Aeronautics and Astronautics, Inc. All rights reserved.

detonation wave is not necessarily eliminated by choosing a mixture that is only mildly sensitive to the temperature.

As a detonation wave runs into a converging duct, it may become overdriven in which case its post-shock temperature increases. This tends to stabilize the detonation wave. Conversely, attenuation of the shock may occur as a detonation wave propagates into a diverging duct, and the reduction of the post-shock temperature tends to destabilize the detonation wave. The same effect can occur when a frictional force exists which causes energy dissipation resulting in a drop of the post-shock temperature to induce an oscillatory behaviour of the detonation wave. This behaviour has been demonstrated by Zhang and Lee[9] for the case of a quiescent unburned mixture, where the area change and friction force manifest themselves as "negative" source terms whose competition with the exothermic reaction causes the detonation wave to become unstable. However, it is unclear how area change and friction force compete with the exothermic reaction to influence the stability of a detonation wave in a transient supersonic incoming flow such as occurs in an engine or detonation driven projectile. The present paper addresses this issue, explains the results of the area change effect on detonation stability obtained in the earlier work by Lee et al.[10] and later by authors[11], and discusses the influence of friction force.

In the present paper, a fully transient quasi-one-dimensional model is formulated for a hollow projectile geometry consisting of a short tube with inlet and nozzle sections. This geometry has the essential features of supersonic engines and the ram accelerator (effectively turned inside out), and its operating feasibility has been studied with a 2D axisymmetric inviscid computation by Thibault et al.[7] In the present study, the attention is focused on the stability of the detonation front. The internal flow is basically described by the unsteady quasi-one-dimensional Euler equations with source terms for area change, friction force and exothermic reaction. Its characteristic form is obtained based on a frame of reference attached to the projectile, and is used to derive a criterion for a stabilized wave configuration, in which a function describing the competition between the source terms is of central importance. The influence of area change and friction force on the stability of a detonation wave in the transient, supersonic projectile is analysed by numerical computations.

Theoretical model

To consider the essential features of supersonic engines and the ram accelerator, a hollow projectile geometry is used which consists of an inlet diffuser and a nozzle section, shown in Fig.1. The internal transient flow can be described by quasi-one-dimensional Euler equations which take into account the effects of friction and exothermic reaction. The governing equations derived in a coordinate system moving with the projectile are listed below:

$$\frac{\partial \rho}{\partial t}+\frac{\partial(\rho u)}{\partial x}=-\frac{1}{A}\frac{dA}{dx}\rho u \qquad (1)$$

$$\frac{\partial(\rho u)}{\partial t}+\frac{\partial}{\partial x}(\rho u^2+p)=-\frac{1}{A}\frac{dA}{dx}\rho u^2+f-\rho a_p \qquad (2)$$

$$\frac{\partial(\rho e)}{\partial t}+\frac{\partial}{\partial x}[u(\rho e+p)]=-\frac{1}{A}\frac{dA}{dx}u(\rho e+p)+\dot{q}-\rho u a_p \qquad (3)$$

where the flow velocity with respect to the projectile is denoted by u, pressure by p, density by r, and the acceleration of the projectile by $a_p = dV_p/dt$. The variable e is the sum of the kinetic and internal energy, i.e.,

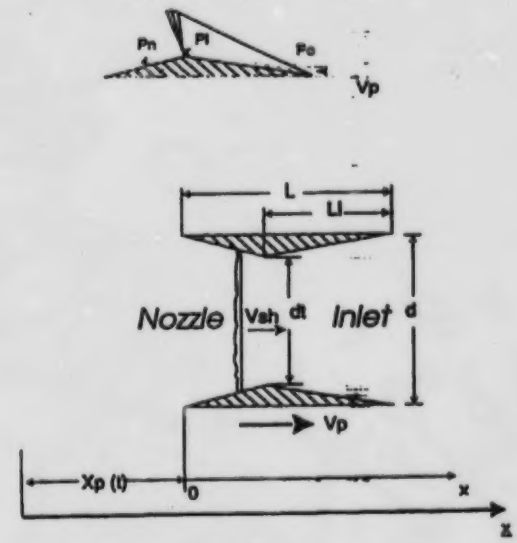

Fig. 1 Hollow projectile and coordinate systems.

$$e = \frac{1}{\gamma - 1}\frac{p}{\rho} + \frac{u^2}{2} \tag{4}$$

To solve the governing equations (1 - 3) the source terms of area change dA/(Adx), friction force f, exothermic reaction $\dot{q}$ and the acceleration of the projectile must be specified. For the present study we are interested only in a qualitative analysis of the competition between these source terms. It is therefore sufficient to choose these source terms as follows. First, the area change is assumed to be described by

$$\frac{1}{A}\frac{dA}{dx} = \frac{\pi}{L - L_1}\ln\frac{d_1}{d}\sin\frac{\pi x}{L - L_1} \qquad for\, 0 \le x \le L - L_1$$
$$\frac{1}{A}\frac{dA}{dx} = \frac{\pi}{L_1}\ln\frac{d_1}{d}\sin\frac{\pi(2L_1 - L + x)}{L_1} \qquad for\, L - L_1 < x \le L \tag{5}$$

and elsewhere dA/dx = 0. The parameters L, L_1, d, d_1 are the length of the projectile, length of the inlet diffuser, outside diameter of the projectile and the throat diameter. The expressions (5) smooth the conical area change and reduce numerical noise.

The friction force has the form of

$$f = -\frac{4c_f}{D_h}\frac{1}{2}\rho u|u| \tag{6}$$

where the minus sign indicates the acting direction of the friction on the gas which is opposite to the flow velocity with respect to the projectile. The parameter D_h usually denotes a hydraulic diameter in a straight duct. In the present study it is regarded as a factor for the magnitude of the friction force. The parameter c_f is the Fanning friction factor. For the unsteady flow behind the shock wave, we follow Zeldovich et al.[12] to assume that it obeys the Blasius law

$$c_f = \frac{0.3164}{Re^{0.25}} \tag{7}$$

where the Reynolds number is defined as

$$Re = \frac{D_h \rho |u|}{\mu} \tag{8}$$

and the dynamic viscosity m follows the Sutherland equation (e.g., see White[13]).

For the exothermic reaction a single step Arrhenius law is assumed, i.e.,

$$\frac{d\beta}{dt} = -\frac{w}{\rho} = -k\beta e^{-\frac{E}{RT}} \tag{9}$$

in which

$$RT = \frac{p}{\rho} \tag{10}$$

Thus, the rate of heat transfer can be written as

$$\dot{q} = Qw \tag{11}$$

Here the variables T and b denote the temperature and the reactant mass fraction with b = 1 in the unburned mixture. Q, w, E, k and R are the effective energy release per unit mass, depletion rate of the reactant mass, activation energy, pre-exponential factor, and gas constant, respectively.

Finally, the projectile acceleration is determined in terms of the thrust divided by the projectile mass according to the Newtonian law, i.e.,

$$a_p = \frac{I}{m} = \frac{1}{m}\left[\int_0^{x_{sh}} p\,dA + \frac{\pi^{1/2} D_h}{2}\int_0^{L} A^{1/2} f\,dx + D_w\right] \tag{12}$$

where the variable x_{sh} denotes the shock front position. The thrust I is the horizontal component of the force acting on the internal projectile surface. Although the presence of the oblique shock attached to the inlet cannot be modelled directly in a one-dimensional formulation, a supersonic wave drag D_w is induced to effectively account for the contribution of the oblique shock to the pressure on the inlet diffuser. For the qualitative analysis, we assume a Cartesian geometry and neglect reflected waves (see Fig. 1), so the drag D_w is determined by the pressure behind the oblique shock wave and the Prandtl-Meyer expansion at the throat, i.e.,

$$D_w = (p_t - p_n)(A_0 - A_t), \qquad for\, x_{sh} < 0$$
$$D_w = p_t(A_0 - A_t) - p_n[A(x_{sh}) - A_t], \qquad for\, 0 \le x_{sh} \le L - L_1 \tag{13}$$

$$D_w = p_1[A_0 - A(x_{sh})], \qquad for\ L - L_1 < x_{sh} < L$$

where the pressure p_1 and p_2 are derived by the relations of oblique shock waves and the Prandtl-Meyer expansion theory respectively (e.g., see Liepmann & Roshko[14]). The influence of the unsteady expansion on D_w is negligible because the pressure behind the expansion at the throat is one to two orders of magnitude less than that behind the oblique shock wave for the incoming flow velocity considered. Note that D_w is used in the expression for a_p only.

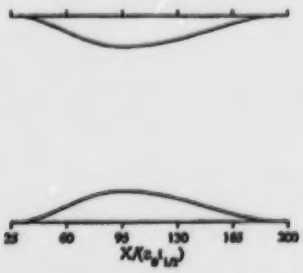

Fig. 2 Shape and length scale of hollow projectile.

The governing equations (1 - 3) are then combined with (5 - 13) to be expressed in the conservation form and numerically solved using a higher order of extension of Godunov's method with Strang's splitting algorithm. In this study, the diameter ratio of the throat to the projectile d_t/d and the initial projectile Mach number (i.e., $M_{p0} = V_{p0}/c_0$) are variables, whereas the other projectile parameters are fixed as follows: $L_t/L = 0.6$, $d/L = 0.84$, $L = 120$ mm, $m = 51$ g, $p_0 = 11$ bar. The nondimensionalized mixture parameters are $g = 1.2$, $Q = 50$ (giving a CJ detonation velocity of $D_{cj} = 6.2\ c_0$), and the activation energy $E = 22$. This value of the activation energy is far below the detonation stability limit for a planar CJ detonation in a straight duct without friction ($E_a = 25$). The detonation is initiated at the exit of the nozzle by imposing a local region of high pressure and temperature. The shape and length scale of the projectile used in the computations are shown in Fig. 2.

Criterion for a stationary wave configuration

From the classical mechanical point of view, a detonation wave can be stationary in a supersonic projectile only if the projectile and the detonation velocities are equal and the acceleration of the projectile vanishes, i.e.,

$$V_p = V_{sh}; \qquad a_p = 0 \tag{14}$$

Any acceleration of the projectile will result in a movement of the detonation front with respect to the projectile, and vice versa. The question arises as to how the internal flow adjusts itself to satisfy the kinematic and dynamic balance conditions (14). To answer this question it is sufficient to look at the state downstream of the shock front along the characteristic C^+, because any disturbance from downstream acting on the shock front is transmitted along a right running acoustic wave. Upon manipulating (1 - 3) the characteristic equation along C^+ can be obtained, i.e.,

$$C^+: \qquad \frac{dx}{dt} = u + c \tag{15}$$

$$\left(\frac{dp}{dt}\right)^+ + \rho c\left(\frac{du}{dt}\right)^+ = \psi - \rho c a_p \tag{16}$$

where

$$\psi = (\gamma - 1)\dot{q} - \frac{1}{A}\frac{dA}{dx}\rho c^2 u + fc\left[1 - (\gamma - 1)\frac{u}{c}\right] \tag{17}$$

$$\left(\frac{d}{dt}\right)^+ = \frac{\partial}{\partial t} + (u + c)\frac{\partial}{\partial x}$$

The function Ψ represents rates of energy production caused by the source terms for exothermic reaction, area change, and friction, and has been called a "competition" function by Zhang and Lee[9] since its value describes the competing effect of the energy production under the source terms involved. A positive value of the function Ψ indicates that a compression wave propagates along the characteristic C^+ to amplify the shock, while a negative value denotes a rarefaction wave which attenuates the shock. If the competition between the source terms which interact with the shock front results in the flow having a right running characteristic, defined by $dx/dt = 0$ along which a steady state exists, such a characteristic must then correspond to the sonic locus x, (see (15)) on which the right hand side of (16) vanishes. A sufficient condition for disappearance of the right hand side of (16)

is $\Psi = 0$ and $a_p = 0$. So one can use a control volume analysis between the two steady states, i.e., at the sonic locus and at the projectile front, to obtain a steady wave solution. Thus, a condition for a steady solution (i.e., $a_p = 0$) is

$$V_p - v(x_s) = -u(x_s) = c(x_s) \tag{18}$$

$$\psi(x_s) = 0 \tag{19}$$

where the variable v refers to the flow velocity in the laboratory coordinates. Upon replacing (14) into (18) one obtains

$$V_{sh} - v(x_s) = c(x_s) \tag{20}$$

The criterion (19 - 20) is a saddle point condition, and provides a sonic choking plane with respect to the shock front at which the rates of energy production caused by the source terms for exothermic reaction, area change, and friction attain a balance. Whether the stabilized detonation wave is overdriven or has a velocity deficit with respect to the CJ detonation value depends on the sign and the magnitude of area change and friction force at the stabilized position. For a steady wave solution with a velocity deficit, equation (19) indicates that a portion of chemical energy is left at the sonic locus and released in the supersonic flow downstream. On the other hand, if an overdriven detonation wave solution exists, the chemical energy release is completed upstream, in the subsonic flow regime. As the product flow arrives at the sonic locus, the balance of the energy change rates caused by area change and friction enables the sonic matching and a steady wave solution is then realized. Note that the criterion (19 - 20) also implies steady flow ahead of the shock front since the acceleration of the projectile vanishes and its velocity then remains constant.

Effect of area change on detonation stability

In order to understand clearly the competing effects of the individual source terms with the exothermic reaction on the stability of a detonation wave, we first focus on the source term for area change and assume the friction force $f = 0$.

From the point of view of the one-dimensional theory, any wave configuration that does not satisfy the sonic matching criterion (19 - 20) is a transient state. For the supersonic projectile studied, the criterion cannot be satisfied for a detonation wave located in the inlet section because the classical supersonic diffuser instability will occur. For a detonation wave propagating in the nozzle where the area change is converging towards the throat, a positive thrust behind the shock front is created (see (12)) which enables a dynamic balance to be achieved with the wave drag D_w based on the oblique shock waves attached at the inlet. If the kinematic matching (i.e., $V_p = V_{sh}$) is attained at the moment of the dynamic balance, the criterion (19 - 20) is then satisfied and a stationary wave configuration can exist. However, the achievement of these conditions is subject to the interaction of the area change with the shock front and the reacting flow, depending on the flow ahead of the shock front.

Following Chester[13] to apply the method by Whitham[16] for a non-reactive shock wave moving through non-uniform steady flow in a duct of varying cross section, one can obtain the interaction rules of area change with the shock front (see Appendix). For subsonic flow in a duct, the rule is the same as in the case of a quiescent gas ahead of the front, that is, the shock wave is attenuated in a diverging duct and amplified in a converging duct. For a supersonic flow ahead of the front, the rule provides an opposite interaction effect, and states that the shock wave is amplified in a diverging duct, while attenuated in a converging duct. This principle is also valid for a detonation wave propagating in the nozzle of the supersonic projectile studied. However, the influence of area change on detonation wave manifests itself through two aspects: the attenuation of the shock velocity due to the interaction of the converging area change with the shock front; and the attenuation of the shock velocity by the rarefaction waves behind the shock front. The rarefaction waves are created by the interaction of the converging area change and the reacting flow towards the nozzle exit, which results in negative values of the second term of the function Ψ in (17). Consequently the post-shock temperature drops and the detonation velocity has a deficit with respect to the

Chapman-Jouguet value. In this case, the negative value of the area change term in the function Ψ represents a rate of energy withdrawal which competes with the chemical heat release, so that the sonic matching criterion (19 -20) might be satisfied. However, in one-dimensional detonation theory it is first established by Fickett and Wood[8] that an oscillatory wave solution occurs as the activation energy of a gaseous mixture is increased beyond a stability limit. Decreasing the post-shock temperature has the same effect on the rate of the chemical reaction as increasing the activation energy, because the reaction rate in a gaseous mixture is proportional to exp[-E/(RT)] where the activation energy is denoted by E and the post-shock temperature by T. Thus increasing the rate of area change in the nozzle of a supersonic engine or projectile in general leads the criterion (19 - 20) to fail, and drives the detonation towards instability.

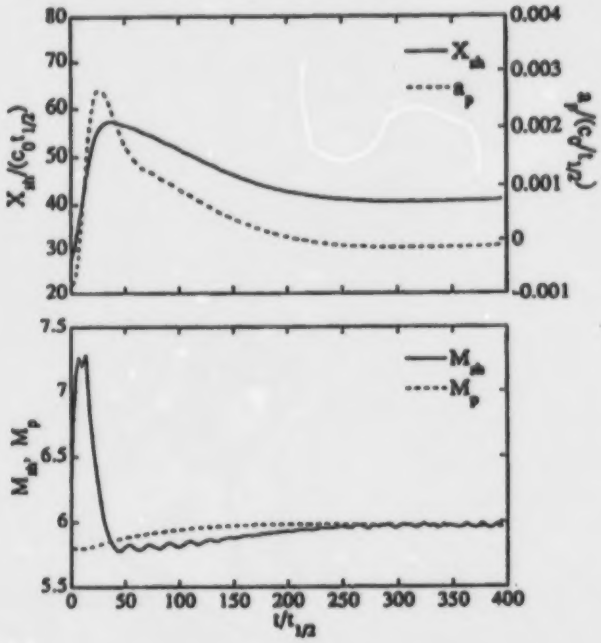

Fig. 3 Time evolution of shock front trajectory X_{sh}, acceleration of projectile a_p, Detonation Mach number M_{sh}, and Mach number of projectile M_p. Projectile parameters are: d/L = 0.84, L/L = 0.6, d/d = 0.7, M_{p0} = 5.8. Detonation parameters are: g = 1.2, Q = 50, E = 22. $t_{1/2}$ is the standard half reaction time. friction force: f = 0.

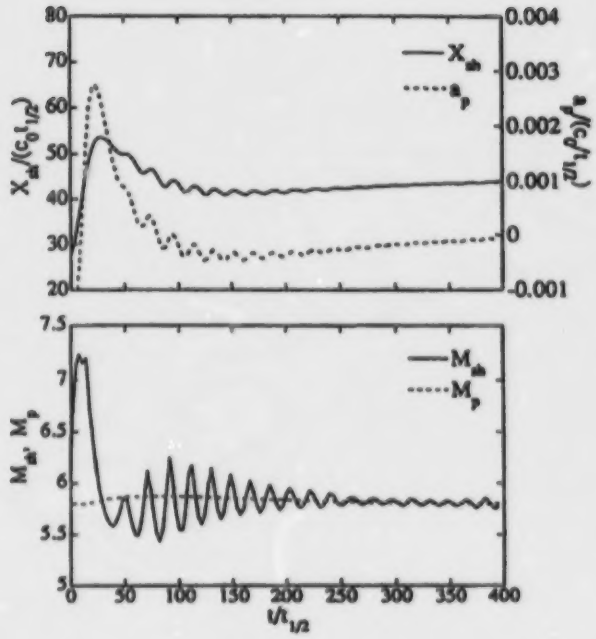

Fig. 4 Time evolution of shock front trajectory X_{sh}, acceleration of projectile a_p, Detonation Mach number M_{sh}, and Mach number of projectile M_p. Parameters are the same as those in Fig. 3 except for d/d = 0.6.

If the area change of the supersonic nozzle is so small that the reduction of the post-shock temperature is not sufficient to excite any instability mode. the detonation can then be stabilized within the nozzle (see Fig. 3). In this example the diameter ratio of throat to projectile is d/d = 0.7 and the initial projectile Mach number M_{p0} = 5.8. After an initial overshoot, the detonation Mach number (i.e., $M_{sh} = V_{sh}/c_0$) decays. The high pressure behind the shock front overcomes the wave drag and creates a positive thrust which accelerates the projectile. As the projectile Mach number (i.e., $M_p = V_p/c_0$) approaches M_{sh}, the detonation penetrates furthest into the nozzle, and a_p nears its maximum. Due to the projectile acceleration, M_p increases above M_{sh} and the detonation front then moves downstream. This in turn causes a_p to decrease. Meanwhile, M_{sh} is increased as the detonation front moves leeward because of the reduction of the rate of area change dA/(Adx) and the pressure

ahead of the front, which raises the pressure ratio across the shock front. Finally the detonation wave is stabilized at the position where $M_p = M_{sh}$ and $a_p = 0$ are satisfied. The velocity of the stabilized detonation has a deficit of $DV_{sh} = -0.2\ c_0$ with respect to the CJ detonation velocity (i.e., $D_{CJ} = 6.2$).

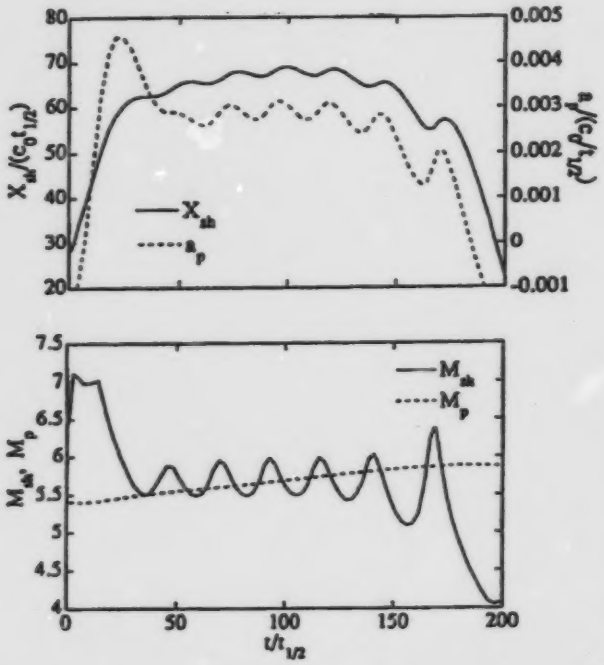

Fig. 5 Time evolution of shock front trajectory X_{sh}, acceleration of projectile a_p, Detonation Mach number M_{sh}, and Mach number of projectile M_p. Parameters are the same as those in Fig. 3 except for $d_i/d = 0.6$, $M_{pi} = 5.4$.

In the case of a very large area change, the detonation decays after initiation and eventually fails. However, for a range of intermediate values of the area change, the detonation executes an oscillatory behaviour as it propagates (see. Fig. 4 with $d_i/d = 0.6$). Whether it can be restabilized or not, depends greatly on the rate of area change dA/(Adx) during the transient motion of the detonation wave. In Fig. 4 we choose the same initial projectile Mach number (i.e., $M_p = 5.8$) as that used in Fig. 3. The detonation wave penetrates to the furthest position ($x = 52$) where $M_p = M_{sh}$, attained while $a_p > 0$. The oscillation of the wave front is damped as it returns downstream, due to the reduction of the rate of area change and the increase of the pressure ratio across the front. Thus, the detonation wave can be restabilized in an oscillatory fashion, and a standing wave configuration can exist in a cycle-averaged sense with a mean velocity deficit of $DV_{sh} = -0.4c_0$. However, upon reducing the initial Mach number to $M_p = 5.4$, the penetration depth of the detonation wave is increased beyond $x > 62$ where the amplitude of the area change dA/(Adx) is sufficiently large to induce rapid growth of the oscillation (see Fig. 5). As a consequence, the detonation velocity cannot recover and the wave is swallowed out of the exit of the nozzle.

The computations discussed above are based on a very low activation energy (i.e., $E = 22$) for which the detonation wave would be highly stable if propagated in a straight duct. If the mixture has an activation energy beyond the detonation stability limit (i.e., $E_a = 25$ with the other mixture parameters fixed), an oscillatory solution could occur even for a small area change. The oscillatory phenomena of the detonation wave studied here is essentially the same as in the case of firing a sphere into a detonable gas observed by Behrens[17], where the expansion of the reacting flow is induced by the area change between the sphere and the bow shock at the sphere front.

Effect of friction on detonation stability and final projectile velocity

Let us consider a detonation wave propagating in a straight duct with friction (i.e., $dA/dx = 0$). From the mechanical point of view, friction force on the gas acts in the opposite direction of the flow velocity. In the case of quiescent flow ahead of a detonation wave, the friction force is then opposite to the propagation direction of the detonation wave and provides a negative source term in the function Ψ (17), where $V_p = 0$. Its interaction with the exothermic reaction (i.e., the positive source term) results in a velocity deficit of the detonation and causes a drop of the post-shock temperature. Thus, the effect of friction is to drive a detonation towards instability, and an oscillatory wave solution can occur for large friction factors[9]. However, as a detonation wave propagates into

an opposed supersonic flow, there exists a friction force both ahead of the shock front in the positive direction (i.e., the propagation direction of the detonation wave) and behind the shock front. The effect of friction on the detonation greatly depends on the magnitude of the incoming flow velocity with respect to the wall. If the incoming flow velocity is small enough that the flow behind the shock front remains in the positive direction and the rarefaction induced by the reaction does not change the flow direction, the influence of the friction force behind the shock front which acts in the negative direction will exceed the influence of the friction force ahead of the shock front. In this case the effect of friction is to create a detonation velocity deficit and hence a drop in the post-shock temperature. However, when the incoming flow velocity is made sufficiently large, the flow behind the shock front will be in the negative direction, which results in the friction force behind the shock front being in the positive direction and creates a positive source term in the function Ψ. The effect of friction is then completely changed; it increases the velocity of the detonation wave and drives the detonation wave towards stability.

For a detonation wave propagating in the nozzle of the supersonic projectile studied, the projectile velocity is close to that of the detonation, hence the post-shock velocity of the flow with respect to the body wall is in the negative direction. Consequently, the friction acting on the internal flow is in the positive direction to amplify the detonation velocity and serves to stabilize the detonation. On the other hand, the friction force acts also on the internal surface of the nozzle in the negative direction, and creates a deceleration of the projectile (see (12)). This deceleration competes with the area change term in which the pressure is enhanced by the friction acting on the reacting flow. If one properly chooses the engine geometry and operating conditions so that a stabilized wave can be attained, the projectile velocity can then be increased by adding friction since at the stabilized position the projectile velocity must equal the detonation velocity.

The numerical calculation indicates that the effect of skin friction (i.e., with a small friction factor) is not significant and provides only a slight increase of the detonation velocity compared with the results without friction. Increasing the roughness behind the shock front can overcome the velocity deficit caused by the area change and drive the detonation into the overdriven regime (see Figs. 6). In this example, the same parameters as in Fig. 3 are used, but friction is added with the ratio of friction factors behind and ahead of the shock front $c_{f2}/c_{f1} = 40$. At the end of the transient development, the stabilized projectile Mach number M_p, which equals the stabilized detonation Mach number M_{sh}, is increased from $M_p = 6.0$ (without friction) to $M_p = 6.4$ (with friction). This represents a 7% overdrive of the CJ detonation.

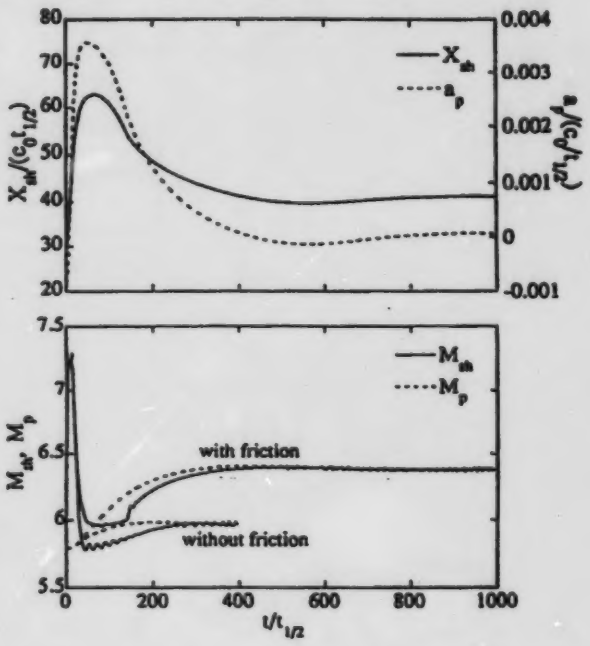

Fig. 6 Time evolution of shock front trajectory X_{sh}, acceleration of projectile a_p, Detonation Mach number M_{sh}, and Mach number of projectile M_p. Parameters are the same as those in Fig. 3 but with friction factor ratio of $c_{f2}/c_{f1} = 40$.

Note that there exists an upper limit of the friction factor beyond which a stabilized wave configuration

cannot be attained with the given engine geometry and operating conditions. The shock front trajectory, shown in Fig. 7, indicates that by increasing the friction factor ratio to $c_{f2}/c_{f1} = 50$, the detonation front penetrates so far into the throat that the projectile accelerates to well above the velocity of the detonation front as it moves leeward. Eventually, the detonation front is swallowed out of the nozzle (i.e., $x_{sh} = 27.4\ c_0 t_{1/2}$). Further increasing the friction factor ratio to $c_{f2}/c_{f1} = 100$, the detonation front passes through the throat and is expelled out of the inlet. In both cases, the stabilized detonation wave can be established only if the area change or the initial projectile velocity is adjusted to make the transient process terminate at the position where the criterion (19 - 20) is satisfied.

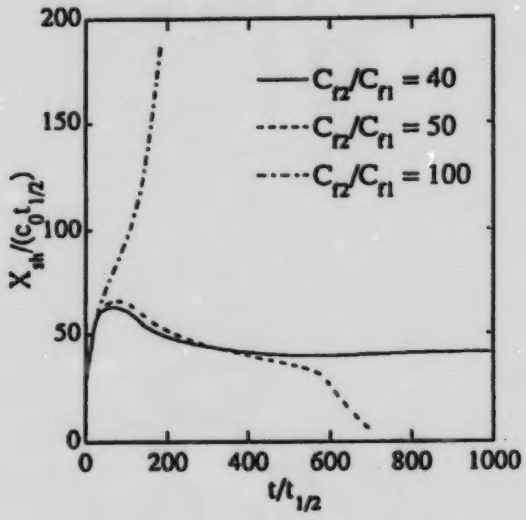

Fig. 7 Time evolution of shock front trajectory X_{sh} with different friction factor ratios. Parameters are the same as those in Fig. 3.

Conclusions

This paper has presented a quasi-1D stability analysis of a detonation driven projectile taking into account the unsteady motion of the projectile and using a single step Arrhenius reaction scheme. The analysis demonstrates that the detonation wave stability is decreased by the rate of area change in the supersonic moving nozzle and is increased by adding friction behind the shock front. A novel concept is to add roughness in the nozzle behind the shock front to improve the stability of the detonation front and increase the final projectile velocity. The stable detonation configuration can be analyzed by replacing the classical CJ criterion with a generalized sonic choking condition that takes into account the competition between area change, friction, and heat release. Once again, the results of this work strongly suggest that the possible onset of propulsion instability should be addressed in the design of detonation driven engines and ram accelerators.

Appendix. Shock wave through flow in ducts of varying cross section

Following Chester[15] and Han and Yin[18] to apply the method by Whitham[16] for a non-reactive shock wave moving through non-uniform steady flow in a duct of varying cross section, we obtain the relations describing the change of the shock Mach number M_s, the area change, and the flow Mach number ahead of the shock (i.e., M_1)

$$dM_s = G dM_1 \qquad (21)$$

$$\frac{dA}{A} = \frac{M_1^2 - 1}{1 + \frac{\gamma - 1}{2} M_1^2} \frac{dM_1}{M_1}$$

where

$$G = \frac{\frac{M_1}{E} + \frac{\gamma - 1}{2}\frac{M_1 M_2}{E} - \frac{M_2}{F} - \frac{M_1^2 - 1}{EM_1}\frac{M_2}{M_2 + 1}}{\frac{2M_2}{(\gamma+1)F}\left(1 + \frac{1}{M_s^2}\right) + \frac{4M_s}{2\gamma M_s^2 - (\gamma - 1)}} \qquad (22)$$

$$M_2 = \frac{(\gamma+1)M_1 M_s + 2(M_s^2 - 1)}{[2\gamma M_s^2 - (\gamma - 1)]^{1/2}[(\gamma - 1)M_s^2 + 2]^{1/2}} \qquad (23)$$

$$E = 1 + \frac{\gamma - 1}{2} M_1^2, \quad F = M_1 + \frac{2(M_s^2 - 1)}{(\gamma + 1)M_s^2}$$

The behaviour of the G-function and the flow Mach number immediately behind the shock front (i.e., M_2)

varying with M_1 and M_s are displayed in Figs. 8 and 9 where Figure 8 is for the case of M_1 being in the positive x-direction (i.e., the same as that of M_s), while Figure 9 represents the case of M_1 in the negative x-direction (i.e., opposite to that of M_s). In the case where $M_1 > 0$, both $M_2 > 0$ and $G > 0$, while for $M_1 < 0$, the sign of M_2 is changed from positive to negative at the point where $|M_1| = 2(M_s^2-1)/((g+1)M_s) < M_s$. As seen in Fig. 9, $G < 0$ up to the point where $M_2 \to -1$, after which the flow chokes immediately behind the shock front due to the influence of the area change, which stands on the last term in the numerator of the G-function. After the discontinuity in G at $M_2 = -1$, G becomes positive. Note that the shock Mach number M_s is relative to the flow ahead of the front. At the point where $|M_1| = M_s$ the shock front is therefore stationary with respect to the duct wall. Thereafter, the shock front moves in the negative x-direction relative to the wall of the duct.

$$dA > 0 \quad dM_1 < 0 \quad dM_s < 0 \quad \text{for } M_1 < 1 \quad (24)$$
$$dA < 0 \quad dM_1 > 0 \quad dM_s > 0$$

$$dA > 0 \quad dM_1 > 0 \quad dM_s > 0 \quad \text{for } M_1 > 1 \quad (25)$$
$$dA < 0 \quad dM_1 < 0 \quad dM_s < 0$$

while in the case where M_1 is in the negative x-direction and within the range of $G < 0$:

$$dA > 0 \quad dM_1 > 0 \quad dM_s < 0 \quad \text{for } |M_1| < 1 \quad (26)$$
$$dA < 0 \quad dM_1 < 0 \quad dM_s > 0$$

$$dA > 0 \quad dM_1 < 0 \quad dM_s > 0 \quad \text{for } |M_1| > 1 \quad (27)$$
$$dA < 0 \quad dM_1 > 0 \quad dM_s < 0$$

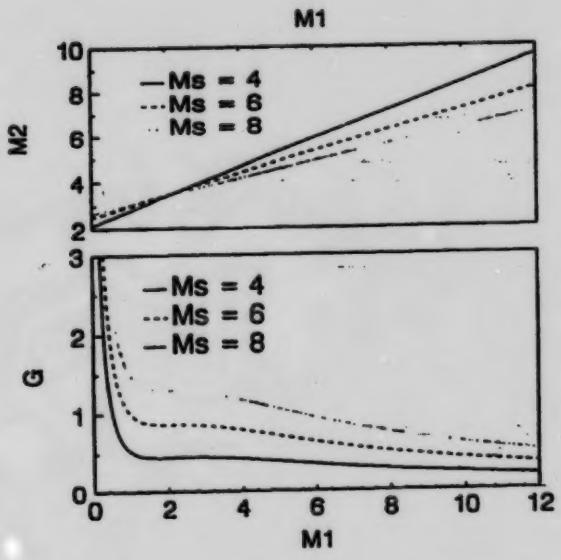

Fig. 8 Variation of G-function and flow Mach number immediately behind shock front M_2 with flow Mach number ahead of shock front $M_1 > 0$.

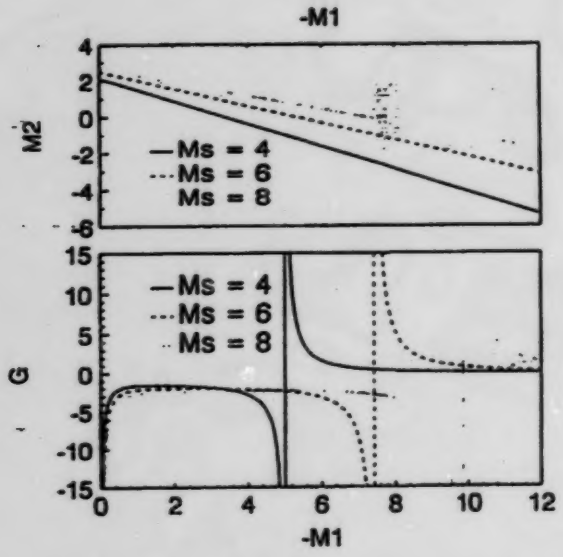

Fig. 9 Variation of G-function and flow Mach number immediately behind shock front M_2 with flow Mach number ahead of shock front $M_1 < 0$.

Once the behaviour of the G-function is known, the rules for the interaction of the area change with the shock front can be obtained from (21). They are listed below: For the case where M_1 is in the positive x-direction:

The rules (24 - 27) clearly indicate that the effects of area change on a shock front in a subsonic flow is the opposite of these effects which occur when the flow ahead

of the front is supersonic. For the subsonic flow in a duct, the rule is the same as in the case of a quiescent gas ahead of the front, that is, the shock wave is attenuated in a diverging duct and amplified in a converging duct. However, for a supersonic flow ahead of the front, the shock wave is amplified in a diverging duct, and attenuated in a converging duct.

References

1. Dunlap, R., Brehm, R.L. and Nicholls, J.A. 1958 A preliminary study of the application of steady state detonative combustion to a reaction engine. Jet Propulsion 28. 451-456.
2. Sargent, W.H. and Gross, R.A. (1960) Detonation wave hypersonic ramjet. ARS J. 30. 543-549
3. Morrison, R.B. 1978 Evaluation of the oblique detonation wave ramjet. Universal Systems Inc., NASA CR-145358.
4. Ostrander, M.J., Hyde, J.C., Young, M.F., Kissinger, R.D. and Pratt, D.T. 1987 Standing oblique detonation wave engine performance. AIAA Paper 87-2002.
5. Atamanchuk, T. and Sislian, J. 1991 Hypersonic detonation wave powered lifting-propulsive bodies. AIAA 3rd Int. Aero. Planes Conference, Orlando, Florida.
6. Herzberg, A. Bruckner, A. P. and Bogdanoff, D. W. 1988 Ram accelerator: A new chemical method for accelerating projectiles to ultrahigh velocities. AIAA J. 26. 195-203.
7. Thibault PA, Penrose JD, Sulmistras A, Murray SB, Labbe JLDS 1992 Studies on detonation driven hollow projectiles. 2nd ICASE/NASA LaRC Meeting on Combustion, Newport News, VA, Oct. 12-14.
8. Fickett W. and Wood W. W. 1966 Flow calculations for pulsating one-dimensional detonations. Phy. Fluids, 9. 903-916.
9. Zhang F., Lee J.H.S. 1993 Friction-induced oscillatory behavior of one-dimensional detonations. Proc. R. Soc. Lond. A. (in press)
10. Lee J.H., Zhang F. and Chue R.S. 1992 Some fundamental problems of detonation instabilities and its relation to engine operation. 2nd ICASE/NASA LaRC Meeting on Combustion, Newport News, VA. Oct. 12-14.
11. Zhang, F., Frost, D.L., Chue, R.S., Lee, J.H.S., Thibault, P. and Yee, C. 1993 Stability studies of detonation driven projectiles. 19th Int. Symp. Shock Waves. Marseille, France.
12. Zeldovich, Ya.B., Borisov, A.A., Gelfand, B.E., Frolov, S.M., and Mailkov, A.E. 1988 Nonideal detonation waves in rough tubes. Dynamics of Explosion (ed. A.L. Kuhl, J-C Leyer and A.A) Borisov). Prog. Astronaut. Aeronaut. 144. 211-231.
13. White, F.M. 1974 Viscous Fluid Flow. 28-36. New York: McGraw-Hill.
14. Liepmann, H.W. and Roshko, A. 1957 Elements of gasdynamics. 84-120. John Wiley & Sons Inc.
15. Chester W. 1960 The propagation of shock waves along ducts. Adv. in Appl. Math. 6. 119-152.
16. Whitham, G.B. 1958 On the propagation of shock waves through regions of nonuniform area or flow. J. Fluid Mech. 4. 337.
17. Behrens M., Struth W. and Wecken F. 1965 Studies of hypervelocity firings into mixtures of hydrogen with air or with oxygen In Proc. 10th Symp. (Int.) Combust. 245-252. Pittsburgh: The Combustion Institute.
18. Han, Z and Yin, X 1993 Shock Dynamics. Netherlands: Kluwer Academic Publishers.

Effects of area change and friction on detonation stability in supersonic ducts

By F. Zhang[1], R. S. Chue[2], D. L. Frost[2], J. H. S. Lee[2], P. Thibault[1] and C. Yee[1]

[1] *Combustion Dynamics Ltd, Suite 203, 132 4th Avenue S.E., Medicine Hat, Alberta, Canada T1A 8B5*

[2] *McGill University, 817 Sherbrooke Street W., Montreal, Quebec, Canada H3A 2K6*

The stability of a detonation wave passing through opposed supersonic flow in a duct of varying cross section and with friction is studied numerically by a transient quasi-one-dimensional model, taking into account the unsteady motion of the duct and using a single-step Arrhenius reaction scheme. The analysis indicates that in a converging duct, that is, a nozzle raising the rate of area change drives a detonation wave towards instability, and adding roughness behind the shock front increases the detonation velocity and stabilizes the detonation wave. The stable detonation-wave configuration can be analysed by replacing the classical Chapman–Jouguet criterion with a generalized sonic choking condition based on the competition between area change, friction and heat release.

1. Introduction

The use of a stabilized detonation wave (either normal or oblique) for supersonic aircraft propulsion (see, for example, Dunlap *et al.* (1958), Sargent & Gross (1960), Morrison (1978), Ostrander *et al.* (1987) and Atamanchuk & Sislian (1991), ram accelerator (Hertzberg *et al.* 1988) or a detonation-driven hollow projectile (Thibault *et al.* 1992; Zhang *et al.* 1993) relies on the establishment of the detonation wave behind the throat of the nozzle to provide positive thrust. The stability of the detonation wave is essential because it determines whether a standing-wave configuration can be obtained within an engine from the transient starting conditions. Unfortunately, owing to the complex multidimensional wave pattern involved, the stability of a detonation wave in the engine remains poorly understood. The basic instability phenomena associated with detonation-driven engines can be discussed, however, with the use of a one-dimensional theory based on the conservation laws for the average flow quantities across the cross section.

The stability of the standing-wave configuration depends on the sensitivity of the reactive mixture, the engine geometry, the boundary-layer effects and the operating conditions. Within the frame of the quasi-one-dimensional Euler equations, the controlling mechanisms may be represented by source terms for the chemically exothermic reaction, the area change and a friction force, while operating conditions are converted into initial and boundary conditions. The rate of chemical reaction in a gaseous mixture is an increasing function of temperature, usually $w \sim e^{-E/RT}$, where the parameter E is its activation energy. The larger the activation energy, the stronger the temperature dependence of the reaction rate. Hence the activation

Proc. R. Soc. Lond. A (1995) 449, 31–49
Printed in Great Britain

© 1995 The Royal Society

energy is one of the most important parameters controlling detonation stability. Beyond a certain value of the activation energy (i.e. the stability limit), an oscillatory detonation-wave solution occurs (Fickett & Wood 1966). Source terms that result in a drop of the post-shock temperature have the same effect on the reaction rate as that of an increase of the activation energy, since the reaction rate is exponentially proportional to $E/(RT)$. Therefore the instability of a detonation wave is not necessarily eliminated by choosing a mixture that is only mildly sensitive to the temperature.

As a detonation wave runs into a converging duct, it may become overdriven, in which case its post-shock temperature increases. This tends to stabilize the detonation wave. Conversely, attenuation of the shock may occur as a detonation wave propagates into a diverging duct, and the reduction of the post-shock temperature tends to destabilize the detonation wave. The same effect can occur when a frictional force exists that causes energy dissipation, resulting in a drop of the post-shock temperature to induce an oscillatory behaviour of the detonation wave. This behaviour has been demonstrated for a quiescent unburned mixture, where the area change and friction force manifest themselves as 'negative' source terms whose competition with the exothermic reaction causes the detonation wave to become unstable (Zhang & Lee 1994). However, it is unclear how area change and friction force compete with the exothermic reaction to influence the stability of a detonation wave in a transient supersonic incoming flow such as occurs in a detonation-driven engine or projectile. The present paper addresses this issue, explains the results of the area-change effect on detonation stability obtained in the earlier work by Lee *et al.* (1992) and Zhang *et al.* (1993), and discusses the influence of friction force.

A fully transient quasi-one-dimensional model is formulated for a supersonic moving duct with inlet and nozzle sections. This geometry has the essential features of supersonic engines and the ram accelerator (effectively turned inside out), and its operating feasibility has been studied by an earlier 2D axisymmetric inviscid computation (Thibault *et al.* 1992). In the present study, the attention is focused on the stability of the detonation front. The internal flow is described by the unsteady quasi-one-dimensional Euler equations with source terms for area change, friction force and exothermic reaction. Its characteristic form is obtained based on a frame of reference attached to the duct, and is used to derive a criterion for a stabilized wave configuration, in which a function describing the competition between the source terms is of central importance. The influence of area change and friction force on the stability of a detonation wave within the supersonic moving duct is analysed by a series of numerical computations.

2. Theoretical model

To consider the essential features of supersonic engines and the ram accelerator, a short duct geometry is used that consists of an inlet diffuser and a nozzle section, shown in figure 1. The internal transient flow can be described by quasi-one-dimensional Euler equations that take into account the effects of friction and exothermic reaction. The governing equations are derived below, to designate their difference from those for the body at rest found in the literature.

Because of the motion of the body, the flow area A varies with both space and time (see figure 1):

$$A = A(x, t) = A(x - X_p(t)), \tag{1}$$

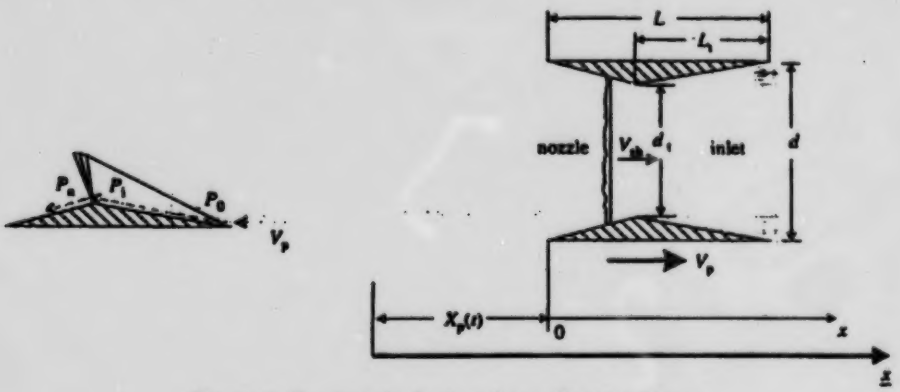

Figure 1. Supersonic duct and coordinate systems.

where $(\underline{x},\underline{t})$ are the laboratory coordinates and $X_p(\underline{t})$ is the trajectory of the body. Upon applying the control volume analysis to a fluid element from $\underline{x}$ to $\underline{x}+\mathrm{d}\underline{x}$, one obtains the continuity, momentum and the energy equations:

$$\frac{\partial}{\partial \underline{t}}(\rho A)+\frac{\partial}{\partial \underline{x}}(\rho A v)=0, \tag{2}$$

$$\frac{\partial}{\partial \underline{t}}(\rho A v)+\frac{\partial}{\partial \underline{x}}(\rho A v^2+pA)=p\frac{\partial A}{\partial \underline{x}}+fA \tag{3}$$

and

$$\frac{\partial}{\partial \underline{t}}(\rho A \underline{e})+\frac{\partial}{\partial \underline{x}}[v(\rho A \underline{e}+pA)]=V_p p\frac{\partial A}{\partial \underline{x}}+V_p fA+\dot{q}A, \tag{4}$$

where the variables ρ, p, v, and $\underline{e}$ are the density, pressure, particle velocity and the sum of the internal and kinetic energy, i.e.

$$\underline{e}=\frac{1}{\gamma-1}\frac{p}{\rho}+\tfrac{1}{2}v^2. \tag{5}$$

The variable V_p denotes the body velocity, which is defined as

$$V_p=\frac{\mathrm{d}X_p(\underline{t})}{\mathrm{d}\underline{t}}. \tag{6}$$

The source terms f and $\dot{q}$ represent a friction force and a rate of heat transfer, respectively. The first term on the right-hand side of the momentum equation (3) is attributed to the pressure acting on the periphery of the fluid element caused by the area change. Because of the motion of the body, the two power terms induced by the body velocity multiplied by the periphery pressure and the friction force appear on the right-hand side of the energy equation (4). Thus, although the effect of the body motion does not enter explicitly into the continuity and the momentum equations, it does change the energy equation.

To make a numerical computation feasible and to derive the criterion for a detonation wave standing in the duct, the laboratory frame is transformed into a body-attached coordinate system (see figure 1):

$$x=\underline{x}-X_p(\underline{t}); \quad t=\underline{t}. \tag{7}$$

From (7) one obtains

$$u = v - V_p \tag{8}$$

and

$$\frac{\partial}{\partial t} = \frac{\partial}{\partial t} - V_p \frac{\partial}{\partial x}; \quad \frac{\partial}{\partial \xi} = \frac{\partial}{\partial x}, \tag{9}$$

where u denotes the flow velocity with respect to the body. Upon replacing the transformations (7)–(9) into (1)–(5), the governing equations in the body-attached frame are obtained:

$$\frac{\partial \rho}{\partial t} + \frac{\partial (\rho u)}{\partial x} = -\frac{1}{A}\frac{\mathrm{d}A}{\mathrm{d}x}\rho u, \tag{10}$$

$$\frac{\partial (\rho u)}{\partial t} + \frac{\partial}{\partial x}(\rho u^2 + p) = -\frac{1}{A}\frac{\mathrm{d}A}{\mathrm{d}x}\rho u^2 + f - \rho a_p \tag{11}$$

and

$$\frac{\partial (\rho e)}{\partial t} + \frac{\partial}{\partial x}[u(\rho e + p)] = -\frac{1}{A}\frac{\mathrm{d}A}{\mathrm{d}x}u(\rho e + p) + \dot{q} - \rho u a_p, \tag{12}$$

where e is the sum of the internal and kinetic energies with respect to the body and a_p denotes the body acceleration: $a_p = \mathrm{d}V_p/\mathrm{d}t$. The last term on the right-hand side of (11) and (12) represents the pseudo-force and its power for the non-inertial frame.

To solve the governing equations (10)–(12) the source terms of area change $\mathrm{d}A/(A\,\mathrm{d}x)$, friction force f, exothermic reaction $\dot{q}$ and the body acceleration a_p must be specified. For the present study we are interested only in a qualitative analysis of the competition between these source terms. It is therefore sufficient to choose these source terms as follows. First, the area change is assumed to be described by

$$\frac{1}{A}\frac{\mathrm{d}A}{\mathrm{d}x} = \frac{\pi}{L - L_1}\ln\frac{d_t}{d}\sin\frac{\pi x}{L - L_1} \quad \text{for} \quad 0 \leqslant x \leqslant L - L_1 \tag{13a}$$

and

$$\frac{1}{A}\frac{\mathrm{d}A}{\mathrm{d}x} = \frac{\pi}{L_1}\ln\frac{d_t}{d}\sin\frac{\pi(2L_1 - L + x)}{L_1} \quad \text{for} \quad L - L_1 < x \leqslant L, \tag{13b}$$

and elsewhere $\mathrm{d}A/\mathrm{d}x = 0$. The parameters L, L_1, d, d_t are the length of the duct, length of the inlet section, outside diameter of the duct and the throat diameter. The expressions (13) smooth the conical area change and reduce numerical noise.

The friction force has the form

$$f = -\frac{4c_f}{D_h}\tfrac{1}{2}\rho u|u|, \tag{14}$$

where the minus sign indicates the acting direction of the friction on the gas that is opposite to the flow velocity with respect to the body. The parameter D_h usually denotes a hydraulic diameter in a straight duct. In the present study it is regarded as a factor for the magnitude of the friction force. The parameter c_f is the Fanning friction factor. For the unsteady flow behind the shock wave, we follow Zeldovich *et al.* (1988) in assuming that the friction factor obeys the Blasius law

$$c_f = 0.3164/Re^{0.25}, \tag{15}$$

where the Reynolds number is defined as

$$Re = D_h \rho |u|/\mu \tag{16}$$

and the dynamic viscosity μ follows the Sutherland formula (see for example, White 1974).

For the exothermic reaction a single-step Arrhenius law is assumed, i.e.

$$\frac{\mathrm{d}\beta}{\mathrm{d}t} = -w/\rho = -k\beta\,\mathrm{e}^{-E/RT}, \tag{17}$$

in which

$$RT = p/\rho. \tag{18}$$

Thus, the rate of heat release can be written as

$$\dot{q} = Qw. \tag{19}$$

Here the variables T and β denote the temperature and the reactant mass fraction, with $\beta = 1$ in the unburned mixture. Q, w, E, k and R are the effective energy release per unit mass, depletion rate of the reactant mass, activation energy, pre-exponential factor and the specific gas constant, respectively.

Finally, the body acceleration is determined in terms of the thrust divided by the body mass according to the Newtonian law, i.e.

$$a_p = \frac{I}{m} = \frac{1}{m}\left[\int_0^{x_{sh}} p\,\mathrm{d}A + \tfrac{1}{4}\pi D_h \int_0^L A^{\frac{1}{2}} f\,\mathrm{d}x + D_w\right], \tag{20}$$

where the variable x_{sh} denotes the shock front position. The thrust I is the horizontal component of the force acting on the internal body surface. Although the presence of the oblique shock attached to the inlet cannot be modelled directly in a one-dimensional formulation, a supersonic wave drag D_w is induced to effectively account for the contribution of the oblique shock to the pressure acting on the inlet section. For the qualitative analysis, we assume a Cartesian geometry and neglect reflected waves (see figure 1), so the drag D_w is determined by the pressure behind the oblique shock wave and the Prandtl–Meyer expansion at the throat, i.e.

$$D_w = (p_i - p_n)(A_0 - A_t) \quad \text{for} \quad x_{sh} < 0, \tag{21a}$$

$$D_w = p_i(A_0 - A_t) - p_n[A(x_{sh}) - A_t] \quad \text{for} \quad 0 \leqslant x_{sh} \leqslant L - L_i \tag{21b}$$

and

$$D_w = p_i[A_0 - A(x_{sh})] \quad \text{for} \quad L - L_i < x_{sh} \leqslant L, \tag{21c}$$

where the pressure p_i and p_n are derived from the relations of oblique shock waves and the Prandtl–Meyer expansion theory respectively (see, for example, Liepmann & Roshko 1957). The influence of the unsteady expansion on D_w is negligible because the pressure behind the expansion at the throat is one to two orders of magnitude less than that behind the oblique shock wave for the supersonic flow considered.

The governing equations (10)–(12) are then combined with (13)–(21) to be expressed in the conservative form and solved numerically by using a higher-order extension of Godunov's method with Strang's splitting algorithm. In this study, the diameter ratio of the throat to the body d_t/d and the initial body Mach number (i.e. $M_{p0} = V_{p0}/c_0$) are variables, whereas the other projectile parameters are fixed as follows: $L_i/L = 0.6$, $d/L = 0.84$, $L = 120$ mm, $m = 51$ g, $p_0 = 11$ bar. The dimensionless mixture parameters are $\gamma = 1.2$, $Q = 50$, which give a CJ detonation velocity of $D_{CJ} = 6.2c_0$, and the activation energy $E = 22$. Note that this value of the activation energy is far below the detonation stability limit for a planar CJ detonation in a straight duct without friction ($E_c = 25$). The detonation is initiated

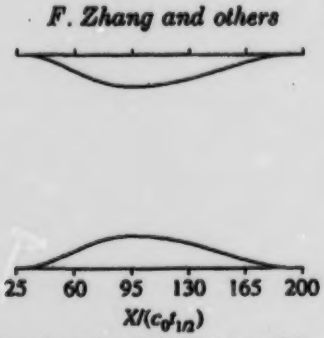

Figure 2. Shape and length scale of the duct used in numerical simulation.

at the exit of the nozzle by imposing a local region of high pressure and temperature. The shape and length scale of the duct used in the computations are shown in figure 2.

3. Criterion for a stationary-wave configuration

From the classical mechanical point of view, a detonation wave can be stationary in a supersonic body only if the body and the detonation velocities are equal and the body acceleration vanishes, i.e.

$$V_p = V_{sh}; \quad a_p = 0. \tag{22}$$

Any acceleration of the body will result in a movement of the detonation front with respect to the body, and vice versa. The question arises as to how the internal flow adjusts itself to satisfy the kinematic and dynamic balance conditions (22). To answer this question it is sufficient to look at the state downstream of the shock front along the characteristic C^+, because any disturbance from downstream acting on the shock front is transmitted along a right running acoustic wave. Upon manipulating (10)–(12), the characteristic equation along C^+ can be obtained, i.e.

$$C^+: \quad \mathrm{d}x/\mathrm{d}t = u + c \tag{23}$$

and

$$(\mathrm{d}p/\mathrm{d}t)^+ + \rho c(\mathrm{d}u/\mathrm{d}t)^+ = \psi - \rho c a_p, \tag{24}$$

where

$$\psi = (\gamma-1)\dot{q} - \frac{1}{A}\frac{\mathrm{d}A}{\mathrm{d}x}\rho c^2 u + fc\left[1-(\gamma-1)\frac{u}{c}\right] \tag{25}$$

and

$$\left(\frac{\mathrm{d}}{\mathrm{d}t}\right)^+ = \frac{\partial}{\partial t} + (u+c)\frac{\partial}{\partial x}.$$

The function ψ represents the rates of energy production caused by the source terms for exothermic reaction, area change and friction, and has been called a 'competition' function (Zhang & Lee 1994) because its value describes the competing effect of the energy production under the source terms involved. A positive ψ indicates that a compression wave propagates along the characteristic C^+ to amplify the shock, whereas a negative value denotes a rarefaction wave that attenuates the shock. If the competition between the source terms interacting with the shock front results in the flow's having a right running characteristic, defined by $\mathrm{d}x/\mathrm{d}t = 0$ along which a steady state exists, such a characteristic must then correspond to the sonic locus x_s (see (23)) on which the right-hand side of (24) vanishes. A sufficient condition for disappearance of the right-hand side of (24) is $\psi = 0$ and $a_p = 0$. So one can use a control-volume analysis between the two steady states, i.e. at the sonic locus and at

the body front, to obtain a steady-wave solution. Thus, a condition for a steady solution (i.e. $a_p = 0$) is

$$l_p^+ - v(x_s) = -u(x_s) = c(x_s), \tag{26}$$

$$\psi(x_s) = 0, \tag{27}$$

where the variable v refers to the flows velocity in the laboratory coordinates. Upon substituting (22) into (26) one obtains

$$l_{sh}^+ - v(x_s) = c(x_s). \tag{28}$$

The criterion (27), (28) is a saddle-point condition, and provides a sonic choking plane with respect to the shock front at which the rates of energy production caused by the source terms for exothermic reaction, area change and friction attain a balance. Whether the stabilized detonation wave is overdriven or has a velocity deficit with respect to the CJ detonation value depends on the sign and the magnitude of area change and friction force at the stabilized position. For a steady-wave solution with a velocity deficit, (27) indicates that a portion of chemical energy is left at the sonic locus and released in the supersonic flow downstream. On the other hand, if a steady solution exists for an overdriven detonation wave, the chemical energy release is completed upstream in the subsonic flow régime. The sonic matching is then realized through the balance of the energy change rates caused by area change and friction. Note that the criterion (27), (28) also implies steady flow ahead of the shock front because the acceleration of the projectile vanishes and its velocity then remains constant.

4. Effect of area change on detonation stability

In order to understand clearly the competing effect of the individual source terms with the exothermic reaction on the stability of a detonation wave, we first focus on the source term for area change and assume the friction force $f = 0$.

The influence of area change on a detonation wave manifests itself through the interaction of the area change with the leading shock front and the reacting flow, and depends on the flow state ahead of the shock front. The rules of the interaction between area change and a shock front can be obtained by using Whitham's method (see Appendix A). For subsonic flow in a duct, the rule is the same as in the case of a quiescent gas ahead of the front, that is, the shock wave is attenuated in a diverging duct and amplified in a converging duct. For a supersonic flow ahead of the front, the rule provides an opposite interaction effect, and states that the shock wave is amplified in a diverging duct and attenuated in a converging duct. The effect of the interaction between the area change and the reacting flow is to create compression or rarefaction waves, dictated by the sign of the area change term $-\rho c^2 u\, \mathrm{d}A/(A\, \mathrm{d}x)$ in the function ψ defined in (25). A positive sign indicates a compression wave that amplifies the detonation wave, whereas a negative sign refers to a rarefaction wave that attenuates the detonation wave. Note that a key factor in the area-change term is the sign of the reacting flow velocity u that is determined by the flow velocity ahead of the shock, the shock velocity (see Appendix A) and the reacting expansion.

Taking into account the interaction effect of the area change with the shock front and the reacting flow, we obtain the rules for a detonation wave propagating through flow in a duct of varying cross section as follows:

1. If a detonation wave propagates in a duct with subsonic flow, whose velocity is small enough that the reacting flow remains in the propagation direction of the

detonation wave, the detonation wave is attenuated in a diverging duct and amplified in a converging duct. In a converging duct, an overdriven detonation will be amplified continuously and cannot be stationary in the duct, because the positive area-change term remains alone in the function ψ at the sonic locus and the criterion (27), (28) fails.

2. If a detonation wave propagates in a duct with opposed supersonic flow, whose velocity is sufficiently large that the reacting flow is in the opposite direction to the detonation propagation and yet is not choked immediately behind the shock front, the rule is completely different. The detonation wave is now amplified in a diverging duct and attenuated in a converging duct. In a diverging duct, an overdriven detonation will be amplified continuously and cannot stand in the duct owing to the failing of the criterion (27), (28).

According to the rules stated above, a detonation wave cannot be stabilized in the inlet section of the supersonic duct studied whose speed is of the order of the CJ detonation speed. Owing to the diverging geometry it becomes overdriven and finally expelled out of the duct front. This phenomenon is in agreement with the classical supersonic diffuser instability. The body deceleration caused by the diverging geometry (see (20)) will speed up the expelling process. As the detonation wave propagates in the nozzle where the area change is converging towards the throat, the post-shock temperature drops and the detonation velocity has a deficit with respect to the Chapman–Jouguet value. In this case, the negative value of the area change term in the function ψ represents a rate of energy withdrawal that competes with the chemical heat release, so that the sonic matching criterion (27)–(28) might be satisfied. However, it is well established in one-dimensional detonation theory that an oscillatory-wave solution occurs as the activation energy of a gaseous mixture is increased beyond a stability limit (see, for example, Fickett & Wood 1966). Decreasing the post-shock temperature has the same effect on the rate of the chemical reaction as increasing the activation energy, because the reaction rate in a gaseous mixture is proportional to $e^{-E/RT}$. Thus, increasing the rate of area change in the supersonic nozzle in general leads the criterion (27), (28) to fail, and drives the detonation towards instability.

If the area change of the supersonic nozzle is so small that the reduction of the post-shock temperature is not sufficient to excite any instability mode, the detonation can then be stabilized within the nozzle (see figure 3). In this example the diameter ratio of throat to body is $d_t/d = 0.7$ and the initial projectile Mach number $M_{p0} = 5.8$. After an initial overshoot, the detonation Mach number (i.e. $M_{sh} = V_{sh}/c_0$) decays. The high pressure behind the shock front overcomes the wave drag and creates a positive thrust that accelerates the body. As the body Mach number (i.e. $M_p = V_p/c_0$) approaches M_{sh}, the detonation penetrates furthest into the nozzle, and a_p nears its maximum. Owing to the projectile acceleration, M_p increases above M_{sh} and the detonation front then moves downstream. This in turn causes a_p to decrease. Meanwhile, M_{sh} is increased as the detonation front moves leeward because of the reduction of the rate of area change $dA/(A\,dx)$ and the pressure ahead of the front, which raises the pressure ratio across the shock front. Finally, the detonation wave is stabilized at the position where $M_p = M_{sh}$ and $a_p = 0$ are satisfied. The velocity of the stabilized detonation has a deficit of $\Delta V_{sh} = -0.2c_0$ with respect to the CJ detonation velocity (i.e. $D_{CJ} = 6.2$). In the entire transient process, the Mach numbers of the product flow (corresponding to the position where the reactant is consumed as up to a fraction of 10^{-3}) with respect to the shock front and to the body

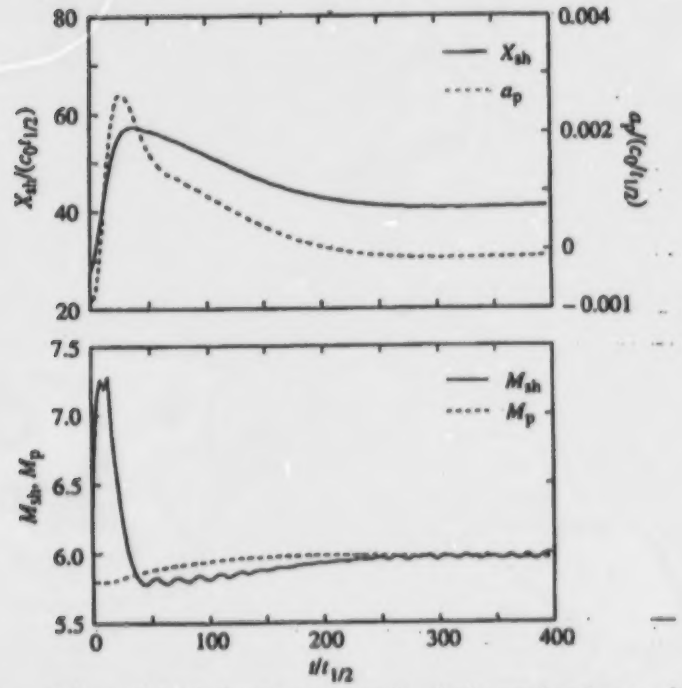

Figure 3. Time evolution of shock front trajectory X_{sh}, body acceleration a_p, detonation Mach number M_{sh} and body Mach number M_p; duct parameters are: $d/L = 0.84$, $L_1/L = 0.6$, $d_1/d = 0.7$, $M_{p0} = 5.8$; detonation parameters are: $\gamma = 1.2$, $Q = 50$, $E = 22$; $t_{\frac{1}{2}}$ is the standard half reaction time; friction force $f = 0$.

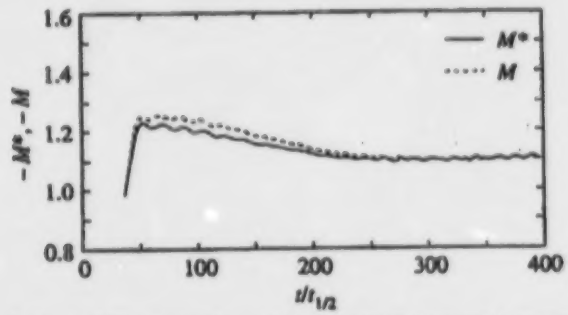

Figure 4. Time evolution of Mach number of the product flow with respect to shock (i.e. M^*) and to body (i.e. M). Parameters are the same as those in figure 3.

(i.e. M^* and M respectively) are supersonic owing to the influence of the area change (see figure 4). They asymptotically approach the same value as the detonation front becomes stabilized. The slightly supersonic asymptotic value is attributed to the fact that burning is completed in the expansion behind the sonic choking plane described by (27), (28). Thus, this example clearly demonstrates the sonic matching criterion (27), (28) as a confinement to the internal flow when a stabilized-wave configuration is established.

In the case of a very large area change, the detonation decays after initiation and

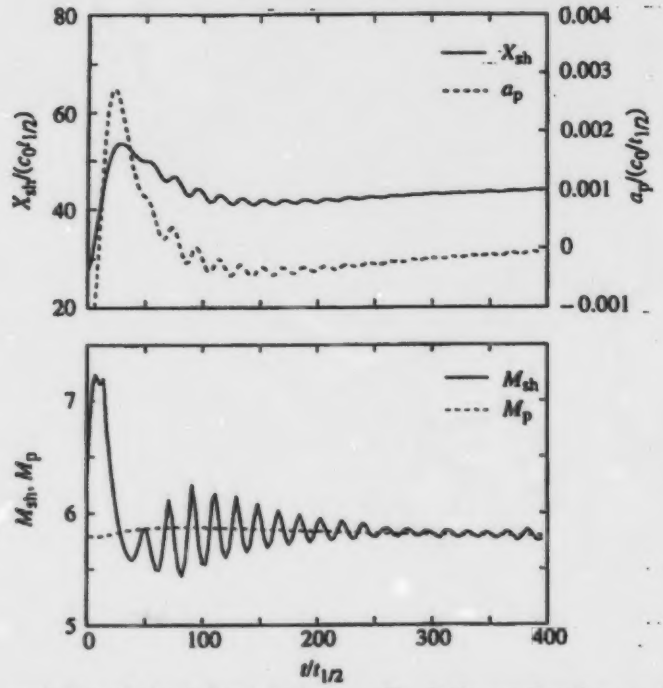

Figure 5. Time evolution of shock front trajectory X_{sh}, body acceleration a_p, detonation Mach number M_{sh} and body Mach number M_p. Parameters are the same as those in figure 3 except for $d_t/d = 0.6$.

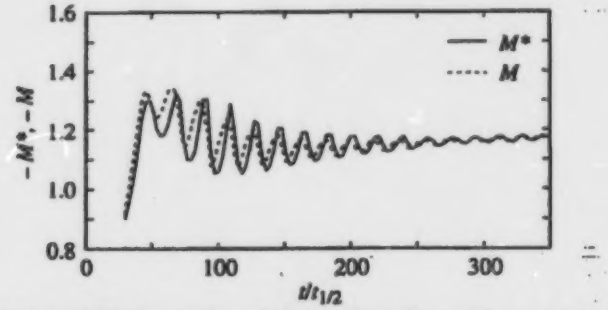

Figure 6. Time evolution of Mach number of the product flow with respect to shock (i.e. M^*) and to body (i.e. M). Parameters are the same as those in figure 5.

eventually fails. However, for a range of intermediate values of the area change, the detonation executes an oscillatory behaviour as it propagates (see figure 5 with $d_t/d = 0.6$). Whether or not it can be restabilized depends greatly on the rate of area change $\mathrm{d}A/(A\,\mathrm{d}x)$ during the transient motion of the detonation wave. In figure 5 we choose the same initial projectile Mach number (i.e. $M_{p0} = 5.8$) as that used in figure 3. The detonation wave penetrates to the furthest position ($x = 52$) where $M_p = M_{sh}$, attained while $a_p > 0$. The oscillation of the wave front is damped as it returns downstream, owing to the reduction of the rate of area change and the increase of the pressure ratio across the front. Finally, the detonation wave is restabilized in an

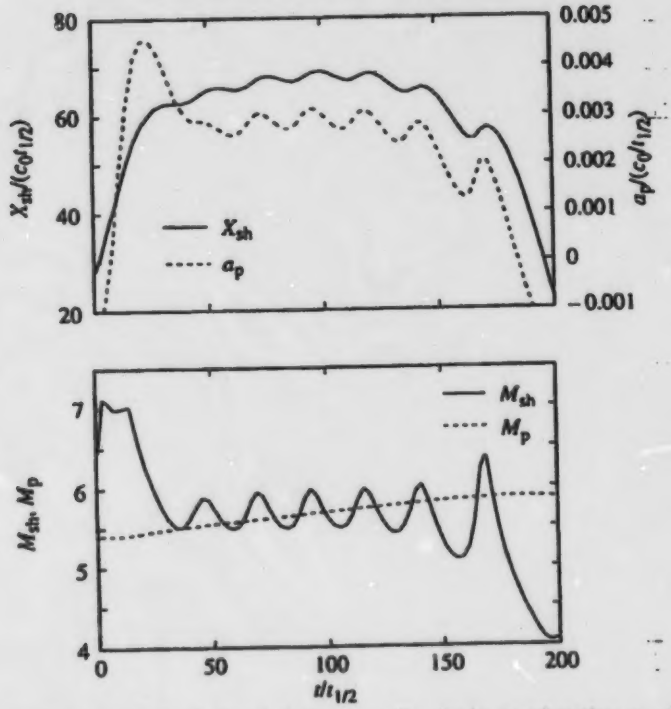

Figure 7. Time evolution of shock front trajectory X_{sh}, body acceleration a_p, detonation Mach number M_{sh} and body Mach number M_p. Parameters are the same as those in figure 3 except for $d_1/d = 0.6$, $M_{p0} = 5.4$.

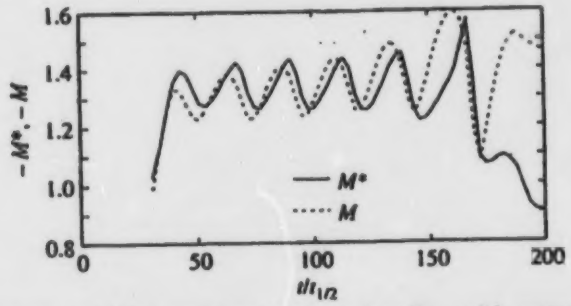

Figure 8. Time evolution of Mach number of the product flow with respect to shock (i.e. M^*) and to body (i.e. M). Parameters are the same as those in figure 7.

oscillatory fashion, and a standing-wave configuration exists in a cycle-averaged sense with a mean velocity deficit of $\Delta V_{sh} = -0.4c_0$. The Mach number of the product flow at the end of reaction approaches its supersonic asymptotic value (see figure 6), which is slightly greater than that shown in figure 4 because in the present case more unburned reactant is left behind the sonic locus caused by the larger area change at the stabilized position. However, upon reducing the initial Mach number to $M_{p0} = 5.4$, the penetration depth of the detonation wave is increased beyond $x > 62$ where the amplitude of the area change $dA/(A\,dx)$ is sufficiently large to induce rapid growth of the oscillation (see figure 7). As a consequence, the detonation velocity

cannot recover and the wave is swallowed out of the exit of the nozzle, while the Mach number of the product flow at the end of the reaction runs away from unity (see figure 8).

The computations discussed above are based on a very low activation energy (i.e. $E = 22$), for which the detonation wave would be highly stable if propagated in a straight duct. If the mixture has an activation energy beyond the detonation stability limit (i.e. $E_c = 25$ with the other mixture parameters fixed), an oscillatory solution could occur even for a small area change. The oscillatory phenomenon of the detonation wave in the supersonic nozzle studied here is essentially the same as in firing a sphere into a detonable gas (Behrens *et al.* 1965), where the expansion of the reacting flow is induced by the area change between the sphere and the bow shock at the sphere front. As the sphere speed is less than a critical value, oscillation patterns are observed in the detonating flow.

5. Effect of friction on detonation stability and final body velocity

Let us consider a detonation wave propagating in a straight duct with friction (i.e. $dA/dx = 0$). Friction force on the gas acts in the opposite direction to the flow velocity with respect to the duct wall. As a detonation wave propagates into opposed flow, there exists friction force both ahead of the shock front in the propagation direction of the detonation wave and behind the shock front. Analogous to the case of source term for area change, the influence of friction on a detonation wave also manifests itself through two aspects: the interaction of friction with the shock front and with the reacting flow. Extending the Whitham's method to a non-reactive shock wave moving through steady frictional flow in a duct (see Appendix B), we obtain the interaction rules of friction with a shock front, that is, the shock wave is attenuated in a frictional duct with opposed subsonic flow, and amplified as opposed flow ahead of the shock front is supersonic. The interaction effect of the friction with the reacting flow is to induce compression or rarefaction waves, determined by the sign of the friction term $fr[1-(\gamma-1)u/c]$ in the function ψ defined in (25), in which the friction force is opposed to the direction of the reacting flow velocity u (see (14)). Thus, a key factor in the friction term is the sign of the reacting flow velocity that is determined by the flow velocity ahead of the shock, the shock velocity (see Appendix A), and the reacting expansion. If the reacting flow velocity with respect to the body is in the same direction as that of the detonation propagation, the friction force acting on the reacting flow is opposed to the detonation propagation and hence attenuates the detonation wave. If the reacting flow velocity is in the opposite direction to the detonation propagation, the friction force acts towards the shock front and thus amplifies the detonation wave.

Upon combining the interaction effects of the friction with the shock front and the reacting flow, the rules for a detonation wave propagating through flow in frictional ducts can be obtained as follows:

1. If a detonation wave propagates in a duct with subsonic flow, whose velocity is small enough that the reacting flow remains in the propagation direction of the detonation wave, the detonation wave is attenuated and its stability is decreased.

2. If a detonation wave propagates in a duct with opposed supersonic flow, whose velocity is sufficiently large that the reacting flow is in the opposite direction to the detonation propagation and yet is not choked immediately behind the shock front, the detonation wave is amplified and its stability is increased. An overdriven

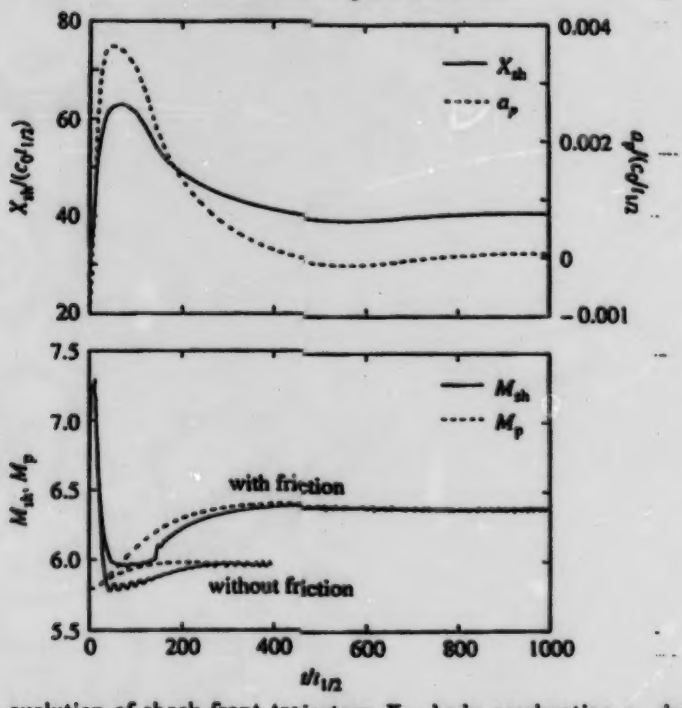

Figure 9. Time evolution of shock front trajectory X_{sh}, body acceleration a_p, detonation Mach number M_{sh} and body Mach number M_p. Parameters are the same as those in figure 3 but with friction factor ratio of $c_{f2}/c_{f1} = 40$.

detonation will be amplified continuously and cannot be stationary in the duct, because the positive value of the friction term remains alone in the function ψ at the sonic locus and the criterion (27), (28) fails.

On the basis of the rules stated above, a detonation wave is amplified and hence more stabilized in the nozzle of the supersonic duct studied whose velocity is of the order of the CJ detonation speed. Concerning the body velocity, one must consider the friction force that acts on the internal surface of the nozzle towards the nozzle exit and hence creates a deceleration of the body (see (20)). This deceleration competes with the acceleration created by the area-change term in which the pressure is enhanced by the friction acting on the reacting flow. If one properly chooses the duct geometry and initial conditions so that the sonic matching can be realized through the balance of the positive terms for the friction and the exothermic reaction (it vanishes for overdriven detonations) with the negative term for the area change in the function ψ, the body velocity is then increased by adding friction because at the stabilized position the body velocity must equal the detonation velocity (see (22)).

The numerical calculation indicates that the effect of skin friction (i.e. with a small friction factor) is not significant and provides only a slight increase of the detonation velocity compared with the results without friction. Increasing the roughness behind the shock front can overcome the velocity deficit caused by the area change and drive the detonation into the overdriven régime (see figure 9). In this example, the same parameters as in figure 3 are used, but friction is added with the ratio of friction

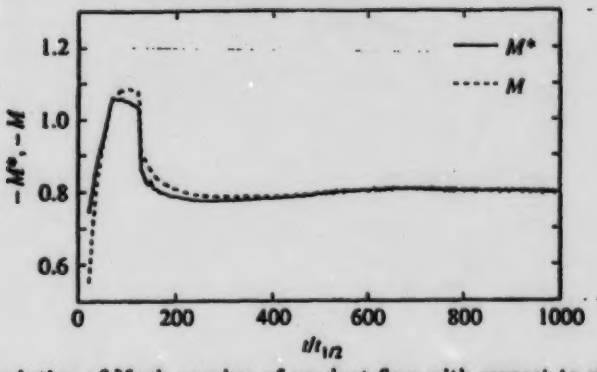

Figure 10. Time evolution of Mach number of product flow with respect to shock (i.e. M^*) and to body (i.e. M). Parameters are the same as those in figure 9.

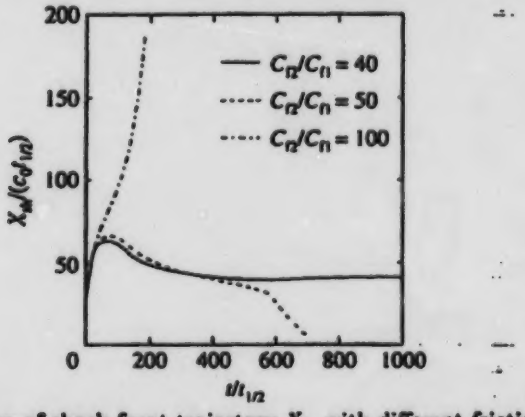

Figure 11. Time evolution of shock front trajectory X_{sh} with different friction factor ratios. Other parameters are the same as those in figure 3.

factors behind and ahead of the shock front $c_{f2}/c_{f1} = 40$. At the end of the transient development, the stabilized body Mach number M_p, which equals the stabilized detonation Mach number M_{sh}, is increased from $M_p = 6.0$ (without friction) to $M_p = 6.4$ (with friction), which represents a 7% overdrive of the CJ detonation. The overdriven feature of the detonation is clearly indicated by the subsonic Mach number of the product flow as the detonation front approaches its stabilized position (see figure 10).

Note that there exists an upper limit of the friction factor beyond which a stabilized-wave configuration cannot be attained with the given duct geometry and initial conditions. The shock front trajectory, shown in figure 11, indicates that by increasing the friction factor ratio to $c_{f2}/c_{f1} = 50$, the detonation front penetrates so far into the throat that the body accelerates to well above the velocity of the detonation front as it moves leeward. Eventually, the detonation front is swallowed out of the nozzle (i.e. at $x_{sh} = 27.4 c_0 t_1$). On further increasing the friction factor ratio to $c_{f2}/c_{f1} = 100$, the detonation front passes through the throat and is expelled out of the inlet. In both cases, the stabilized detonation wave can be established only if the area change or the initial body velocity is adjusted to make the transient process terminate at the position where the criterion (27), (28) is satisfied.

6. Conclusions

In a duct of varying cross section with the presence of friction, the amplification or attenuation of a detonation wave depends on the flow ahead of the wave front. If the unburned flow is subsonic and its velocity is small enough that the reacting flow remains in the propagation direction of the detonation wave, the detonation wave is attenuated in a diverging duct and amplified in a converging duct, whereas friction behind the shock front leads to the attenuation of the detonation wave. If the unburned flow is opposed and supersonic, and its velocity is sufficiently large that the reacting flow is opposite to the direction of the detonation propagation, the diverging geometry can drive the detonation wave towards amplification, whereas the converging geometry leads it to attenuation. In this case, the effect of the friction behind the shock front is to amplify the detonation wave. As a rule, the stability of the detonation front is decreased as the detonation wave attenuates, and increased by its amplification. The stationary detonation wave in the duct can be analysed by replacing the classical CJ criterion with a generalized sonic choking condition that takes into account the competition between area change, friction and heat release.

In this paper we have chosen a supersonic moving duct as an example to elucidate the foregoing conclusions. The analysis shows that in a supersonic nozzle, raising the rate of area change drives a detonation wave towards instability, whereas adding friction behind the shock front increases the detonation velocity and stabilizes the detonation wave. Thus, a novel concept is to add roughness in the nozzle behind the shock front to improve the stability of the detonation front and to increase the final velocity of the body.

Appendix A. Shock wave through flow in ducts of varying cross section

Following Chester (1960) and Han & Yin (1993) in applying the method by Whitham (1958) for a non-reacting shock wave moving through non-uniform steady flow in a duct of varying cross section, we obtain the relations describing the change of the shock Mach number M_s, the area change, and the flow Mach number ahead of the shock (i.e. M_1):

$$\left.\begin{aligned} \mathrm{d}M_s &= G\,\mathrm{d}M_1 \\ \frac{\mathrm{d}A}{A} &= \frac{M_1^2-1}{1+\frac{1}{2}(\gamma-1)M_1^2}\frac{\mathrm{d}M_1}{M_1} \end{aligned}\right\} \tag{A 1}$$

where

$$G = \left(\frac{M_1}{E}+\tfrac{1}{2}(\gamma-1)\frac{M_1M_2}{E}-\frac{M_2}{F}-\frac{M_1^2-1}{EM_1}\frac{M_2}{M_2+1}\right)\Big/\left(\frac{2M_2}{(\gamma+1)F}\left(1+\frac{1}{M_s^2}\right)+\frac{4M_s}{2\gamma M_s^2-(\gamma-1)}\right) \tag{A 2}$$

$$M_2 = \frac{(\gamma+1)M_1M_s+2(M_s^2-1)}{[2\gamma M_s^2-(\gamma-1)]^{\frac{1}{2}}[(\gamma-1)M_s^2+2]^{\frac{1}{2}}}, \tag{A 3}$$

$$E = 1+\tfrac{1}{2}(\gamma-1)M_1^2, \quad F = M_1+\frac{2(M_s^2-1)}{(\gamma+1)M_s^2},$$

where the flow Mach number with respect to the duct is denoted by M, and the shock

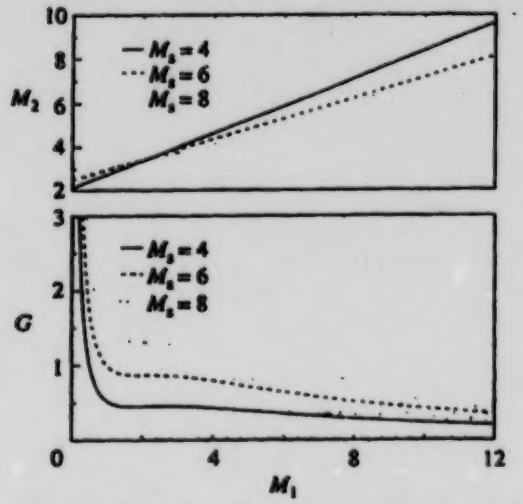

Figure 12. Variation of function G and flow Mach number immediately behind shock front M_s with flow Mach number ahead of shock front $M_1 > 0$.

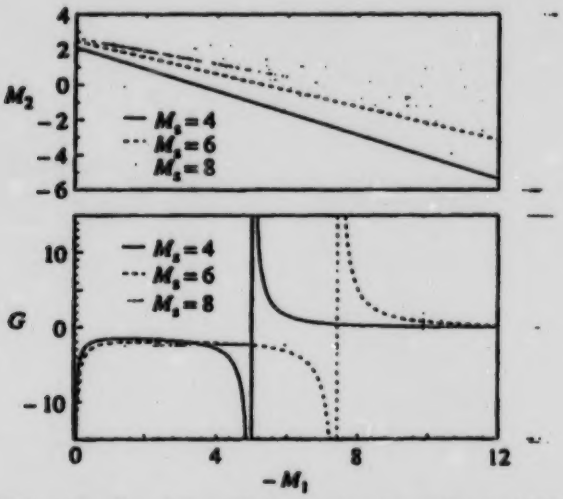

Figure 13. Variation of function G and flow Mach number immediately behind shock front M_s with flow Mach number ahead of shock front $M_1 < 0$.

Mach number relative to the flow ahead of the front by M_s. The subscript 1 refers to the state ahead of the front, while the subscript 2 defines the state immediately behind the front.

The behaviour of the function G and the flow Mach M_2 varying with M_1 and M_s are displayed in figures 12 and 13, where figure 12 is for the case of M_1 being in the positive x-direction (i.e. the same as that of M_s), and figure 13 represents the case of M_1 in the negative x-direction (i.e. opposite to that of M_s). Where $M_1 > 0$, both $M_2 > 0$ and $G > 0$, while for $M_1 < 0$, the sign of M_2 is changed from positive to negative at the point where $|M_1| = 2(M_s^2 - 1)/((\gamma + 1)M_s) < M_s$. As seen in figure 13,

$G < 0$ up to the point where $M_2 \to -1$, at which the flow chokes immediately behind the shock front owing to the influence of the area change, which stands on the last term in the numerator of the function G. After the discontinuity in G at $M_2 = -1$, G becomes positive.

Once the behaviour of the function G is known, the rules for the interaction of the area change with the shock front can be obtained from (A 1). They are listed below.

For the case where M_1 is in the positive x-direction:

$$\left.\begin{array}{llll} \mathrm{d}A > 0 & \mathrm{d}M_1 < 0 & \mathrm{d}M_2 < 0 \\ \mathrm{d}A < 0 & \mathrm{d}M_1 > 0 & \mathrm{d}M_2 > 0 \end{array}\right\} \quad \text{for} \quad M_1 < 1; \tag{A 4}$$

$$\left.\begin{array}{llll} \mathrm{d}A > 0 & \mathrm{d}M_1 > 0 & \mathrm{d}M_2 > 0 \\ \mathrm{d}A < 0 & \mathrm{d}M_1 < 0 & \mathrm{d}M_2 < 0 \end{array}\right\} \quad \text{for} \quad M_1 > 1; \tag{A 5}$$

whereas in the case where M_1 is in the negative x-direction and within the range of $G < 0$:

$$\left.\begin{array}{llll} \mathrm{d}A > 0 & \mathrm{d}M_1 > 0 & \mathrm{d}M_2 < 0 \\ \mathrm{d}A < 0 & \mathrm{d}M_1 < 0 & \mathrm{d}M_2 > 0 \end{array}\right\} \quad \text{for} \quad |M_1| < 1; \tag{A 6}$$

$$\left.\begin{array}{llll} \mathrm{d}A > 0 & \mathrm{d}M_1 < 0 & \mathrm{d}M_2 > 0 \\ \mathrm{d}A < 0 & \mathrm{d}M_1 > 0 & \mathrm{d}M_2 < 0 \end{array}\right\} \quad \text{for} \quad |M_1| > 1. \tag{A 7}$$

The rules (A 4)–(A 7) clearly indicate that the effects of area change on a shock front in a subsonic flow is the opposite of the effects that occur when the flow ahead of the front is supersonic. For subsonic flow in a duct, the rule is the same as in the case of a quiescent gas ahead of the front, that is, the shock wave is attenuated in a diverging duct and amplified in a converging duct. However, for a supersonic flow ahead of the front, the shock wave is amplified in a diverging duct, and attenuated in a converging duct.

Appendix B. Shock wave through flow in frictional ducts

Analogous to the case of area change, the interaction of friction with a shock front is analysed by extending Whitham's method to a non-reactive shock wave propagating through steady frictional flow in a duct. We follow Whitham (1958) in applying the characteristic equation at the shock front:

$$M_2 \frac{\mathrm{d}u_2}{u_2} + \frac{\mathrm{d}p_2}{\gamma p_2} + \frac{2c_{\mathrm{f}2}}{D_{\mathrm{h}2}} \frac{M_2|M_2|\,[1-(\gamma-1)M_2]}{M_2+1}\mathrm{d}x = 0, \tag{B 1}$$

where the flow velocity with respect to the duct is denoted by u, and the shock trajectory with respect to the duct is denoted by x. The other notations are defined as in Appendix A and the previous sections. The shock relations with flow ahead are the same as used in Appendix A, whereas the governing equations for adiabatic, frictional steady flow ahead of the shock front can be written as

$$\rho_1 u_1 = \text{const.} \tag{B 2}$$

$$\tfrac{1}{2}\mathrm{d}u_1^2 + \mathrm{d}p_1/\rho_1 + (2c_{\mathrm{f}1}/D_{\mathrm{h}1})\,u_1|u_1|\,\mathrm{d}x = 0 \tag{B 3}$$

and

$$c_1^2 + \tfrac{1}{2}(\gamma-1)\,u_1^2 = c_{\mathrm{T}}^2. \tag{B 4}$$

where the constant c_{T} is the stagnation sound speed in adiabatic flow. Upon

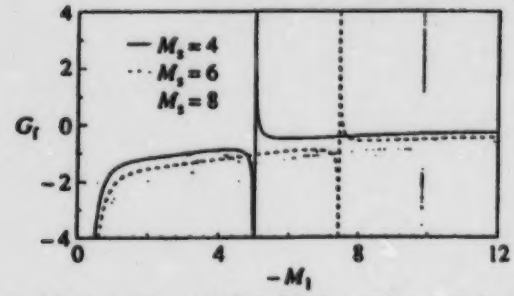

Figure 14. Variation of function G_f with flow Mach number ahead of shock front $M_1 < 0$.

manipulating (B 1)–(B 4) with the shock relations and equation of state (18), we obtain the relations which describe the change of the shock Mach number, the friction and the flow ahead of the shock, i.e.

$$\left.\begin{aligned} \mathrm{d}M_s &= G_f\,\mathrm{d}M_1 \\ \frac{2c_{f1}}{D_{h1}}\mathrm{d}x &= \frac{1-M_1^2}{\gamma E M_1^2|M_1|}\mathrm{d}M_1 \end{aligned}\right\} \tag{B 5}$$

where

$$G_f = \frac{\dfrac{M_1}{E}+\tfrac{1}{2}(\gamma-1)\dfrac{M_1M_2}{E}-\dfrac{M_2}{F}-\dfrac{M_1^2-1}{\gamma EM_1}-\dfrac{D_{h1}c_{f2}}{D_{h2}c_{f1}}\dfrac{1-M_1^2}{\gamma EM_1^2|M_1|}\dfrac{M_2|M_2|[1-(\gamma-1)M_2]}{M_2+1}}{\dfrac{2M_s}{(\gamma+1)F}\left(1+\dfrac{1}{M_s^2}\right)+\dfrac{4M_s}{2\gamma M_s^2-(\gamma-1)}} \tag{B 6}$$

The expressions for E and F can be found in Appendix A.

The property of the flow Mach number M_2 is the same as described in Appendix A. The behaviour of the function G_f varying with M_1 and M_s are displayed in figure 14 for the case of M_1 in the negative x-direction (i.e. opposite to that of M_s). $G_f < 0$ holds up to the point where $M_2 \to -1$, at which the flow chokes immediately behind the shock front owing to the influence of the friction, which stands on the last term in the numerator of the function G_f. Knowing the behaviour of the function G_f, from (B 5) one can obtain the rules for the interaction of the friction with the shock front ahead of which flow is opposed. Where $G_f < 0$ we have:

$$\mathrm{d}x > 0 \quad \mathrm{d}M_1 > 0 \quad \mathrm{d}M_s < 0 \quad \text{for} \quad |M_1| < 1 \tag{B 7}$$

and

$$\mathrm{d}x > 0 \quad \mathrm{d}M_1 < 0 \quad \mathrm{d}M_s > 0 \quad \text{for} \quad |M_1| > 1. \tag{B 8}$$

The rules (B 7) and (B 8) indicate the different effect of friction on a shock front when the flow velocity ahead of the front is changed; that is, the shock wave is attenuated in a frictional duct with opposed subsonic flow, and amplified as opposed flow ahead of the shock front is supersonic.

References

Atamanchuk, T. & Sislian, J. 1991 Hypersonic detonation wave powered lifting-propulsive bodies. In *AIAA 3rd Int. Aero. Planes Conf., Orlando, Florida.*

Behrens, M., Struth, W. & Wecken, F. 1965 Studies of hypervelocity firings into mixtures of hydrogen with air or with oxygen. In *Proc. 10th Symp. (Int.) Combust.*, pp. 245–252. Pittsburgh: The Combustion Institute.

Chester, W. 1960 The propagation of shock waves along ducts. *Adv. appl. Math.* 6, 119–152.

Dunlap, R., Brehm, R. L. & Nicholls, J. A. 1958 A preliminary study of the application of steady state detonative combustion to a reaction engine. *Jet Propulsion* 28, 451–456.

Fickett, W. & Wood, W. W. 1966 Flow calculations for pulsating one-dimensional detonations. *Phys. Fluids* 9, 903–916.

Han, Z. & Yin, X. 1993 *Shock dynamics*. Netherlands: Kluwer Academic Publishers. (In the press.)

Hertzberg, A., Bruckner, A. P. & Bogdanoff, D. W. 1988 Ram accelerator: a new chemical method for accelerating projectiles to ultrahigh velocities. *AIAA Jl* 26, 195–203.

Lee, J. H., Zhang, F. & Chue, R. S. 1992 Some fundamental problems of detonation instabilities and its relation to engine operation. In *2nd ICASE/NASA LaRC Meeting on Combustion, Newport News, VA, 12–14 October*. See also Buckmaster, J., Jackson, T. L. & Kumar, A. (eds) *Combustion in high-speed flows*, pp. 541–574. The Netherlands: Kluwer Academic Publishers.

Liepmann, H. W. & Roshko, A. 1957 In *Elements of gasdynamics*, pp. 84–120. New York: John Wiley & Sons Inc.

Morrison, R. B. 1978 *Evaluation of the oblique detonation wave ramjet*. NASA CR-145358.

Ostrander, M. J., Hyde, J. C., Young, M. F., Kinsinger, R. D. & Pratt, D. T. 1987 Standing oblique detonation wave engine performance. *AIAA Paper* no. 87–2002.

Sargent, W. H. & Gross, R. A. 1960 Detonation wave hypersonic ramjet. *ARS Jl* 30, 543–549.

Thibault, P. A., Penrose, J. D., Sulmistras, A., Murray, S. B. & Labbe, J. L. D. S. 1992 Studies on detonation driven hollow projectiles. In *2nd ICASE/NASA LaRC Meeting on Combustion, Newport News, VA, 12–14 October*. See also Buckmaster, J., Jackson, T. L. & Kumar, A. (eds) *Combustion in high-speed flows*, pp. 421–443. The Netherlands: Kluwer Academic Publishers.

White, F. M., 1974 In *Viscous fluid flow*, pp. 28–36. New York: McGraw-Hill.

Whitham, G. B. 1958 On the propagation of shock waves through regions of nonuniform area or flow. *J. Fluid Mech.* 4, 337.

Zeldovich, T. B., Borisov, A. A., Gelfand, B. E., Frolov, S. M. & Maikov, A. E. 1988 Nonideal detonation waves in rough tubes. In *Dynamics of explosion* (ed. A. L. Kuhl, J.-C. Leyer & A. A. Borisov) (*Prog. Astronaut. Aeronaut.* 144), pp. 211–231.

Zhang, F. & Lee, J. H. S. 1994 Friction-induced oscillatory behaviour of one-dimensional detonations. *Proc. R. Soc. Lond.* A 446, 87–105.

Zhang, F., Frost, D. L., Chue, R. S., Lee, J. H. S., Thibault, P. & Yee, C. 1993 Stability studies of detonation driven projectiles. In *19th Int. Symp. Shock Waves, Marseille* (ed. R. Brun). Heidelberg: Springer. (In the press.)

Received 15 April 1994; accepted 16 June 1994

NUMERICAL MODELLING OF DETONATION DRIVEN HOLLOW PROJECTILES

P.A. Thibault, F. Zhang, J. Penrose and A. Sulmistras
Combustion Dynamics Ltd.
203, 132 4th Avenue, S.E.
Medicine Hat, Alberta, Canada, T1A 8B5

Abstract

Purpose: To review the main physical processes and modelling approaches for a detonation driven projectile (DDP) propagating in a pre-mixed fuel-air mixture. The influence of key design parameters on the detonation stabilization is illustrated through 2-D and variable area 1-D calculations.

Methods: The simulations are based on the Euler equations, with a one-step combustion model, and source terms to account for the acceleration of the projectile. Additional source terms are incorporated in the 1-D calculations to account for the rate of area change and the momentum losses resulting from wall friction. The 2-D calculations are performed using the Lax-Wendroff and FCT schemes, whereas the 1-D algorithm is based on a second order (PLM) Godunov scheme.

Results: The 2-D calculations demonstrate the important role of the projectile geometry and initial velocity in the establishment of a stabilized detonation wave in the nozzle. The higher resolution 1-D calculations explore the stability of the detonation front which is found to increase with a decrease in the rate of area change, and with the addition of friction in the nozzle.

1. Introduction:

The concept of a detonation driven engine (DDE) was initially introduced by Sargent and Gross [1] and investigated by Morrison [2], Ostrander et al. [3] and Atamanchuk and Sislian [4]. Propulsion in such an engine relies on the formation of a stable detonation to produce thrust. The major advantage of this approach is that the chemical reaction is shock initiated and occurs over a relatively short distance compared to that in a conventional SCRAM engine where combustion is limited by turbulent mixing. As illustrated in Figure 1, the main elements of a DDE include an inlet section where the fuel is injected and mixed with the air, and a nozzle section where the detonation is initiated and stabilized. A detonation driven projectile (DDP), on the other hand, is a simplified DDE which is propelled in a pre-mixed fuel-air mixture. The DDP is a useful research vehicle that allows fundamental studies on the propulsion aspects of a DDE, and eliminates the added complexities associated with fuel injection and mixing.

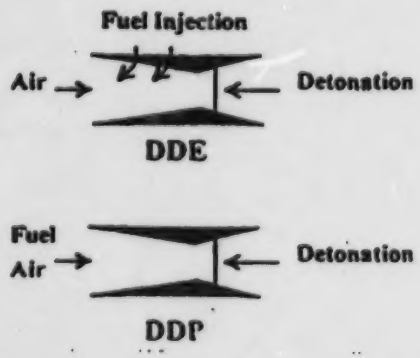

Figure 1: DDE and DDP Geometries

The DDP proposed and investigated by Thibault et al. [5] and Zhang et al. [6,7] is essentially an unconfined and hollow version of the ram accelerator developed by Hertzberg et al. at the University of Washington [8]. This paper reviews some of its underlying physical processes and relevant CFD modelling considerations

2. Governing Equations and Solution Methods

All the calculations presented in this paper solve the Euler equations for 2-D axi-symmetric or 1-D variable area flows.

2.1 2-D Governing Equations

Using a frame of reference attached to the accelerating projectile, the mass, momentum and energy balance equations for 2-D axi-symmetric flow may be written as follows:

$$\frac{\partial \rho}{\partial t} + \frac{\partial \rho v_x}{\partial x} + \frac{1}{r}\frac{\partial \rho v_r r}{\partial r} = 0 \qquad (1)$$

$$\frac{\partial \rho v_x}{\partial t} + \frac{\partial \rho v_x^2}{\partial x} + \frac{1}{r}\frac{\partial \rho v_x v_r r}{\partial r} = -\frac{\partial p}{\partial x} - \rho a_p \qquad (2)$$

$$\frac{\partial \rho v_r}{\partial t} + \frac{\partial \rho v_x v_r}{\partial x} + \frac{1}{r}\frac{\partial \rho v_r^2 r}{\partial r} = -\frac{\partial p}{\partial r} \qquad (3)$$

$$\frac{\partial \rho e}{\partial t} + \frac{\partial \rho e v_x}{\partial x} + \frac{1}{r}\frac{\partial \rho e v_r r}{\partial r} = -\left|\frac{\partial p v_x}{\partial x} + \frac{1}{r}\frac{\partial p v_r r}{\partial r}\right| - \rho a_p v_x \qquad (4)$$

where ρ and p are density and pressure, a_p is the projectile acceleration, and v_x and v_r denote the axial and radial flow velocity components relative to the projectile.

The projectile motion is computed by integrating the equation

$$Ma_p = \int p dA_x \qquad (5)$$

where A_x is the projection of the surface area in the axial direction, and M is the projectile mass.

The energy density, e, includes the chemical energy per unit mass, Q, multiplied by a reaction parameter, α, which varies between 0 and 1 for burned and unburned mixtures respectively:

$$e = \frac{p}{(\gamma - 1)\rho} + \frac{1}{2}(v_x^2 + v_r^2) + \alpha Q \qquad (6)$$

The specific heat ratio, γ, varies continuously between the burned and unburned gas values. The set of equations is completed with the ideal gas equation of state:

$$p = \rho RT \qquad (7)$$

and the rate equation for the reactant, α

$$\frac{\partial \rho \alpha}{\partial t} + \frac{\partial \rho \alpha v_x}{\partial x} + \frac{1}{r}\frac{\partial \rho \alpha v_r r}{\partial r} = R_\alpha \qquad (8)$$

where:

$$R_\alpha = -\frac{\rho}{\tau_R} \quad \text{for } T > T_{ig} \text{ and } \alpha > 0$$
$$= 0 \quad \text{for } T < T_{ig} \text{ or } \alpha \le 0 \qquad (9)$$

where T_{ig} is the minimum ignition temperature and τ_R is the chemical reaction time. This very simple reaction model is sufficient to simulate the detonation propagation and stabilization process without introducing gasdynamic and chemical instabilities which would require prohibitively fine resolution to resolve in a 2-D calculation. Such instabilities are considered however in the variable area 1-D calculations described later.

2.2 2-D Solution Method

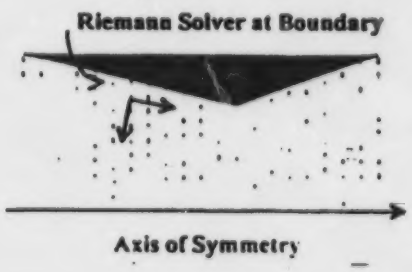

Figure 2: Slanted Boundary on Grid

The above equations are solved using the Lax-Wendroff finite difference scheme in conjunction with the 6th order (phase error) version [9] of the Flux Corrected Transport (FCT) algorithm [10]. As shown in Fig. 2, the solution is computed on a fixed rectangular mesh and uses a special "slanted boundary" algorithm for solid boundaries that are not aligned with the grid. This algorithm maintains free-slip conditions in the direction tangent to the boundary, and solves the Riemann problem for the normal component. The overall solution method uses a "split" algorithm which constructs a 2-D solution through separate sweeps in the x and r directions. The intersection of the slanted boundary with a rectangular grid can introduce computational cells that are significantly smaller than the "standard" cells away from the boundary. This can result in very small time steps due to the explicit nature of the finite difference scheme. As illustrated in Fig. 3, this problem is eliminated by merging the small end cell with the neighbouring cell in the vertical and horizontal sweeps.

The above procedure preserves the simplicity and flexibility of the finite-difference approach. It also avoids the numerical artefacts associated with a "staircase" representation of boundaries not aligned with the grid. It has been extended to 3-D geometries and can accommodate extremely complex geometries without resorting to unstructured grids.

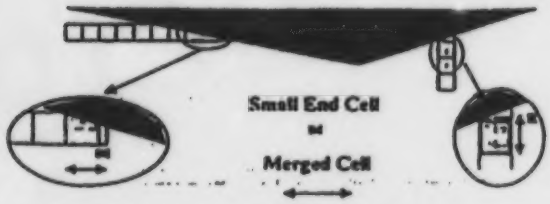

Figure 3: End Cell Merging

2.3. Governing Equations for 1-D Flow

The equations for 1-D variable area flow are similar to the previous 2-D flow description with the following exceptions:

- Source terms are required to account for the variations in cross-sectional area.
- A friction term, f, is included to account for wall friction.
- An Arrhenius reaction model is included to account for potential chemical-gasdynamic instabilities. Also, since the chemical energy is not included directly in the definition of the internal energy, e, a heat release term, $\dot{q}$, is explicitly added to the energy balance equation.
- A drag term is included in the projectile motion equation to account for effects that cannot be directly modelled using a variable area 1-D description. These include the pressure rise behind the oblique shock at the inlet, and the Prandtl-Meyer expansion at the throat.

The above description leads to the following formulation,

$$\frac{\partial \rho}{\partial t} + \frac{\partial \rho v_x}{\partial x} = -\frac{1}{A}\frac{dA}{dx}\rho v_x \tag{10}$$

$$\frac{\partial \rho v_x}{\partial t} + \frac{\partial \rho v_x^2}{\partial x} = -\frac{\partial p}{\partial x} - \frac{1}{A}\frac{dA}{dx}\rho v_x^2 + f - \rho a_p \tag{11}$$

$$\frac{\partial \rho e}{\partial t} + \frac{\partial \rho e v_x}{\partial x} = -\frac{\partial p v_x}{\partial x} - \frac{1}{A}\frac{dA}{dx}v_x(\rho e + p) - \rho a_p v_x + \dot{q} \tag{12}$$

$$\frac{\partial \rho \alpha}{\partial t} + \frac{\partial \rho \alpha v_x}{\partial x} = \frac{1}{A}\frac{dA}{dx}\rho \alpha v_x - k\rho\alpha e^{-\frac{A}{RT}} \tag{13}$$

where

$$e = \frac{p}{(\gamma - 1)\rho} + \frac{v_x^2}{2} \tag{14}$$

$$\dot{q} = Qk\rho\alpha e^{-\frac{A}{RT}} \tag{15}$$

and k and E denote the pre-exponential coefficient and activation energy in the Arrhenius model.

The friction force acting on the gas is given by the expression

$$f = -\frac{2c_f}{D_h}\rho v_s|v_s| \qquad (16$$

where D_h is the hydraulic diameter and c_f is the Fanning friction coefficient and assumed to obey:

$$c_f = \frac{0.3164}{Re^{0.25}} \qquad (17$$

where Re is the Reynolds number

$$Re = \frac{\rho D_h|v_s|}{\mu} \qquad (18$$

and μ is the dynamic viscosity.

The projectile motion is solved by integrating the equation

$$Ma_p = \int_L^{x_{sh}} p dA_s + \frac{\pi^{\frac{1}{2}} D_h}{2} \int_L^0 A^{\frac{1}{2}} f dx + D_w \qquad (19$$

where L is the length of the projectile, x_{sh} is the detonation front position, and D_w is the wave drag associated with the oblique shock and the Prandtl-Meyer expansion at the throat.

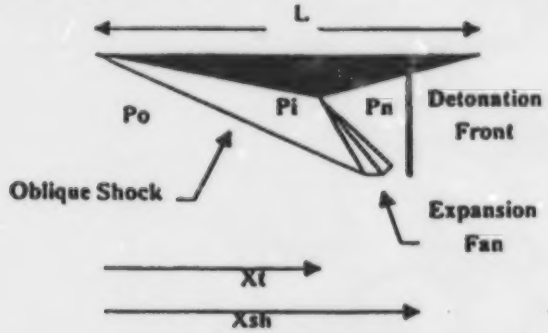

Figure 4: Drag Calculation

As illustrated in Fig. 4, D_w is calculated as:

$$D_w = (p_i - p_n)(A_w - A_t) \quad for \quad x_{sh} > L$$

$$D_w = p_i(A_w - A_t) - p_n[A(x_{sh}) - A_t]: \quad x_t < x_{sh} \le L$$

$$D_w = p_i[A_w - A(x_{sh})] \quad for \quad 0 < x_{sh} < x_t \qquad (20)$$

2.4 Solution Method for 1-D calculation

The above equations for the variable area 1-D flow are solved using the second order (PLM) Godunov method by Van Leer [11] in conjunction with Roe's [12] approximate Riemann solver and operator splitting for the source terms.

3. Computational Results

3.1 2-D Calculations for Fully Coupled Case

Two dimensional calculations were performed for the case of a hollow projectile propelled in a stoichiometric acetylene-air mixture at a pressure of 1 atm and temperature of 298.15K. The projectile has a length L = 254 mm, an outer diameter d= 203 mm, with d_i/d = 0.75 and x_t/L = 0.6. The initial Mach number of the projectile is equal to 6 which is slightly larger than the Chapman Jouguet value M_{CJ} = 5.4 for this mixture.

The calculations were performed with a resolution of 2.5 mm per computational cell which corresponds to 40 cells per projectile radius. The reaction time, τ_R, was chosen to accommodate approximately 3 computational cells for the reaction zone. Higher resolution calculations with larger reaction zones have also been performed and are described in [5]. The main computational grid was surrounded by a geometrically expanding grid that contained 25 additional cells in both the axial and radial directions. The expansion ratio for each cell in this portion of the grid is equal to 1.3 and results in a grid extension of 76 projectile radii.

The pressure and temperature contours in Fig. 5 display the four main phases of the projectile acceleration process. The first frame shows the ignition process which is caused by the implosion of the conical bow shock emanating from the leading edge of the projectile. During this phase, the projectile has not yet felt the thrust force from

the detonation and is decelerating due to the net drag The ignition process is followed by the formation of a detonation front which consists of three separate branches. The central branch is overdriven and follows the trajectory outlined by the conical bow shock. The outer branch, which propagates along the nozzle wall is responsible for producing the thrust. At the time of the second frame, the thrust equals the drag to produce a zero acceleration. These two detonation fronts, connected by a third "bridge" detonation, propagate up the nozzle to a maximum penetration distance where the projectile acceleration is maximum (third frame). Further acceleration of the projectile then causes the detonations to be pushed back to a steady state position where the projectile Mach number reaches a maximum steady state value M_p = 6 43 which is 19% larger than the Chapman Jouguet value for this mixture.

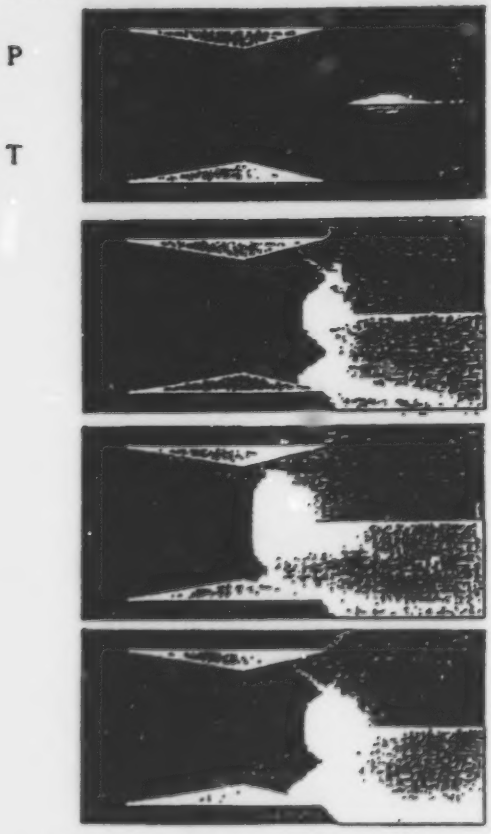

Figure 5: Fully Coupled Calculation

3.2 Effects of Projectile Geometry and Initial Mach Number

The successful stabilization of the detonation front depends greatly on the initial conditions and the projectile geometry. If the initial velocity of the projectile is too low, the detonation front will penetrate through the throat section and "outrun" the projectile thereby resulting in negative thrust (Fig. 6). A similar situation occurs if the projectile throat diameter is too small in which case ignition occurs in the inlet rather than in the nozzle section (Fig. 7).

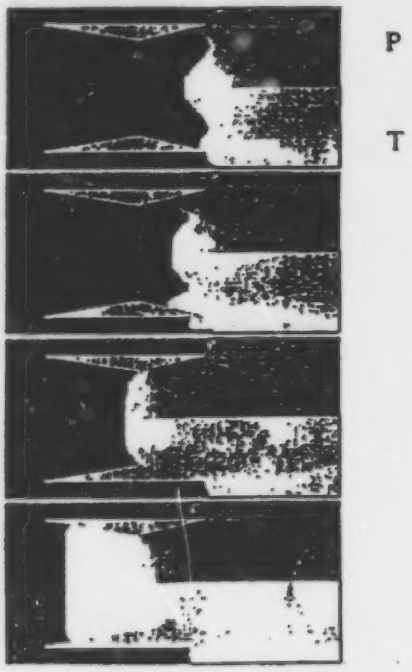

Figure 6: Effect of Initial Velocity

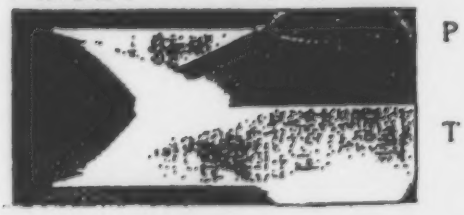

Figure 7: Effect of Geometry

3.3 1-D Stability Calculations

The 2-D calculations demonstrate the feasibility of maintaining a detonation front in the nozzle of the projectile to maintain positive thrust. They also clearly reveal the important role of geometry and start-up velocity in the design of a Detonation Driven Engine (DDE).

One important aspect which was not explored in the 2-D analysis is the sensitivity of the detonation front to local perturbations. For most fuel-air mixtures, such perturbations result in the formation of instabilities at the detonation front. This is due to the large sensitivity of the reaction rate to the local changes in temperature behind the shock front. The instabilities usually manifest themselves in the form of a transverse wave structure with dimensions 1 to 2 orders of magnitude larger than the local reaction zone. Unfortunately, the mesh resolution required to resolve such instabilities in a multi-dimensional analysis would be prohibitive for DDP geometries and fuel-air mixtures of interest. For this reason, the 2-D calculations were based on a constant reaction time combustion model which would not trigger instabilities and could be solved with moderate resolution and CPU requirements.

In the case of 1-D simulations, sufficient resolution is available to explore the susceptibility of different projectile geometries to the onset of longitudinal oscillations. These studies which are discussed in much greater detail in [6,7] were performed using a one step Arrhenius combustion model with a specified activation energy E. For a given combustion energy Q and specific heat ratio γ, a planar detonation in a constant area channel (or tube) is one dimensionally stable for $E < E_s$ where E_s can be calculated using analytical methods or repeated 1-D calculations. The calculations reported here are for the case γ=1.2 and $Q = 50RT_0$ which corresponds to a detonation Mach number M_{cj}=6.2. The activation energy value $E = 22RT_0$ was selected to be significantly below the value $E_s = 25RT_0$ where a planar constant-area detonation becomes unstable.

3.4 Effect of Area Change

As in the case of the 2-D analysis, the 1-D calculations indicate that a detonation may be stabilized in the nozzle with an appropriate choice of projectile geometry and initial velocity. Figure 8 shows the time histories for the shock and projectile Mach numbers for a projectile with $x_i/L = 0.6$, $d/L = 0.84$, $d_t/d = 0.7$, and an initial Mach number of 5.8. After an initial overshoot of the detonation front Mach number, the projectile and detonation velocities stabilize with only minor oscillations to reach a final Mach number of approximately 6 which is approximately 3% lower than the Chapman Jouguet value of 6.2 for the mixture.

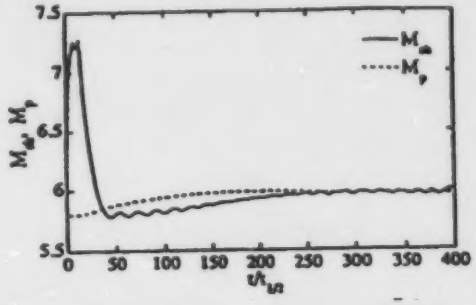

Figure 8: $d_t/d = 0.7$, $M_p(0) = 5.8$

The above calculations were repeated with the same initial conditions and geometry but with a smaller throat diameter $d_t/d = 0.6$. This results in a larger area expansion rate dA/dx which produces stronger oscillations in the detonation front velocity (Fig. 9). The final steady state projectile Mach number is also reduced to a value of 5.8 which corresponds to a 6% deficit from the Chapman Jouguet velocity.

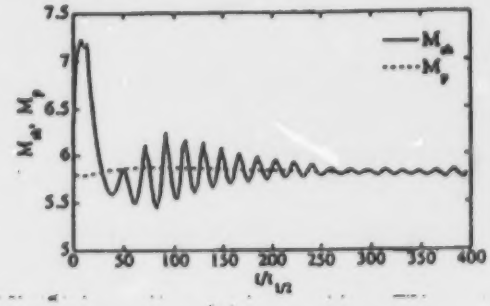

Figure 9: $d_t/d = 0.6$, $M_p(0) = 5.8$

As seen from Fig. 10, the oscillations described above become far more pronounced if the initial projectile velocity is reduced from 5.8 to 5.4. The velocity excursions, in this case, are sufficiently large to expel the detonation from the nozzle, and decouple it from the projectile.

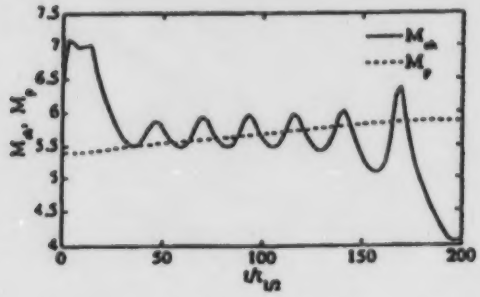

Figure 10: $d_t/d = 0.6$, $M_p(0) = 5.4$

3.5 Effect of Wall Friction

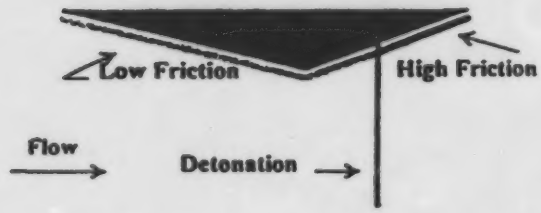

Figure 11: Wall Friction Behind Detonation

The introduction of wall friction in the 1-D flow analysis can have a strong effect on the detonation stability and the final projectile velocity depending on the variation of the friction factor along the projectile wall. From an intuitive point of view, one would expect friction to act as a retarding force that decelerates the projectile. This is certainly true for the flow in the unburned gas upstream of the detonation front. Behind the detonation front, however, the friction force acting on the burned gas acts in the direction of the detonation propagation. This force acts to increase the detonation velocity, and pressure, thereby increasing the thrust. Significant performance enhancement can therefore be achieved by increasing the wall roughness behind (or downstream) of the detonation wave. This fact is illustrated in Figure 11 where the friction factor , c_f, is increased by a factor of 40 across the detonation front. In this case, the projectile attains a final Mach number of 6.4 which is 3% larger than the Chapman Jouguet velocity for the mixture, and 8% larger than that for the case of no friction. The increase in detonation velocity also acts to raise the post-shock temperature and decrease the oscillation amplitude.

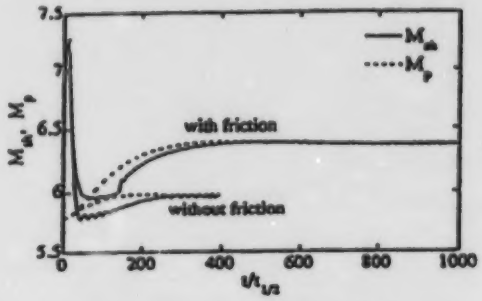

Figure 12: Effect of Wall Friction

4. General Discussion and Conclusions

The above calculations have highlighted some of the key features governing the performance of detonation drive projectiles (DDP).

The 2-D calculations based on the Euler equations and a constant combustion time model suggest the following:

- Stable detonation propulsion may be achieved by selecting an appropriate projectile geometry and initial velocity.
- For a given projectile shape, the successful start-up of the projectile (or engine) requires a minimum initial projectile velocity.
- The overdriven detonation front produced in the nozzle results in a final projectile velocity that is larger than the Chapman Jouguet velocity for the mixture.

The variable area 1-D calculations based on a single step Arrhenius model supports the above conclusions with the following exception and additions:

- The final projectile velocity is slightly below the C.J. velocity unless a large increase in wall friction is introduced in the burned gas behind the detonation front.

- The stability of the detonation front decreases with the activation energy and the rate of area increase in the nozzle section, but can be increased by adding friction in the burned gas behind the detonation front.

From a general modelling point of view, it is clear that the following considerations will play an important role in future CFD simulations on this problem:

- Viscous and turbulent flow inside the projectile should be investigated in terms of their role in determining the optimal projectile geometry.

- The aerodynamic stability of the projectile should be investigated through appropriate 3-D calculations.

In addition to these, considerable attention should be paid to the modelling of the detonation front and its cellular structure. Two approaches can be used for this purpose depending on the characteristic length scale of the projectile, L, and the detonation cell size, λ.

- In the case where L and λ are of the same order of magnitude, detonation failure may occur in the projectile. High resolution 3-D calculations with adaptive gridding, and a good global chemical kinetic model may be required to evaluate a particular geometry.

- If $L >> \lambda$, an efficient computational approach would be to use a detonation tracker in conjunction with a detonation "sub grid" model to monitor the local detonation structure.

5. References

1. Sargent, W.H. and Gross, R.A. "Detonation wave hypersonic ramjet". *ARS Journal* (1960).
2. Morrison, R.B. "Evaluation of the oblique detonation wave ramjet". Universal Systems Inc., *NASA CR NAS1-14771*, (1978).
3. Ostrander, M.J., Hyde, J.C., Young, M.F., Kissinger, R.D. and Pratt, D.T. "Standing oblique detonation wave engine performance". Aerojet TechSystems Co., PRA-SA-AFAL, published by the American Institute of Aeronautics and Astronautics Inc. (1987).
4. Atamanchuk, T. and Sislian, J. "Hypersonic detonation wave powered lifting-propulsive bodies". *AIAA Third International Aerospace Planes Conference*, Orlando, Florida. (1991).
5. Thibault, P.A. Penrose, J.D., Sulmistras, A., Murray, S.B. and Labbe, J.L.D.S. "Studies on detonation driven hollow projectiles" 2nd ICASE/NASA LaRC Meeting on Combustion, Newport News, VA, Oct. 12-14, (1992), Kluwer Academic Publishers (In Press).
6. Zhang, F., Frost, D.L., Chue, R.S., Lee, J.H.S., Thibault, P. and Yee, C. "Stability Studies on detonation driven projectiles" 19th Int. Symp. Shock Waves, Marseille, France (1993).
7. Zhang, F., Thibault, P., Yee., C., Chue, R.S., Frost, and Lee J.H.S. "One dimensional stability analysis of detonation-driven projectiles" to be presented at the 30th AIAA/ASME/SAE/ASEE Joint Propulsion Conference, June 27-29, Indianapolis, IN, USA, AIAA 94-3223
8. Hertzberg, A., Bruckner, A.P., and Bogdonoff, D.W. "Ram accelerator: a new chemical method for accelerating projectiles to ultrahigh velocities". AIAA Journal 26 (2). 195-203. 1988
9. Book, D.L. and Fry, M.A. "Airblast simulations using flux corrected transport codes". Naval Research Laboratory Memorandum 5334, (1984).
10. Boris, J.P. "Flux corrected transport modules for solving generalized continuity equations". Naval Research Laboratory Memorandum 3237, (1976).
11. Van Leer, B. "Toward the ultimate conservative difference scheme V. A second-order sequel to Godunov's method". *J. Comp. Phys.*, 32:101-136, (1979).
12. Roe, P.L. "Approximate Riemann solvers, parameter vectors and difference schemes". *J. Comp. Phys.* 43:357-372, (1981).

SOLUTION OF 2-D AND 3-D FULLY COUPLED FSI PROBLEMS FOR COMPRESSIBLE FLOWS

Link, R., Tran, D., Chen, L., Thibault, P. A.
Combustion Dynamics Ltd.
132 - 4th Avenue S.E.
Medicine Hat, Alberta, Canada, T1A-8B5

Norwood, M.
Martec Ltd.
Suite 400, 1888 Brunswick St.
Halifax, Nova Scotia, Canada, B3J-3J8

Slater, J.
Defence Research Establishment Suffield (DRES)
P.O. Box 4000
Medicine Hat, Alberta, Canada, T1A-8K6

Abstract

Purpose: To develop methods to model 2-D and 3-D fluid-structure interaction problems
Methods: An explicit Lax-Wendroff FCT Eulerian finite difference formulation is used to compute the fluid motion. A Lagrangian finite element formulation is used to calculate the solid response; explicit time integration is used for 2-D, and implicit integration is adopted for 3-D. Riemann solvers are used to compute the variables at the fluid-solid interface, and insure free slip conditions there. The coupled formulations are valid for arbitrarily large deformations in the 2-D case, and small deformations in the 3-D case. The proposed formulations are used to analyse three problems; the first a classical 1-D wave transmission problem analysed using 2-D, the second a 2-D simulation of blow-out panels in air, and the third a 3-D analysis of a typical ship hull submerged in water.
Results: Comparison of 1-D transmitted pressures with exact results is excellent for the 1-D wave transmission problem. Qualitative results for the 2-D blow-out panel simulation seem to be in agreement with expected behaviour, and demonstrate the stability of the algorithm for extremely large solid deformations. Pressure and velocity plots obtained for the 3-D ship hull analysis show cavitation and pressure regions consistent with expected and observed results.
Conclusions: Two Lagrangian-Eulerian techniques are presented here to solve fluid-structure interaction problems. Calculations performed on the three problems described above yielded good quantitative agreement for the 1-D wave transmission case, and good qualitative agreement for the 2-D and 3-D cases. Comparison with experimental results is required for full method validation.

Introduction

Fluid structure interaction (FSI) problems in compressible fluid flow represent a large category of problems including aerodynamics, underwater shock analysis, and pressure vessel safety evaluation for volatile goods.

Traditional methods of computational analysis include modeling the structure as an immovable object, or using a computational solid mechanics (CSM) code to represent both the fluid and the solid. The former does not take into consideration the deformation of the structure, which may result in overly conservative, or non-conservative results, depending on whether or not cavitation is involved. The latter attributes solid properties to the fluid mass, which is not realistic. What is required is a combined solution technique, where both the fluid and solid are realistically characterized.

This paper presents solution techniques and numerical calculations for three problems involving 2-D and 3-D fluid-structure interaction problems. The fluid and gas flow are modeled using a Lax-Wendroff/FCT algorithm on a fixed Eulerian grid. The solid behaviour is characterized using a Lagrangian finite element formulation. The two models are connected using a mixed Lagarangian-Eulerian formulation.

The selected problems are drawn from theoretical and industrial applications. The first problem is a 1-D verification problem consisting of simple wave transmission. The second problem is a 2-D qualitative evaluation of a sequence of blow-out

panels in air. The third problem involves a 3-D qualitative analysis of a thin ship hull subjected to an underwater shock.

Methods

CFD Calculation

The calculations presented in this paper assume the flow to be inviscid and compressible. The Euler equations for mass, momentum, and energy are solved over a fixed Cartesian grid using an explicit Lax-Wendroff finite difference scheme [1]. This integration scheme is used in conjunction with the 6th order (phase error) version [2] of the Flux Corrected Transport (FCT) scheme [3]. The solution is constructed using a "split" approach that uses separate sweeps in the x and y directions. Free-slip conditions are maintained tangent to the solid-fluid/gas interface by solving a Riemann problem normal to the interface (discussed later).

Two materials are considered here: air, and water. The air energy and state equations are assumed to follow classical ideal gas laws. The water state equation is assumed to follow the Tait equation of state for densities greater than ambient, and the modified Tait equation of state for densities less than ambient [4]. In this model, note that since the pressure for water is solely a function of the density through the above mentioned state equations, an energy equation is not required for the medium.

Solid Calculation

The finite element method is used in solid calculations due to the ease with which non-regular geometries are handled. The formulation is based on the well known variational statement of virtual work [5]. A Lagrangian frame of reference, where the mesh moves with the material, is preferred here for two reasons. Firstly, the relative strains in the solid material are small, so no accuracy loss due to distorted elements is expected. Secondly, the alternative would be to use an Eulerian frame of reference, which would not work well with small strains, since resolution would be lost in material advection and front tracking. All material is assumed to follow a linear elastic constitutive law i.e. material stress is proportional to material strain.

Two different time integration schemes are used in the solid computations. In the 2-D calculations, an explicit central difference scheme is adopted which is identical to that used by Hallquist in the explicit solid hydrocode DYNA-3D [6]. For 3-D calculations, only structures constructed of thin plates are considered here. In this case, the through-thickness wave transmission characteristics are neglected i.e. waves are transmitted through bending and axial motion. An implicit Newmark scheme [5] is utilized, and no viscous damping is assumed.

Riemann Solver Calculation

A Riemann solver is used here to calculate the boundary conditions at the fluid-solid interface. Its advantage lies in the ease with which it accommodates slanted boundaries. Free-slip conditions are guaranteed, which eliminates the problem of "staircasing", prevalent in earlier CFD codes. In addition, the Riemann solver is implicit and exact, thereby ensuring stability and accuracy of the solution.

Two types of Riemann solvers are utilized in this study:

1) Fluid-deformable solid - 2-D
2) Fluid-rigid solid - 3-D

The different solvers can best be described by examination of Figure 1. For case 1, given the fluid pressure, density, and velocity p_F, ρ_F, and v_F, respectively, and given the solid counterparts p_S, ρ_S, and v_S, the interface pressure and velocity p_I and v_I respectively are computed. The state variables for both sides are given in a region near the interface. For case 2, the fluid state variables only are given, along with the interface velocity. The interface is treated as a rigid reflecting boundary with relative velocity $v_F - v_I$. From the interface velocity conditions, the interface pressure and density are calculated.

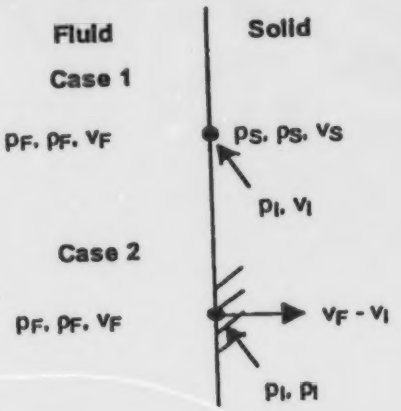

Figure 1 Riemann solver description

Material Tracker Calculation

A first order material tracker is used to update the position of the fluid-solid interface as the solid moves through the Eulerian grid. The interface updating proceeds as follows. Interface velocities are integrated over the time step to obtain the new position. Once the new interface position has been determined, the redistribution of materials is ascertained, and the properties of any changed fluid cells is computed.

Integration of Solid and Fluid Codes

The computational segments described above are combined as shown in Figure 2 (it is assumed here that the shock propagates through the fluid media first, although this is not necessarily the case).

The calculation is started with the assignment of boundary conditions which is performed by the Riemann solver segment. These fluid boundary conditions are then used by the CFD computational segment to solve the Euler equations for fluid densities, velocities, and pressures. At this point, the problem is checked to see whether a deformable solid is present on the Euler grid. If this is the case, the pressures at the solid boundary are sent to the solid computational segment, where the boundary velocities and positions are updated by solving the equations of motion for the solid. The fluid state variables are then used by the material tracker segment to update the solid and fluid material position.

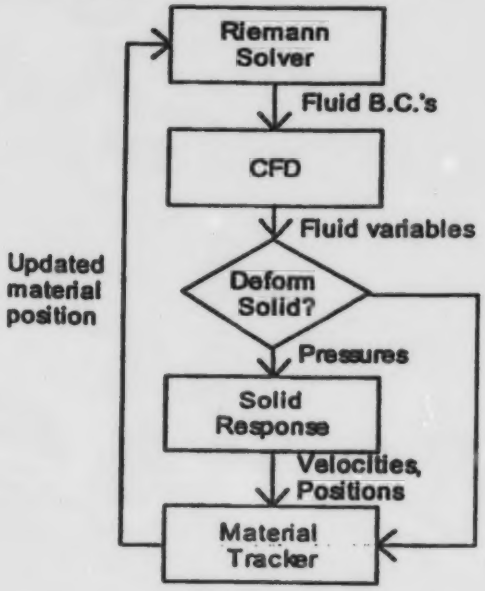

Figure 2 Calculation flowchart

The flowchart shown in Figure 2 applies for both 2-D and 3-D calculations, with one exception for 3-D. For 3-D computations, the deformations are assumed small; therefore, the deformations are neglected. In other words, only velocities are sent to the CFD code.

There is a difference in the integration of the structural response segment between 2-D and 3-D. In the case of 2-D calculations, the coding is contained within the main CFD module, IFSAS (Integrated Fluid Structure Analysis Software). For 3-D calculations, IFSAS is connected with a more sophisticated stand-alone 3-D structural analysis program, VAST (Vibration And STrength analysis). A schematic of the program connection is shown in Figure 3.

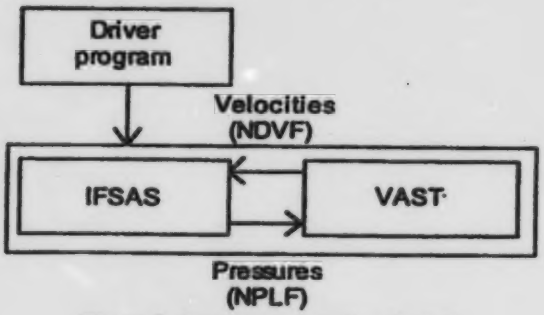

Figure 3 Program connection for 3-D

Because IFSAS and VAST are two independent, stand-alone programs, it was felt that the best way to connect the two would be through the use of disk files. A neutral pressure loading file (NPLF) was used to transfer pressure information from IFSAS to VAST. Conversely, a neutral displacement and velocity file (NDVF) was used to transfer velocity information from VAST to IFSAS. A driver program written in UNIX script was used to facilitate communication between the two programs.

The calculation is begun by starting IFSAS, which performs the Riemann solver and CFD calculations. Calculated pressures are written to the NPLF. The program VAST is then started, and performs the solid response calculation. Velocity information is then written to the NDVF. The looping continues until the analysis end time is reached.

Results

1-D Results

The 1-D calculation involved the application of a simple flat shock on a 2-D grid composed of various fluids and solids. Figure 4 shows the

computational model used. The geometry adopted was Cartesian. The shock was applied by use of an inflow condition as shown in Figure 4. Sides 1 and 3 allowed no flow through normal to the boundary in the fluid, and allowed horizontal translation only in the solid. Side 2 was fixed against any translation in the solid.

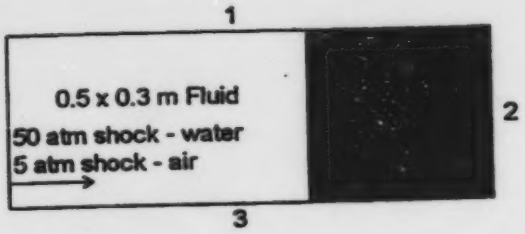

Figure 4 1-D calculation setup

There were three analysis cases considered here, and are defined as follows:

Case 1: Water - mud
Case 2: Water - steel
Case 3: Air - steel

Typical initial state values were used for both air and water. State values for the solids were as follows:

Mud: Elastic modulus = 8×10^9 Pa
Density = 2000 kg/m^3
Steel: Elastic modulus = 2×10^{11} Pa
Density = 7850 kg/m^3

As indicated in Figure 4, an inflow shock condition of 50 atm absolute pressure was applied for cases involving water (1 and 2), and 5 atm for the case involving air (3).

The fluid pressures are compared with the exact results of the solution of the 1-D wave transmission problem in Table 1. It is evident that analysis results are similar to those obtained from exact theory.

Case No.	Analytical	Exact
1	72.6	72.6
2	96.1	95.9
3	17.9	17.7

Table 1: Comparison of pressures (in atm)

2-D Results

The 2-D analysis was performed on a double compartment with movable pressure hatches. The concept was to simulate a blow-out situation in a typical pressure vessel.

Figure 5 shows the setup used in the calculation. The 25x100 CFD computational grid is assumed as axisymmetric about the y-axis. The structural finite element model consists of 4 node quadrilateral elements whose sizes are identical to that of the CFD cells.

The double compartment is composed of steel. The bottom of the structure is restrained in the vertical direction, and the axis of symmetry is restrained in the horizontal direction. The top and bottom hatches are composed of steel and aluminum, respectively, and are located as shown in Figure 5. The hatches are free to translate vertically, and are not connected to the steel compartments.

The top compartment and the compartment outsides contain ambient air. An expansion of the combustion in the bottom chamber was used to induce loading on the structure. This was performed by using an Arrhenius one step burn model with a low ignition temperature and short reaction time.

Figure 6 shows the position of the pressure hatches at various times. Positions 1-4 denote analysis times of 4.4, 8.4, 15.2, and 19.2 milliseconds, respectively. At position 1, blow-out of the aluminum hatch is well under way, and large gas velocities are expected at the hatch periphery. Figure 7 is a velocity vector plot at position 1, with every second grid point plotted. It is evident that particle velocities are relatively large in this region, with a maximum of 2284 m/sec.

At position 3, it is seen that both the aluminum and steel hatches are in motion. This is due to a localized pressure increase obtained from piston action. The pressure increase then causes motion in the steel hatch. This is clearly evident by examination of the plot in Figure 8, which shows pressure contours at 14.0 milliseconds.

At position 4, the aluminum hatch has reversed motion. This is due to the mass difference between the aluminum and steel hatches. The aluminum hatch has approximately 6 times less mass than the steel hatch. The magnitude of the pressure increase is sufficient to reverse the motion of the aluminum hatch.

Qualitative results seem to be in agreement with what is expected. Comparison with actual experimental results is required for full verification of the numerical model.

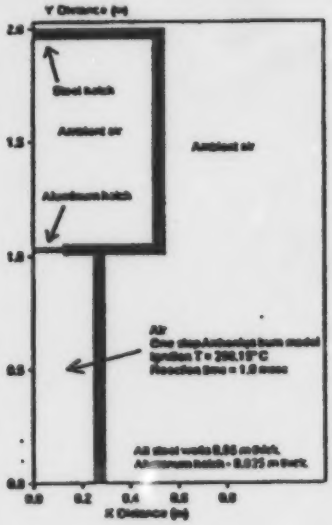

Figure 5 2-D calculation setup

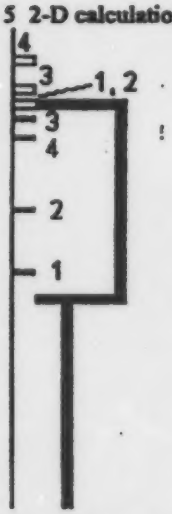

Figure 6 Hatch motion at various times

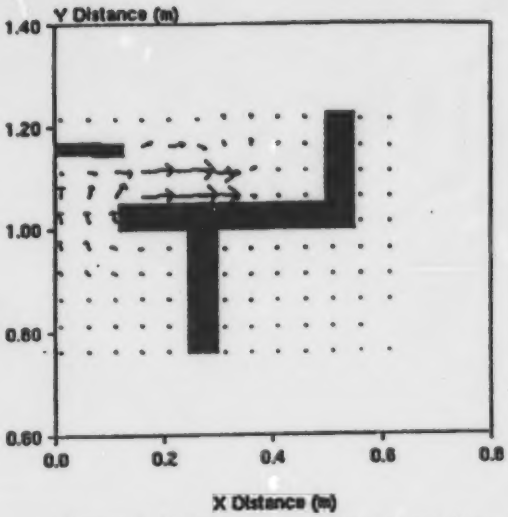

Figure 7 Velocity vector plot at t = 4.4 msec

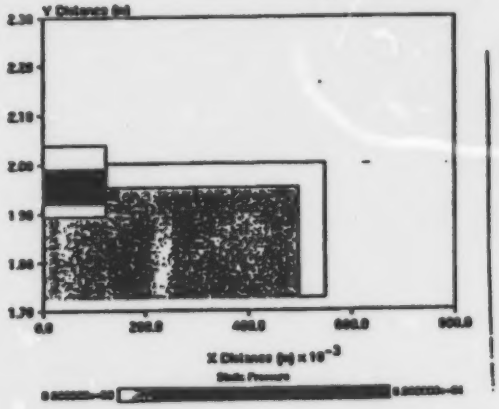

Figure 8 Pressure contours at t = 14.0 msec

3-D Results

The 3-D analysis was performed on a model of a ship hull subjected to a typical far-field blast scenario. Figure 9 shows the overall numerical model. The following assumptions were made:

1) The explosive charge is far away from the ship i.e. the charge distance is large in comparison with the ship cross-sectional dimensions.

2) The explosive charge detonates when the ship midship is perpendicular to a line drawn from the charge to the midship.

3) The ship bulkheads (stiffening plates transverse to the hull span) are more or less uniformly spaced.

4) Overall rigid body ship motions are small.

Given these assumptions, an acceptable estimate of fluid-structure interaction can be obtained by the use of a considerably simplified 3-D model. A typical section between bulkheads was taken as the representative structure because of the relatively flat shock implied by assumptions 1 and 2, and the repetitive structural response implied by assumption 3.

A charge size of 6800 kg of TNT was used. This explosive charge was assumed to be acting at horizontal and vertical distances of 300 m and 95 m respectively from the hull middeck (point A in Figure 9). These large distances preclude the use of a point detonation model for the TNT charge, because of resolution loss and limited computational resources. In order to obtain increased computational resolution in the ship hull region, a 30x30x10 m CFD computational volume consisting of 48x48x16 cells was adopted. The explosive charge was simulated by using inflow boundary conditions consistent with the charge size and distance [7]. The inflow conditions impose a flat shock moving at an angle parallel to the distance vector from the charge to the bottom corner of the computational grid.

Figure 10 shows the setup of the CFD computational grid. The ship hull wetted surface is composed of 40 shell elements, and no calculations are performed on the region inside the hull. The computational portion includes a decaying pressure inflow condition at a trajectory of 13 degrees (maximum strength of 24.7 atm), a flow through grid to avoid spurious shocks, and a water-air interface at the top surface for investigation of bulk cavitation. A pressure monitoring point is placed 2.0 under the water surface, and 1.0 m away from the ship hull. The effects of hydrostatic pressure are not considered here.

Figure 11 shows the setup of the structural finite element mesh. The mesh is composed of a complex array of beam and shell elements taken from a typical ship section. The grey area represents the wetted surface that is included in the CFD analysis

Figure 12 is a pressure contour plot located halfway through the z-direction (z = 5 m) at 14 msec. Bulk cavitation is evident, and is due to the rarefaction wave reflected at the air-water interface. In addition, wall cavitation exists at the bottom of the ship hull, and a pressure ridge is evident on the side of the ship hull. These phenomena are explained subsequently.

Figure 13 is a velocity vector plot at the same position and time. Near the region of wall cavitation, there are large inward velocities, which are consistent with a hull cavitation region. At the pressure ridge location, there are large outward velocities, consistent with formation of a pressure ridge.

Figure 14 shows the deflected shape of the ship hull at 14 msec (magnified at 250 times). The region of wall cavitation is deflected inwards, and the pressure ridge location is deflected outwards. From this plot, it appears that the deformation at the wall cavitation section bends the pressure ridge area through a combination of bending and arching action. The deformation patterns seem consistent with the pressure distributions.

Figure 15 is a pressure time history plot at the monitoring point in Figure 10. There are three distinct pressure spikes. The first spike is caused by the initial shock wave impacting the point. The third spike is caused by the upward deformation of the hull bottom, which causes the hull by the monitoring point to bulge outward. The second spike may have been due to impact near the slanted surface between the vertical section and hull bottom.

Similar to results obtained from the 2-D analysis, qualitatively the 3-D model displays behaviour consistent with expected and observed field behaviour. Quantitative results would involve analysis of simpler structures, and comparison with experimental and/or theoretical results.

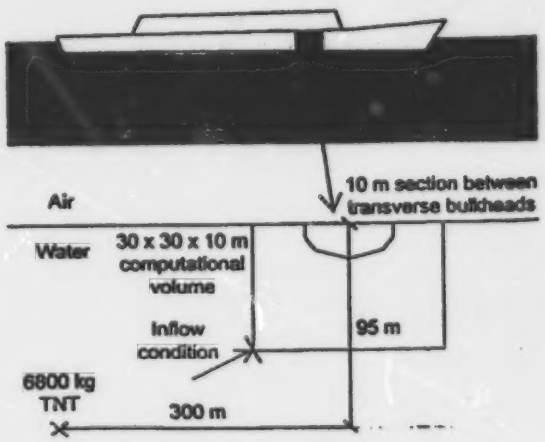

Figure 9 Numerical model

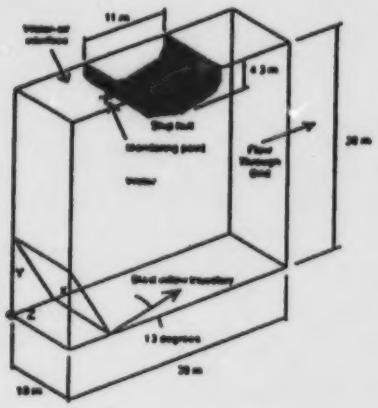

Figure 10 CFD setup

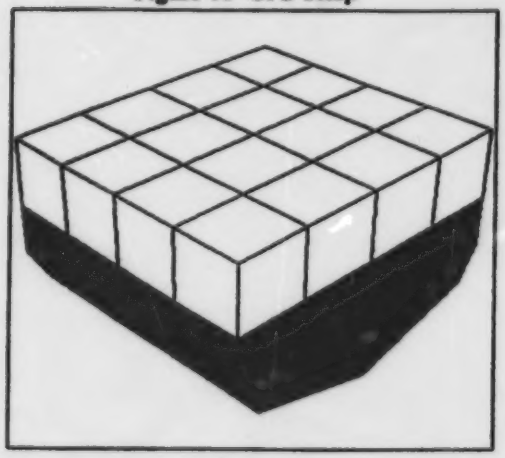

Figure 11 Structural setup

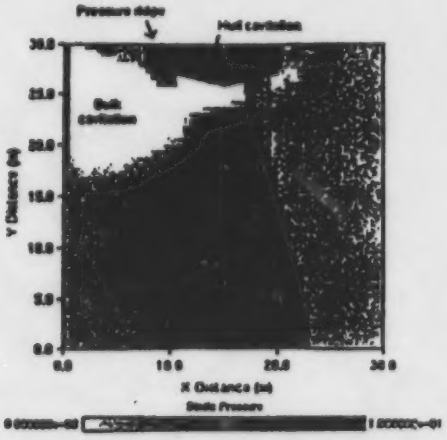

Figure 12 Pressure contours at 14.0 msec

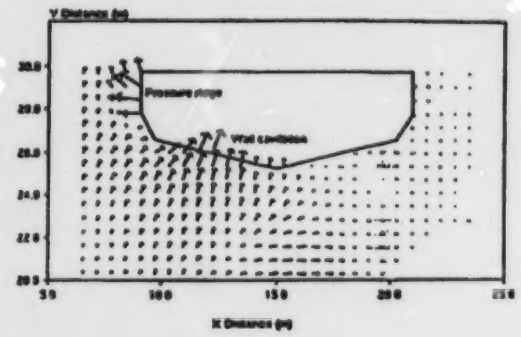

Figure 13 Velocity vectors at 14.0 msec

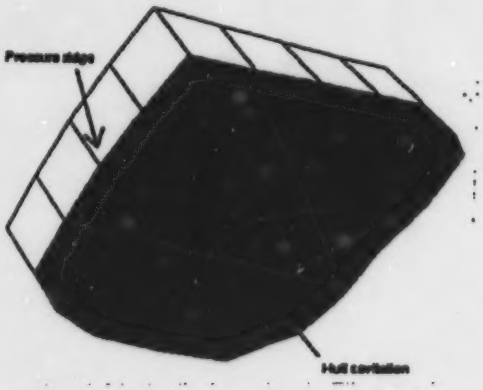

Figure 14 Deflected shape at 14.0 msec

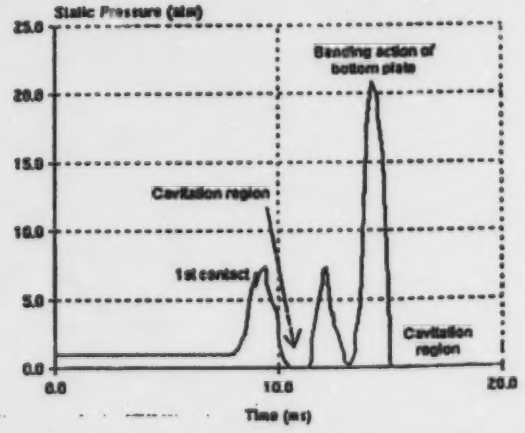

Figure 15 Pressure history at monitoring point

Summary and Conclusions

This paper has presented two coupled Lagrangian-Eulerian techniques to solve fluid-structure interaction problems. The first technique applies to 2-D problems of arbitrary solid deformation, and the second technique involves 3-D thin shell problems with small deformations. The main components of these schemes include

1) An explicit Eulerian finite difference Lax-Wendroff/FCT scheme that computes fluid response.

2) An exact Riemann solver for the fluid-structure interface.

3) A material front tracker that monitors the solid position, and maps it onto the Eulerian grid.

4) An explicit Lagrangian finite element technique for computation of the 2-D solid response. An implicit Lagrangian finite element solver for 3-D solid computations.

5) A technique for integration of independent, sophisticated fluid and structural computational segments for 3-D calculations.

Calculations were performed on three test problems. The first problem was a verification test involving the 1-D wave transmission problem. Analytical results obtained from this test compared well with the results obtained from exact theory. The second problem consisted of a simulated 2-D blow-out scenario in a double compartment, and qualitative results seemed to agree with what was expected. In addition, it was seen that the computations remained stable through extremely large rigid body motions. The third problem involved a 3-D analysis of a typical ship hull subjected to a far-field blast. Examination of the results revealed cavitation and high pressure regions consistent with expected behaviour.

Further improvements to broaden the application spectrum, and increase accuracy include the following:

1) Enhancements on fluid and solid front tracking techniques. By combining the material interface tracker with available shock tracking techniques, accuracy of shock resolution in fluids can be improved considerably. In solids, the artificial viscosity scheme is used to maintain wave physics. This could be improved by possibly adopting an FCT scheme.

2) Multiple time scales on 2-D solid calculations. The solid usually requires a significantly smaller time step than the fluid. If this time step is used in the fluid, overly diffusive fluid behaviour may result.

3) Enhancements on material models. Effects such as plasticity, and fracture/failure models are important in practical shock fluid-structure interaction problems

4) The capability to model thin solids less than 1 fluid cell thickness, and incorporation of arbitrarily large solid deformations in 3-D is required.

5) Experimental validation. Correlation with data from carefully controlled simple tests is necessary to fully validate the techniques presented here.

References

[1] Thibault, P.A., Zhang, F., Penrose, J., and Sulmistras, A. (1994). Numerical modeling of detonation driven hollow projectiles. Second Annual Conference of the CFD Society of Canada, University of Toronto, Toronto.

[2] Book, D.L., and Fry, M.A. (1984). Airblast simulations using flux corrected transport codes. Naval Research Laboratory Memorandum 5334.

[3] Boris, J.P. (1976). Flux corrected transport modules for solving generalized continuity equations. Naval Research Laboratory Memorandum 3237.

[4] Hains, F.D. (1982). Fluid-structure interaction by the method of characteristics. 53rd Symposium on Shock and Vibration, Part 2: Fluid-Structure Dynamics and Dynamic Analysis, Danver, Mass., USA, pp 26-28.

[5] Bathe, K.J. (1982). Finite element procedures in engineering analysis. Prentice-Hall, 735 p.

[6] Hallquist, J.O. (1983). Theoretical manual for DYNA-3D. Report UCID 19401, Lawrence Livermore Laboratories.

[7] Keil, A.H. (1966) . The response of ships to underwater explosions. Annual Meeting of the Society of Naval Architects and Marine Engineers, New York, New York, pp. 366-410.

Report of an Invention:

DETONATION DRIVEN PROJECTILE

1. The Problem

Conventional aircraft power plants, including turbojets and turbofans, can be designed to operate at flight speeds near Mach 2. Speeds of approximately Mach 6 are possible using ramjet technology. The flow entering a ramjet is supersonic, but it is made to pass through a shock wave so that combustion of the fuel-air mixture takes place at subsonic conditions. In a ramjet engine, significant time is available for mixing to take place between the fuel and air. Flame holders are required to stabilize the combustion zone.

In order to attain higher flight speeds, it becomes necessary for combustion of the fuel-air mixture to take place supersonically. Development of the so-called supersonic combustion ramjet, or SCRAMJET, has been the subject of intense study within the propulsion community for quite some time. Although it has been reported that scientists conducting research in support of the National Aerospace Plane (NASP) have tested prototype engines up to Mach 8 in a land-based test cell, the details of this work are still highly gaurded. In general terms, supersonic combustion requires that fuel be introduced to air entering the engine, and that the resulting mixture be instantaneously shock heated to a temperature in excess of the ignition temperature. Subsequent rapid combustion leads to a stabilized and coupled shock and combustion zone, or "standing detonation wave," at some point downstream of the fuel injectors. The success of such an engine hinges on the ability to stabilize the detonation front over the operational range of flight speeds.

2. How May it be Accomplished According to Present Knowledge

Hypersonic propulsion made possible by a stabilized detonation front has apparently been demonstrated in a device known as the "Ram Accelerator" (References 1-4). This apparatus is essentially a ramjet-in-tube concept for accelerating projectiles to hypervelocities. The concept was first proposed by Hertzberg and co-workers at the University of Washington during the mid 1980's. As shown in Figure 1, the projectile resembles the centrebody of a conventional ramjet and is accelerated by the release of

combustion energy in a stationary tube filled with a reactive gas mixture. The tube acts as the outer cowling of the ramjet and the energy release process moves along with the projectile. There is no fuel carried aboard the projectile. It is apparent from Figure 1 that the SCRAMJET engine and the Ram Accelerator are based on identical physics; only the frame of reference is different.

In Hertzberg's apparatus, an annular passage is maintained between the projectile's outer surface and the tube wall by a series of four fins on the aft section of the projectile. An alternative approach, and the one adopted by the research group at Institute Saint-Louis in France (Reference 5), is to employ an axisymmetric projectile (without fins) in a tube equipped with several internal and equally spaced longitudinal rails. In either case, the "inlet" of the engine could appropriately be defined as that portion of the apparatus between the projectile nose and maximum projectile diameter. Correspondingly, that segment between the maximum diameter and the tail of the projectile could be aptly termed the engine "nozzle."

Two general modes of combustion have been proposed by Hertzberg and colleagues. In the case of the "thermally choked subsonic mode" (Figure 1), the projectile is injected into the tube by either a powder or light gas gun at a velocity well below the theoretical or Chapman-Jouguet (C-J) detonation velocity of the combustible mixture. The nose angle of the projectile and the sensitivity of the combustible mixture are chosen so that neither the oblique shock system, nor the normal shock wave located further downstream, are strong enough to ignite the mixture. The zone of combustion is established behind the projectile using an external ignitor. Choking of the flow by the heat release stabilizes the normal shock on the projectile body. This mode of combustion results in ballistically efficient acceleration up to velocities of 2.7 - 3.0 kilometers per second.

In order to achieve efficient acceleration to higher velocities, an alternative mode of combustion must be induced. Figure 2 shows the "superdetonative ram acceleration mode." In this mode, the projectile velocity must exceed the detonation velocity of the combustible mixture. Transition from the thermally choked mode to the superdetonative mode can be induced by abruptly changing the gas mixture entering the inlet. In practice, a thin diaphragm is generally used to separate two gas mixtures in the tube. If the second gas has a detonation velocity lower than the projectile velocity, transition to the superdetonative mode takes place automatically. Care must be taken to tailor the nose angle, projectile velocity and sonic velocity of the gas mixture so that combustion does not occur behind the initial oblique shock, but rather behind the first or subsequent reflected shocks. This ensures that the high-pressure detonation products act on the aft surface of the projectile.

Experimental data from a test involving a 70 gram projectile accelerating in a relatively short four-compartment tube containing various gases are presented in Figure

3. The projectile's maximum diameter and the tube diameter are 28.9 mm and 38 mm, respectively. A final velocity near 2.5 kilometers per second is apparent, corresponding to a Mach number in excess of 8 for the gas mixture contained in the final compartment of the tube. In theory, velocities on the order of 12 kilometers per second are thought to be possible based on this mode of combustion. However, aerodynamic heating and ablation become problematic above 6 kilometers per second.

Two important points should be noted about the experiments conducted by the groups at the University of Washington and the Institute Saint-Louis. First, the combustion processes rely on the presence of the tube wall. In the absence of the wall there would be no reflected shock waves and hence no standing detonation wave available for the production of thrust. Secondly, the gas mixtures employed in these experiments are at elevated pressures (16 - 31 atmospheres). Thus, it is not clear whether this arrangement would function at atmospheric pressure.

A variant of the Ram Accelerator, studied recently at the Technion-Israel Institute of Technology, is the so-called "External Propulsion Accelerator" shown in Figure 4 (Reference 6). In this apparatus, the tube diameter is much larger (about 4 times) than the projectile diameter. The flow over the projectile is established independently of any interactions with the tube wall. As with Hertzberg's experiments, a gun is used to inject the projectile into a pressurized combustible gas mixture at high supersonic speeds. The projectile velocity and geometry, as well as the sensitivity of the combustible mixture, are tailored so that the oblique shock wave formed at the projectile nose compresses the gas significantly but does not ignite it. Subsequently, a detonation wave is generated on the projectile centrebody by some aerodynamic means such as a blunt step or notch. The intersection between the oblique shock wave and detonation wave occurs well away from the tube walls. The high-pressure, high-temperature products of detonation are then expanded over the rear of the projectile in order to produce thrust.

Since the external propulsion flow structure is independent of reflections from the tube walls, the investigators argue that this configuration should be operational over a much larger range of velocities than is possible with the Ram Accelerator. Their analysis shows that a higher thrust might also be possible. One serious problem with the analysis is that it is one-dimensional in nature, whereas the real problem is axisymmetric. Therefore, the calculated performance is likely overpredicted and may not

even be valid. No testing of this configuration has been done to date.

3. Limitations or Drawbacks of the Present Apparatus

The Ram Accelerator configuration, although successful at achieving hypersonic projectile velocities, cannot lead to a self-contained, free-flying power plant because the tube walls are instrumental in the generation of thrust. Additionally, a confined tube permits the use of a high-pressure fuel/oxidizer mixture. It is not clear whether this propulsion mechanism would be successful at atmospheric pressure.

The External Propulsion Accelerator has the advantage of not needing the tube walls in order to establish a shock/detonation complex capable of generating thrust. Thus, a free-flying power plant is theoretically possible. The present inventors, however, are skeptical about the advertized propulsive performance of this design. Another disadvantage of this design is that it presents a large cross sectional area to the oncoming flow. This will result in very significant levels of aerodynamic drag. Finally, it is difficult to imagine how on-board fuel (in the case of a fully operational engine) would be introduced effectively into combustion zones external to the vehicle.

4. Our Proposal

Our proposal is to use a tubular projectile for achieving internal combustion and efficient hypersonic flight. A sketch showing one simple configuration appears in Figure 5. Basically, it consists of a hollow cylinder 400 mm long by 200 mm in diameter (these dimensions have been chosen to enable the projectile to be fired from a 8-inch naval gun). The internal contour of the projectile is machined so that a minimum diameter or "throat" exists at some distance from the leading edge of the projectile. The region forward of the throat functions as the engine inlet, while that aft of the throat constitutes the nozzle. The design in Figure 5 has a 150-mm diameter throat located 150 mm from the leading edge. These dimensions have been selected so that the shock wave which establishes at the engine inlet is of the correct angle and strength to cause ignition of the fuel-air mixture and the subsequent establishment of a standing detonation wave in the vicinity of the throat.

The results of numerical calculations (contours of overtemperature ratio) showing the "start-up" phenomena for this design are presented in Figure 6. The flow entering the engine has been modelled to closely represent stoichiometric acetylene-air at atmospheric pressure. This mixture is characterized by a C-J detonation Mach number

of about 5.3. The calculations have been carried out for a flight speed of Mach 6.0 so that supersonic combustion takes place. It should be emphasized that these calculations model the equation of state and the conservation equations quite accurately. The only simplifying assumptions are those related to the rate of chemical reaction (a 3-parameter, 1-step burn model is employed in place of full chemical kinetics). Viscous effects are also ignored.

A description of the phenomena in Figure 6 is given below. It should be noted that each computer generated graphic shows only one half of the flow field (i.e., the horizontal axis represents the centreline of the hollow projectile). One should also note that the vertical axis has been expanded for visual clarity. The staircase-like contours are an artifact of the graphics routines and not the calculations. The projectile body is shown in black. The oncoming flow approaches from the left in all cases.

In 6a, an oblique shock wave begins to form at the leading edge of the projectile. The shock-heated gas, shown in pink, is at an elevated temperature but is still well below the ignition temperature of the combustible mixture. Eventually, the conical shock wave converges on the projectle axis (6c), and gives rise to a hot spot (dark pink region in 6d). Recall that Hertzberg relies on shock reflection from a wall to generate a hot spot. Shortly after the appearance of this hot spot, ignition of the gas takes place, leading to a detonation bubble which expands rapidly to fill the entire cross section of the projectile (6e - 6h). Subsequently, the wave is seen to march forward toward the throat in 6i through 6l. At the same time, it adjusts to the boundary conditions dictated by the projectile wall and the axis of symmetry. The final set of graphics (6m - 6p) shows the wave migrating almost to the throat and finally stabilizing at a position just rearward of that location. To the authors' knowledge, these are the first time-accurate combustion calculations showing the establishment of a standing detonation front in a hypersonic flow.

The calculations displayed in Figure 6 show only the engine starting process. Once the detonation front establishes, the projectile will accelerate as a result of thrust generation. Figure 7 shows plots of acceleration and velocity as a function of time for a steel projectile fired from a gun into a bag containing acetylene-air mixture. An artist's conception of such an experiment is shown in Figure 8. When the projectile first emerges from the gun into ambient air, it decelerates under the influence of aerodynamic drag forces. The engine starts up about 13 ms later as the projectile enters the combustible mixture in the bag. Acceleration then occurs until the projectile achieves a terminal velocity of about 2.29 kilometers per second (Mach 6.62). The range of the projectile at this point is about 200 meters. The terminal velocity is governed by the balance between thrust and aerodynamic drag forces acting on the projectile. Contour plots similar to those presented in Figure 6 show that the detonation front recedes from the throat somewhat as the terminal velocity is approached. This is a reflection

of the changing inlet conditions with increasing flight speed.

It should be emphasized that the geometry of the projectile discussed above is in no way optimized. Future numerical calculations will focus on optimizing the inlet and nozzle geometries. In particular, the feasibility of incorporating a low-loss Busemann type inlet and a flared nozzle will be investigated.

5. What is Thought to be Novel about Our Proposal

The inventors believe their proposal is novel in the following ways:

- It appears to be the first convincing design for a free-flying detonation-driven projectile.
- It appears to be operational at standard atmospheric pressure, which might not be the case for the ram accelerator or the external propulsion accelerator (all tests and analysis with respect to these latter devices have involved elevated pressures).
- The detonation front is internal to the device in contrast to the external propulsion accelerator. This will have obvious advantages when the management of on-board fuel becomes an issue.
- Its small cross-sectional area means low drag and hence the possibility of achieving higher flight speeds than other proposed devices. Low drag will also mean low specific fuel consumption.

The inventors believe their proposal has tremendous potential for both military and civil applications once on-board fuel is incorporated into the design. Possible applications include:

- Off-route mines
- Standoff demolition devices
- Large calibre armour-piercing rounds
- One-shot high-speed aerial targets
- One-shot disposable engines for the delivery of surviellence devices or weapons

- Air-breathing portion of a single-stage-to-orbit vehicle
- Hybrid detonation driven projectile and spinning tubular projectile (i.e., high thrust performance in early stage of flight followed by high drag performance in latter stage)

6. References

1. Hertzberg, A., Bruckner, A., and Bogdonoff, D.W., "The Ram Acclerator: A New Chemical Method of Achieving Ultrahigh Velocities." Presented at the 37th Meeting of the Aeroballistic Range Association, Quebec, Canada, September 9-12, 1986.
2. Bruckner, A.P., Bogdanoff, D.W., Knowlen, C., and Hertzberg, A., "Investigation of Gasdynamic Phenomena Associated with the Ram Accelerator Concept." AIAA Paper 87-1327, June, 1987.
3. Hertzberg, A., Bruckner, A., and Bogdonoff, D.W., "Ram Acclerator: A New Chemical Method for Accelerating Projectiles to Ultrahigh Velocities." AIAA Journal, Vol. 26, pp. 195-203, 1988.
4. Bruckner, A.P. and Hertzberg, A., "Investigation of Superdetonative Ram Accelerator Drive Modes." Report prepared for the Office of Naval Research, Arlington Virginia, by the Aerospace and Energetics Research Program, University of Washington, December 1989.
5. M. Giraud, J.F. Legendre, G. Simon and L. Catoire, "Ram Accelerator in 90 mm Caliber: First Results Concerning the Scale Effect in Thermally Choked Propulsion Mode." Thirteenth International Symposium on Ballistics, Stockholm, Sweden, 1-3 June 1992.
6. J. Rom and G. Avital, "The External Propulsion Accelerator: Scramjet Thrust Without Interaction of Accelerator Barrel." AIAA/SAE/ASME/ASEE 28th Joint Propulsion Conference, July 6-8 1992, Nashville, TN.

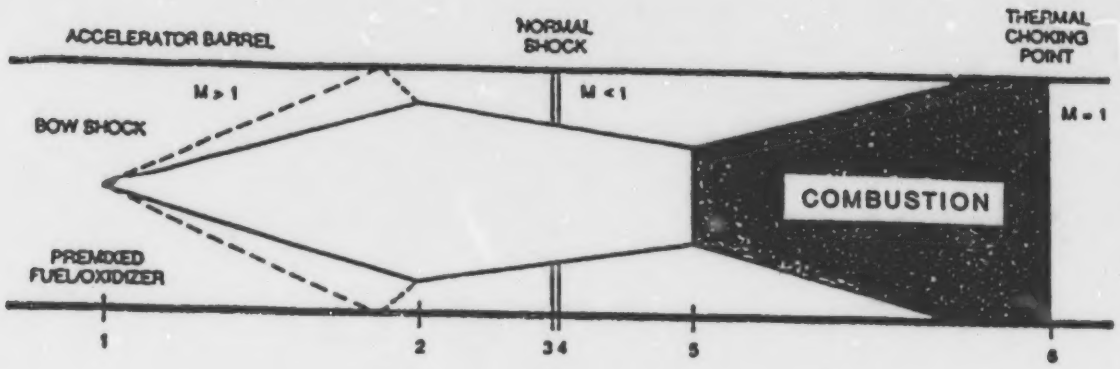

Figure 1
Subsonic Combustion Thermally Choked Ram Accelerator Mode

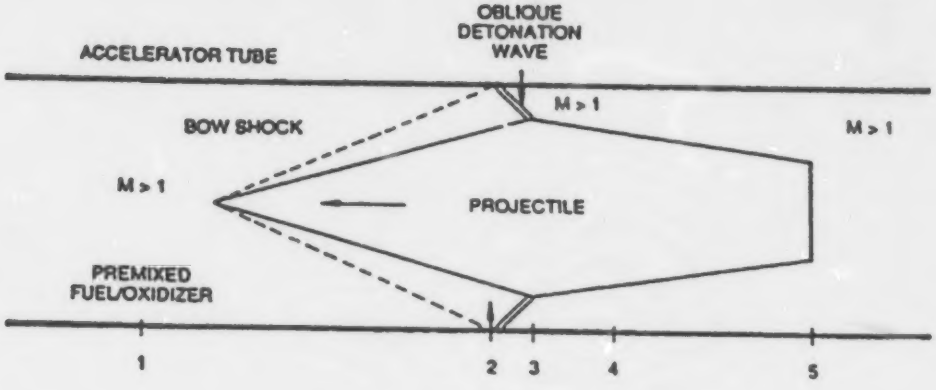

Figure 2
Superdetonative Ram Accelerator Mode

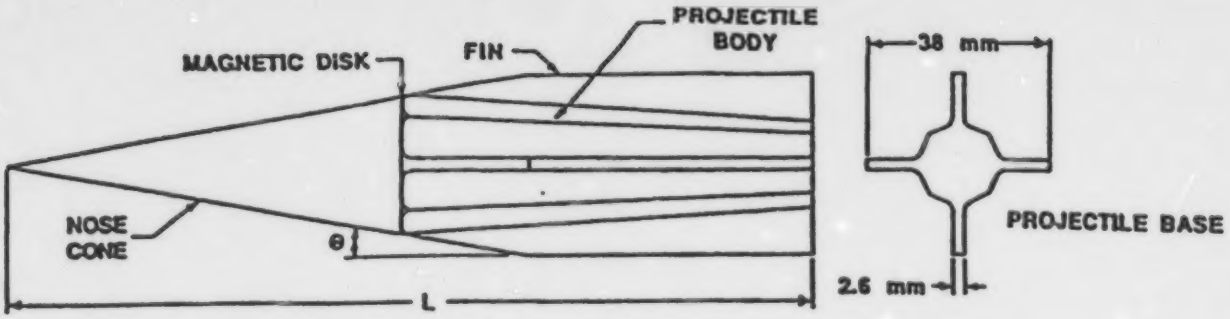

PROJECTILE	TYPE A	TYPE B
L	138 mm	168 mm
θ	12.5°	10°

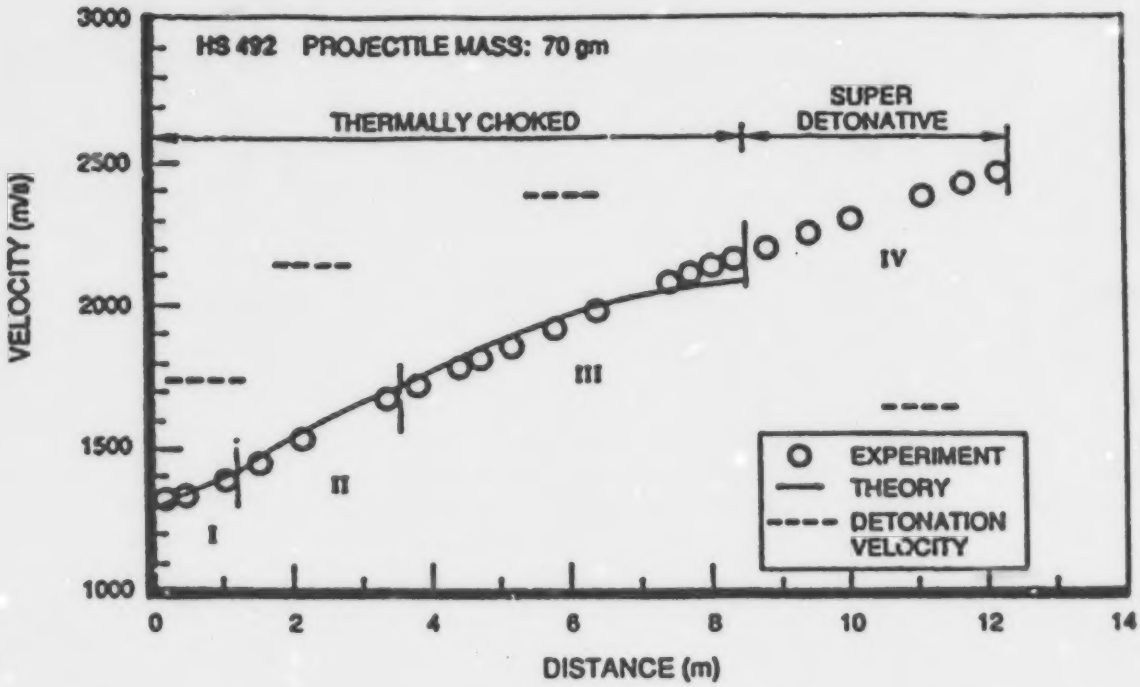

STAGE	MIX	SOUND SPEED	PRESSURE
I	2.6 CH_4 – 2 O_2 – 5.6 N_2	363 (m/s)	31 atm
II	4.5 CH_4 – 2 O_2 – 2 He	448 (m/s)	31 atm
III	3.5 CH_4 – 2 O_2 – 6.5 He	544 (m/s)	31 atm
IV	0.6 C_2H_4 – 2 O_2 – 3.8 CO_2	291 (m/s)	16 atm

Figure 3
Projectile Details and Ram Accelerator Performance

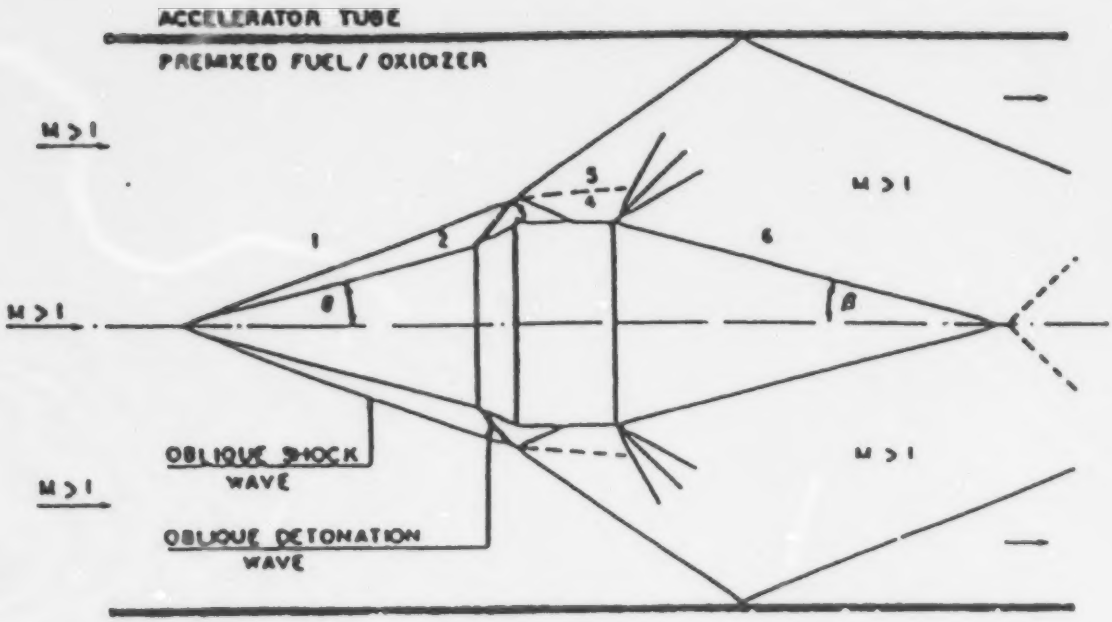

Figure 4
Wave System for the External Propulsion Accelerator

Figure 5

DETONATION DRIVEN PROJECTILE

ACETYLENE-AIR @ P = 1 ATM and T = 298 K
FLIGHT MACH NUMBER = 6.0
MIXTURE DETONATION MACH NUMBER = 5.3

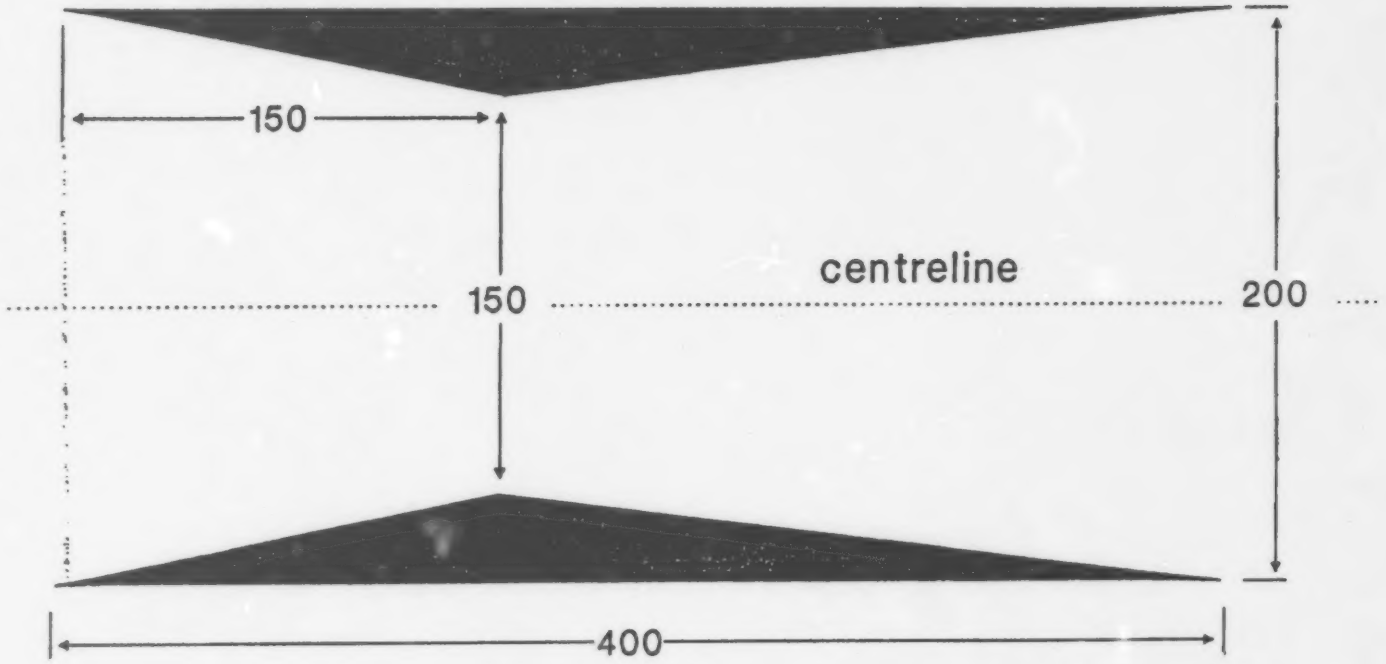

All Dimensions in millimeters

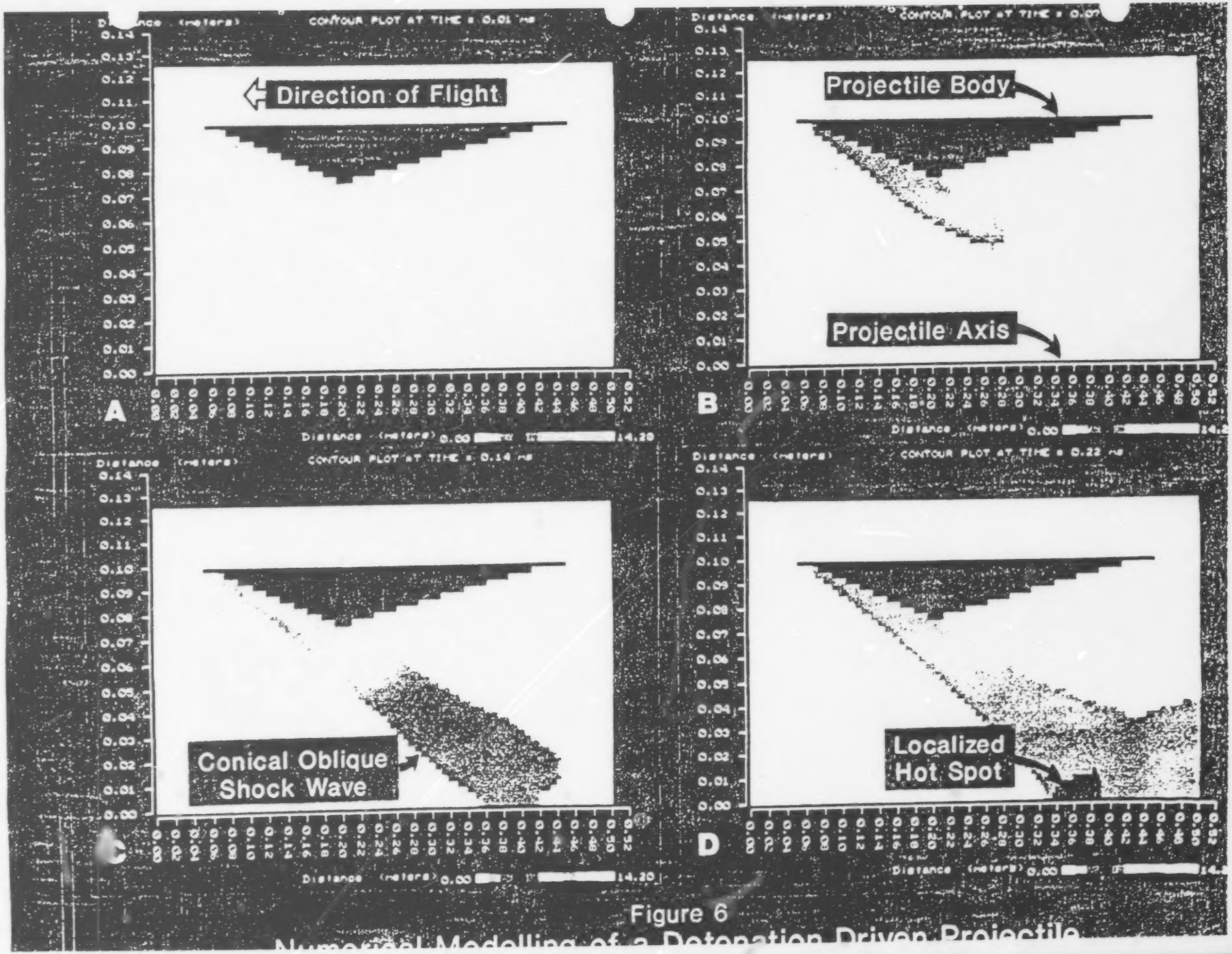

Figure 6

Numerical Modelling of a Detonation Driven Projectile

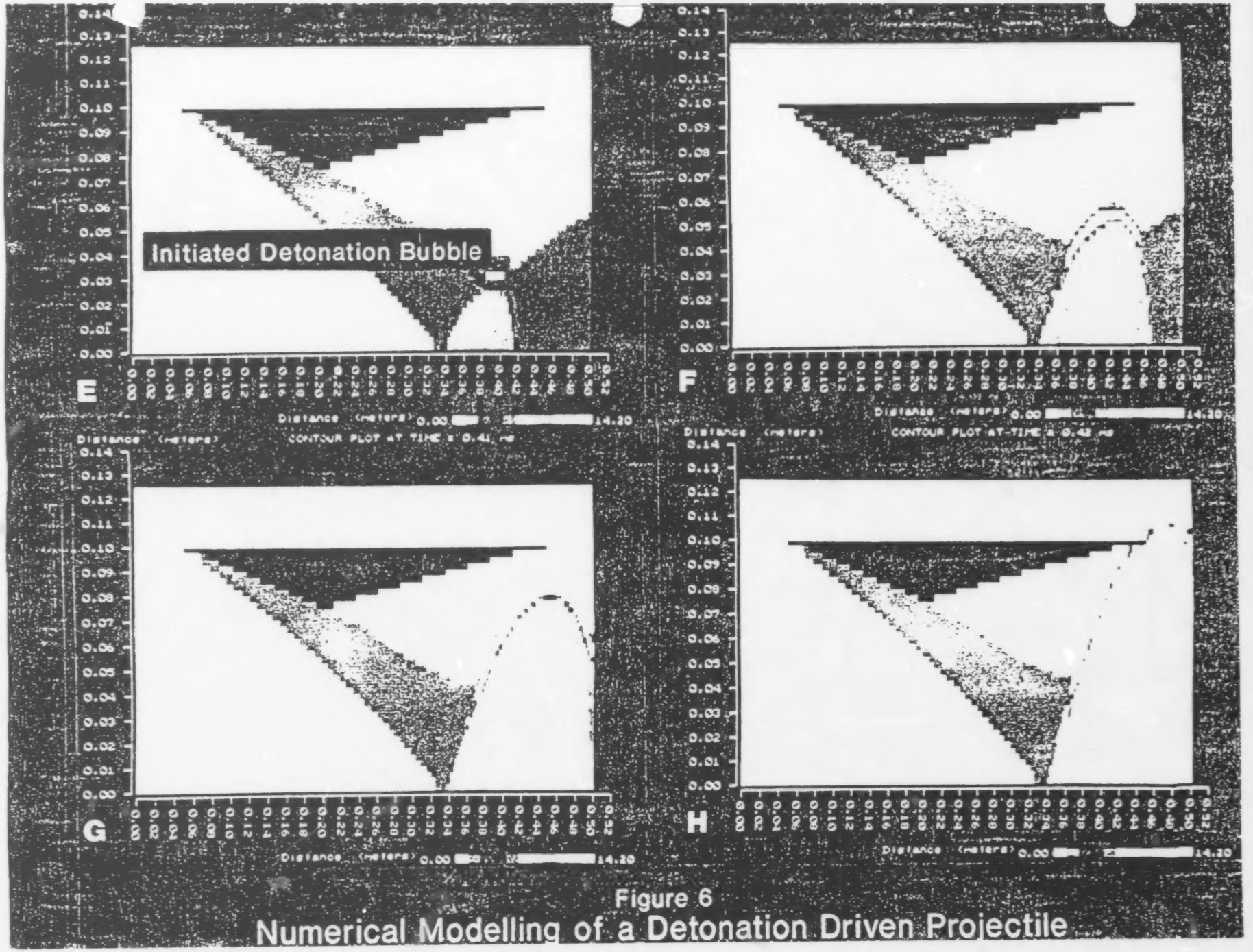

Figure 6

Numerical Modelling of a Detonation Driven Projectile

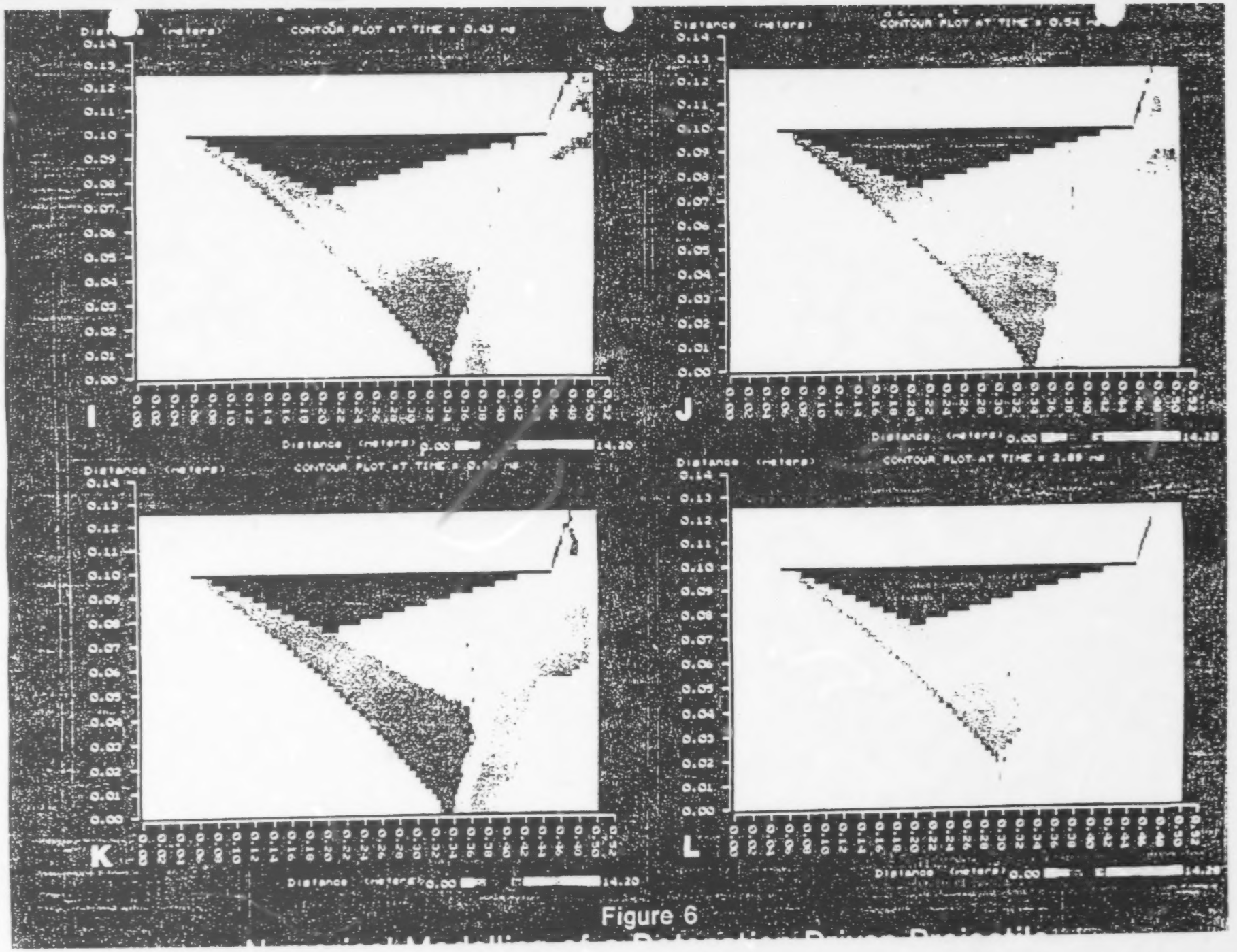
CONTOUR PLOT AT TIME = 0.43 ns
CONTOUR PLOT AT TIME = 0.54 ns
CONTOUR PLOT AT TIME = 2.89 ns
Distance (meters)
I
J
K
L

Figure 6

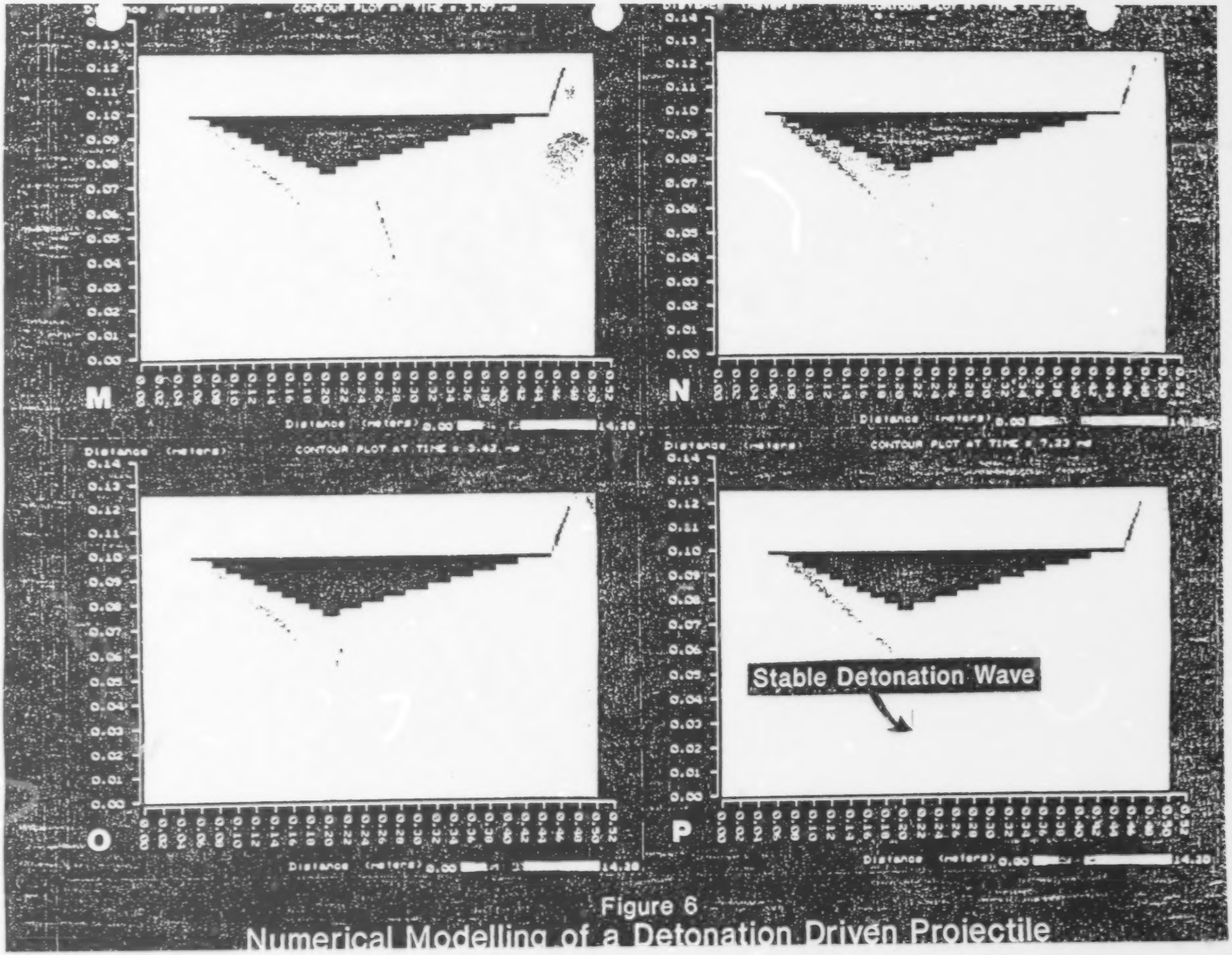

Figure 6
Numerical Modelling of a Detonation Driven Projectile

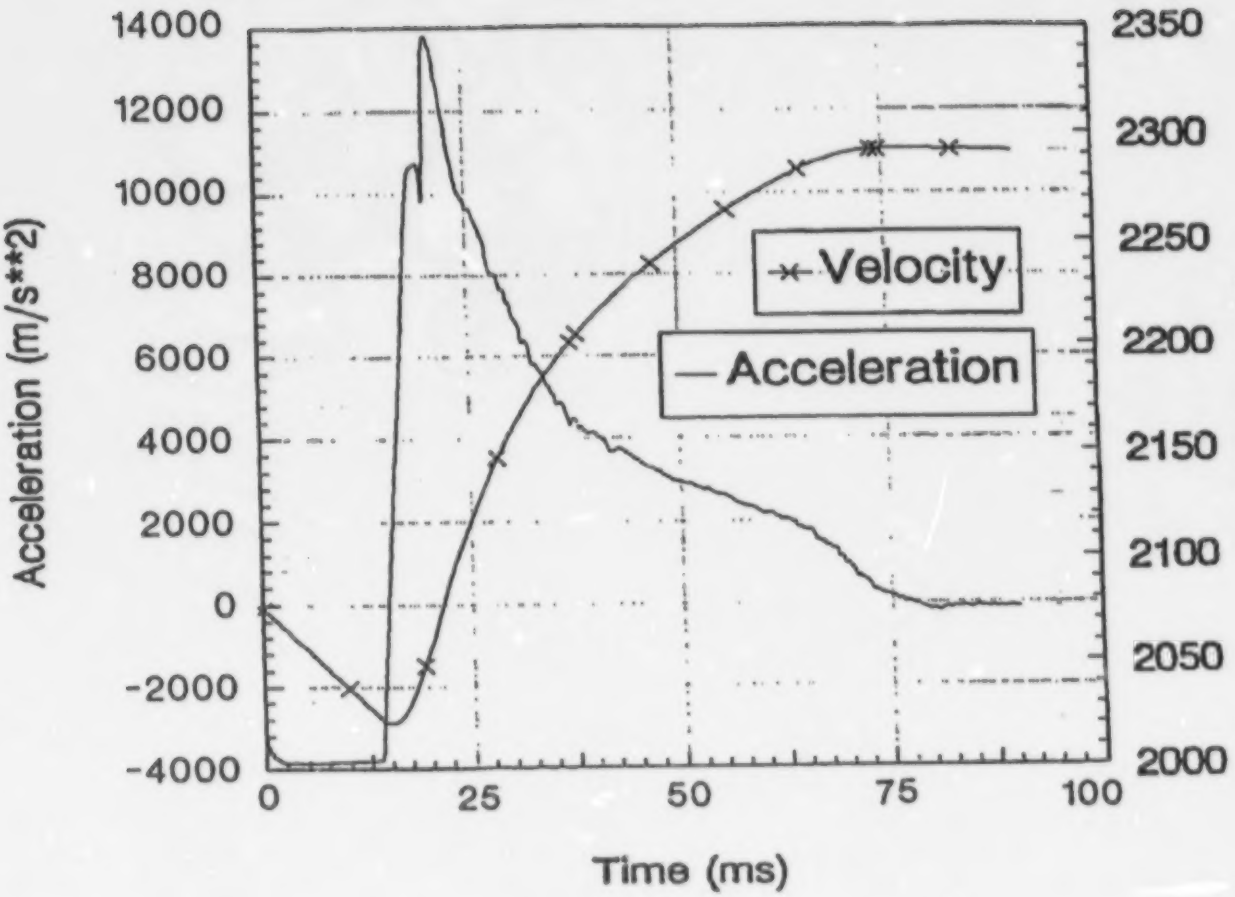

Figure 7
Calculated Acceleration and Velocity Profiles
for the Detonation Driven Projectile in Figure 5

Figure 8

CONCEPTUAL SKETCH OF SUPERSONIC COMBUSTION FACILITY

STUDIES ON DETONATION DRIVEN HOLLOW PROJECTILES

P. A. Thibault, J. D. Penrose, and A. Sulmistras

Combustion Dynamics Ltd.
203, 132 4th Avenue, S.E.
Medicine Hat, Alberta T1A 8B5, Canada

S. B. Murray and J. L. D. S. Labbé

Defence Research Establishment Suffield
Box 4000
Medicine Hat, Alberta T1A 8K6, Canada

ABSTRACT

This study explores the concept of a detonation driven projectile by performing CFD computations for a simple hollow projectile propelled in a pre-mixed detonable mixture. The particular projectile selected for the calculations has a 203 mm outer diameter and is propelled in a stoichiometric acetylene-air mixture at atmospheric pressure. The calculations model the experiments that will be performed at DRES using a 203-mm diameter, 55-caliber gun to fire the hollow projectile, and a long 2-m diameter thin plastic bag to contain the pre-mixed combustible mixture.

Fully transient inviscid 2-D computations, performed with a simple one-step combustion model, indicate that a detonation front can be stabilized in the projectile nozzle for an appropriate choice of projectile geometry and inlet Mach number. The detonation structure inside the projectile is relatively complex and involves three connected detonation branches, two of which interact with the conical bow shock generated by the leading edge of the projectile. The central branch is overdriven due to the flow contraction produced by the other two oblique detonation branches. Fully coupled computations that include projectile acceleration effects indicate that the diameter of the central branch approaches a diameter of 44 mm when the projectile reaches a terminal Mach number of 6.43. Based on detonation cell size measurements for a CJ detonation, and ZND calculations for an overdriven detonation, this corresponds to a diameter to cell size ratio $D/S = 18$ which is large enough to suggest good stability properties for this branch.

J. Buckmaster et al. (eds.), Combustion in High-Speed Flows, 421–443.
© 1994 *Kluwer Academic Publishers. Printed in the Netherlands.*

1. Introduction

The development of efficient supersonic air-breathing engines will require modern techniques to mix and burn the fuel-air mixture. Due to the high flow velocities involved, these processes must be cleverly accelerated in order to minimize the overall size of the engine. Conventional SCRAM engine designs that rely on turbulence to promote mixing and combustion may not be effective in achieving complete combustion at high velocities and altitudes. These problems may be resolved by triggering flow instabilities upstream of the combustor to promote fuel-air mixing, and by burning the mixture as a detonation rather than as a turbulent flame.

The concept of using detonation combustion for supersonic engines has been discussed by numerous authors including Sargent and Gross (1960), Morrison (1978), Ostrander et al. (1987) and Atamanchuk and Sislian (1991). Many of the proposed concepts involve Oblique Detonation Wave Engines (ODWE) that rely on an oblique detonation wave to achieve positive thrust. The onset of detonation in such engines requires sufficient shock heating to ignite the combustible gas near the throat of the engine nozzle. This can be achieved using repeated shock reflection in a constant angle inlet section (Fig. 1a) or by the merging of multiple shock waves in a double angle inlet geometry (Fig. 1b). The presence of an oblique detonation has also been proposed as a possible mechanism for the "superdetonative" mode of the ram accelerator developed at the University of Washington (Hertzberg et al., 1988, and Hinkey et al., 1992). In this case, the detonation rides on the leeward side of the projectile and accelerates the latter to velocities higher than the Chapman-Jouguet detonation velocity for the mixture (Fig. 1c).

Studies related to detonation driven engines have thus far focused on oblique detonations and ram accelerators. Lehr (1972) has performed free-flight experiments of solid projectiles fired into pre-mixed mixtures. These studies have revealed a fascinating spectrum of combustion modes and instabilities. The solid projectiles used however were not conducive to producing positive net thrust and acceleration.

The purpose of the present study is to investigate a hollow projectile geometry that is propelled in an unconfined pre-mixed gas and accelerated by a stabilized detonation front inside the projectile. As illustrated in Figure 1d, the simple hollow projectile geometry consists of a short round tube with conical inlet and nozzle sections.

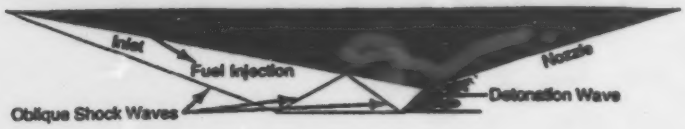

Figure 1a Oblique Detonation Wave Engine (ODWE)
Ostrander et al., 1987

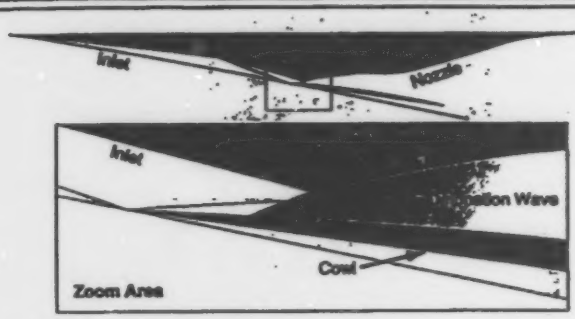

Figure 1b Hypersonic Detonation Powered Lifting-Propulsive Body
Atamanchuk and Sislian, 1991

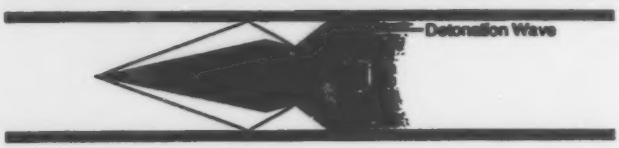

Figure 1c RAM Accelerator - Superdetonative Regime
Hinkey et al., 1992

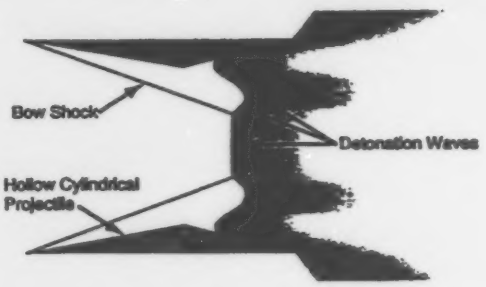

Figure 1d Detonation Driven Hollow Projectile

Figure 2a Detonation Driven Hollow Projectile
Bow Shock Implosion

Figure 2b Detonation Driven Hollow Projectile
Detonation Initiation

Figure 2c Detonation Driven Hollow Projectile
Detonation Stabilization

This geometry is essentially the ram accelerator geometry of Figure 1c turned inside out and is also similar to tubular projectiles used for artillery training (Evans and Wardlaw, 1989). This paper presents the results of a series of calculations that were performed as an initial feasibility study for large-scale experiments that will be performed at Defence Research Establishment Suffield, using a 203-mm diameter hollow projectile fired from a 203 mm - 55-caliber gun.

2. Detonation Driven Hollow Projectile Concept

The hollow projectile geometry provides many advantages over solid projectiles for self-sustained propulsion. Firstly, the flow field inside the projectile consists of a conical bow shock that implodes with increasing strength toward the axis of symmetry (Fig. 2a). As illustrated in Figure 2b, this shock focusing serves as a natural detonation initiation source when the projectile enters a combustible gas. Projectile acceleration then becomes possible when the detonation wave expands and stabilizes in the nozzle section (Fig. 2c).

2.1. Parameters related to projectile design

As with all detonation driven engine designs, the feasibility of achieving positive thrust in a hollow projectile depends on a variety of parameters associated with the mixture, the geometry, and the initial velocity of the projectile. Direct detonation initiation depends on the energy deposited by the shock implosion process, and the reactivity of the mixture. Energy focusing is controlled by the inlet angle, the inflow Mach number, and the size of the projectile. Mixture reactivity is determined by the detailed chemical kinetics, and can be quantified in terms of the detonation cell size of the mixture which decreases with increasing mixture sensitivity. Previous studies on detonation propagation and transmission suggest that the onset of detonation by an imploding bow shock becomes more probable when the projectile diameter, D, is large compared to the detonation cell size, S (Edwards et al., 1979, and Murray and Lee, 1986). The stability of the detonation front inside the nozzle may also be expected to depend on the ratio D/S and the regularity of the mixture's detonation cellular structure (Moen et al., 1986).

Even in the limit where $D \gg S$, sustained propulsion may not be possible due to an inappropriate combination of projectile geometry

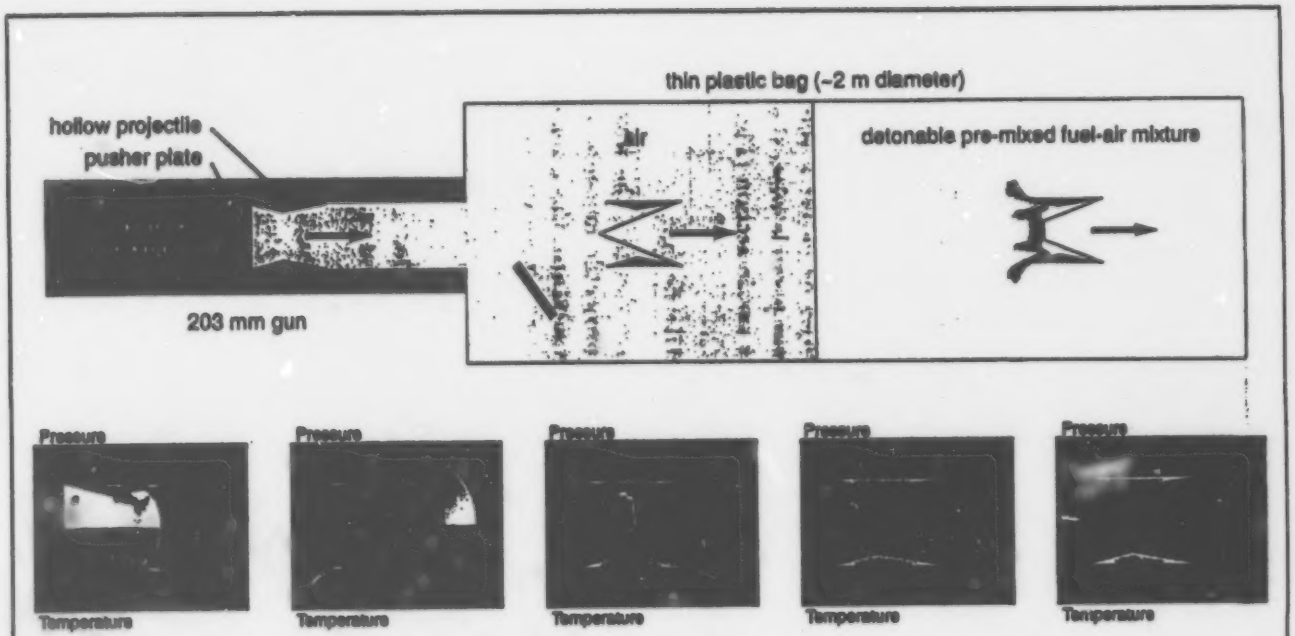

Figure 3 Detonation Driven Hollow Projectile - Proposed Experimental Configuration (DRES)
Calculation of Projectile & Pusher Plate Start-up and Shock Swallowing Process in Air

or initial velocity that can cause the detonation to either trail behind the projectile or to initiate prematurely in the inlet section. The key geometric parameters for the hollow projectile are the throat to outer diameter ratio, d/D, and the relative position of the throat, l/L. The initial inflow velocity may be characterized in terms of the ratio V_p/V_{CJ} where V_p is the initial projectile velocity and V_{CJ} denotes the Chapman-Jouguet detonation velocity for the mixture.

2.2. Parameters related to experiment design

As illustrated in Figure 3, the proposed experiments are to be performed using a 203 mm projectile that will be fired from a 203 mm - 55-caliber gun into a cylindrical bag of pre-mixed fuel-air mixture. The experiments introduce additional parameters such as the diameter of the bag which must be sufficiently large compared to the projectile diameter to eliminate any possible confinement effects of the plastic enclosure. The bag should also be sufficiently wide to accommodate the vertical displacement of the projectile due to gravity, and long enough to observe its acceleration and approach to terminal velocity. The distance required to reach this velocity is controlled by the total mass of the projectile.

The projectile will be ejected from the muzzle using a pusher plate to separate it from the burned gun propellant. The resulting flow blockage inside the projectile will produce a bow shock ahead of it as it leaves the muzzle. A sufficient free-flight distance in air must therefore be allotted for removal of the pusher plate and to allow the bow shock to be "swallowed" before the projectile enters the combustible mixture. Finally, the gun barrel will be rifled to spin the projectile and improve its aerodynamic stability.

3. Computational Method and Validation

Initial proof of concept computations were performed using a fully transient and inviscid CFD code based on the Lax-Wendroff finite difference scheme in conjunction with the 6th order (phase error) version (Book and Fry, 1984) of the Flux Corrected Transport (FCT) algorithm (Boris, 1976). The code uses a structured rectangular grid with a special slanted boundary algorithm that imposes appropriate free-slip boundary conditions on surfaces that are not aligned with the grid.

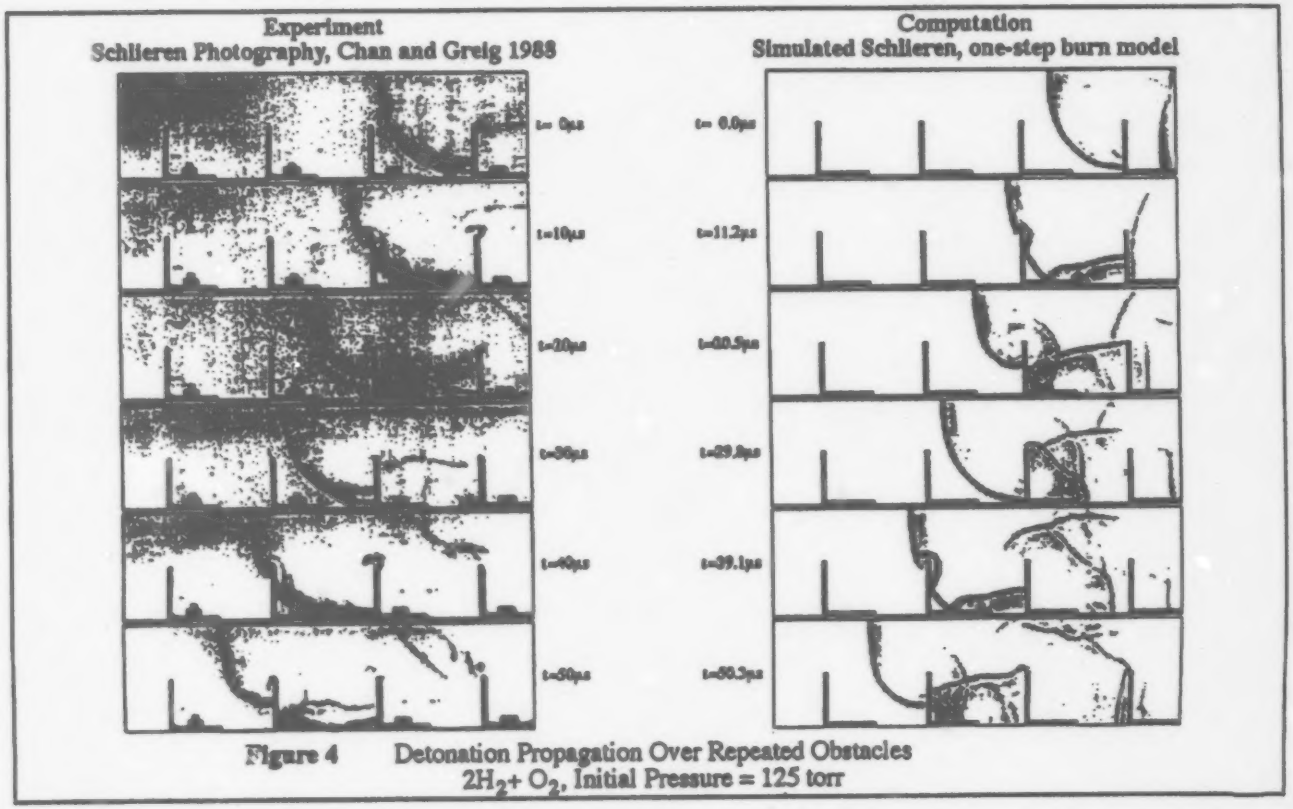

Figure 4 Detonation Propagation Over Repeated Obstacles
$2H_2 + O_2$, Initial Pressure = 125 torr

The purpose of the calculations was to follow the propagation and stabilization of the detonation wave without resolving the transverse wave structure of the detonation front or attempting to model the detailed onset of detonation initiation (or failure). As previously mentioned, the latter phenomena are intimately related to the ratio of the projectile diameter, D, over the characteristic detonation cell size, S, of the mixture. In the limit where D/S is assumed to be very large, detonation initiation and propagation are essentially guaranteed when the temperature is raised above the ignition temperature of the mixture. In this limit, the computations can be performed with a very simple reactant depletion model with a constant reaction time and a temperature threshold for ignition. During the reaction process, the chemical energy released is in proportion to the reactant depleted, and the specific heat ratio γ varies continuously from the unburned to the burned gas values. Due to the absence of a temperature dependent term, this model inhibits the onset of gasdynamic-chemical instabilities that would require a prohibitively expensive fine grid to be accurately resolved. All computations were performed using a chemical energy per unit mass, and a specific heat ratio that are consistent with chemical equilibrium computations for a Chapman-Jouguet detonation in a stoichiometric acetylene-air mixture.

The simple one-step burn model described above has been used successfully in computing the propagation of hydrogen-oxygen detonations over repeated obstacles. Figure 4 compares computational results with experiments performed by Chan and Greig (1988). The computed and experimental Schlieren images reveal excellent agreement at the detonation front. Both the detonation diffraction over the obstacles and the focusing in the bottom corners are correctly represented. The calculations clearly capture complex shock reflection patterns that are also evident, though more diffused, in the experiments. The most significant difference between the experiments and computations appears in the fourth frame where the experimental Schlieren image suggests a slight decoupling between the diffracted shock wave and the reaction front. This local detonation failure is due to the weakening of the wave as it diffracts around the obstacle. Its occurrence depends on the sensitivity of the mixture and can result in a very distinct cycle of detonation failure and reinitiation in less sensitive mixtures. Such "quasi-detonation" cycles cannot be quantitatively computed without resolving the detonation

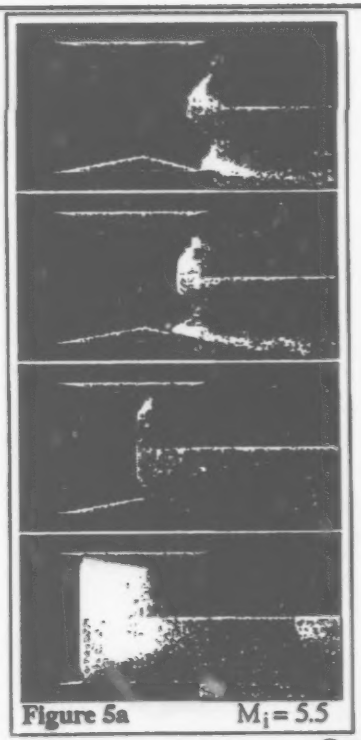

Figure 5a $M_i = 5.5$

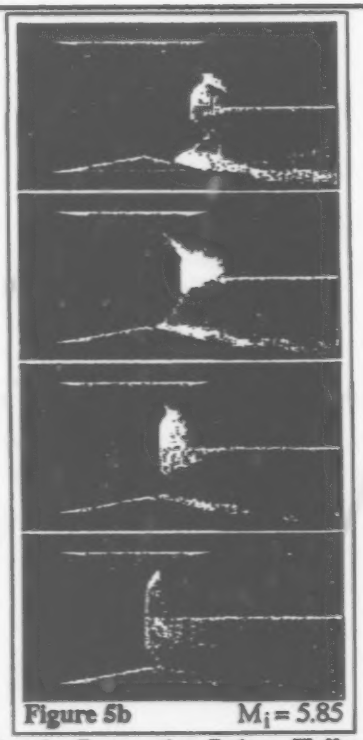

Figure 5b $M_i = 5.85$

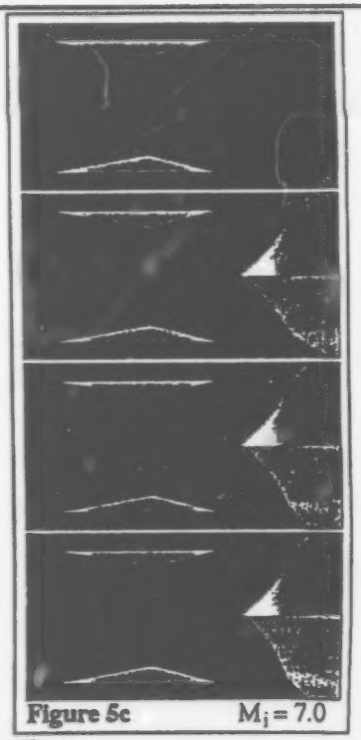

Figure 5c $M_i = 7.0$

Computation for Detonation Driven Hollow Projectile
Effect of Inflow Mach Number (d/D=0.75, l/L=0.6)

cellular structure and the turbulent flow downstream of the obstacle.

4. Computational Results

In order to investigate the effect of geometry and initial Mach number on the stabilization of the detonation front in the projectile nozzle, initial computations were performed using a resolution of 40 computation cells per projectile radius and approximately 3 cells per reaction-zone length. For a 203-mm diameter projectile, this corresponds to a resolution of 2.5 mm per computational cell. These calculations were followed by higher resolution computations with 80 cells per radius, and as many as 30 cells per reaction zone. This provided a more detailed view of the relatively complex detonation front structure. The main computational grid was surrounded by a geometrically expanding grid that contained 25 additional computational cells in both directions. This extended the grid by an additional 76 and 38 projectile radii for low and high resolution computations respectively. "Flow-through" boundary conditions were imposed at the end of the expanded grid. The entire grid was initialized to an ambient pressure, $P = 1$ atm., temperature, $T_\infty = 298.15$ K, and inflow Mach number, M_i.

4.1. Effect of Mach number

Figure 2 shows the results of the calculations with an inflow Mach number, $M_i = 5.85$ for a stoichiometric acetylene-air mixture with a CJ detonation Mach number of 5.4. In this case, the detonation is initiated along the axis of symmetry behind the projectile and propagates into the nozzle to finally stabilize near the throat. The detonation propagation process is shown in greater detail in Figure 5 which compares pressure and temperature contours for $M_i = 5.5, 5.85$ and 7. The successful engine start-up configuration for $M_i = 5.85$ (Fig. 5b) reveals a detonation front that is constructed of three connected branches. The central branch represents a normal overdriven detonation that propagates upstream along the axis of symmetry in the undisturbed region of the flow field. This branch connects to an oblique detonation that propagates in a mixture that has been precompressed by the bow shock. The third branch propagates along the nozzle wall into a low-pressure region behind the throat. The three branches move relative to each other during the overall engine start-

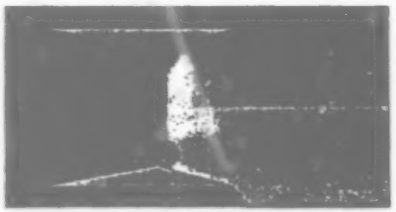

Figure 6a d/D = 0.750, l/L = 0.60
Unconfined

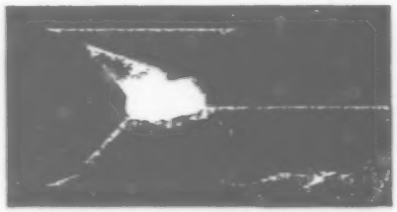

Figure 6b d/D = 0.500, l/L = 0.60
Unconfined

Figure 6c d/D = 0.875, l/L = 0.60
Unconfined

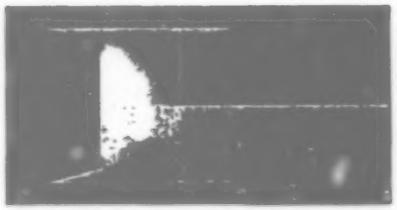

Figure 6d d/D = 0.750, l/L = 0.40
Unconfined

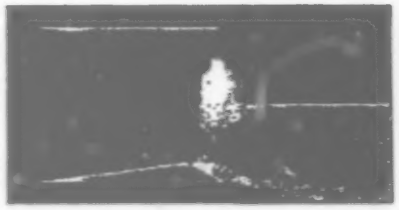

Figure 6e d/D = 0.750, l/L = 0.82
Unconfined

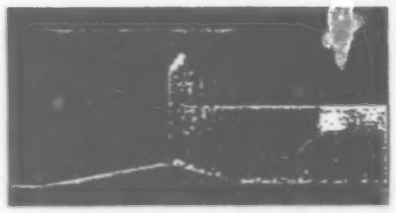

Figure 6f d/D = 0.750, l/L = 0.60
Confined in Tube

Computation for Detonation Driven Hollow Projectile
Effect of Geometry ($M_1 = 6$)

up process. The central branch initially moves ahead of the other branches until the outer branch comes in contact with the projectile wall. The latter branch then rapidly accelerates along the nozzle surface to overtake the central branch and eventually stabilizes just downstream of the throat (Frame 2). At this point, it is overtaken by the central branch (Frame 3) which stabilizes just upstream of the throat (Frame 4).

The same "seesawing" behavior between the central and outer detonation branches is observed for the case of a lower inlet Mach number $M_i = 5.5$ (Fig. 5a). In this case, however, the central detonation penetrates through the throat causing the engine to unstart. The three-branch structure is then reduced to two branches with the central branch remaining overdriven while the second branch propagates in the pre-compressed region behind the bow shock. It is interesting to note that the hollow projectile engine unstarts for an inlet Mach number that is slightly larger than the Chapman-Jouguet Mach number for the mixture. This observation is consistent with the analysis of Pratt et al. (1987) which indicates that the CJ state represents "a lower bound for possibly stable oblique detonations."

The detonation propagation sequence for a large inlet Mach number, $M_i = 7$, is displayed in Figure 5c. In this case, the detonation spreads radially from the axis of symmetry but cannot propagate upstream to provide thrust to the projectile. In a free-flight situation, the projectile would decelerate due to drag and allow the detonation to catch up.

4.2. Effect of geometry

The detonation propagation phenomena described above depend not only on the inlet Mach number but also on the internal geometry of the projectile. Even in the case of non-reacting flow, the shock structure inside the projectile depends greatly on the ratio, d/D, of projectile's throat diameter over its outer diameter. For a given inlet Mach number, there exists a minimum value of d/D below which the flow restriction causes the flow to become subsonic at the throat. This creates a detached shock upstream of the projectile and causes a sudden deceleration of a projectile in free flight (Shapiro, 1953 and Evans, 1989).

The effect of area blockage on the start up of a hollow projectile engine is displayed in Figures 6a, b, and c for an inlet Mach number

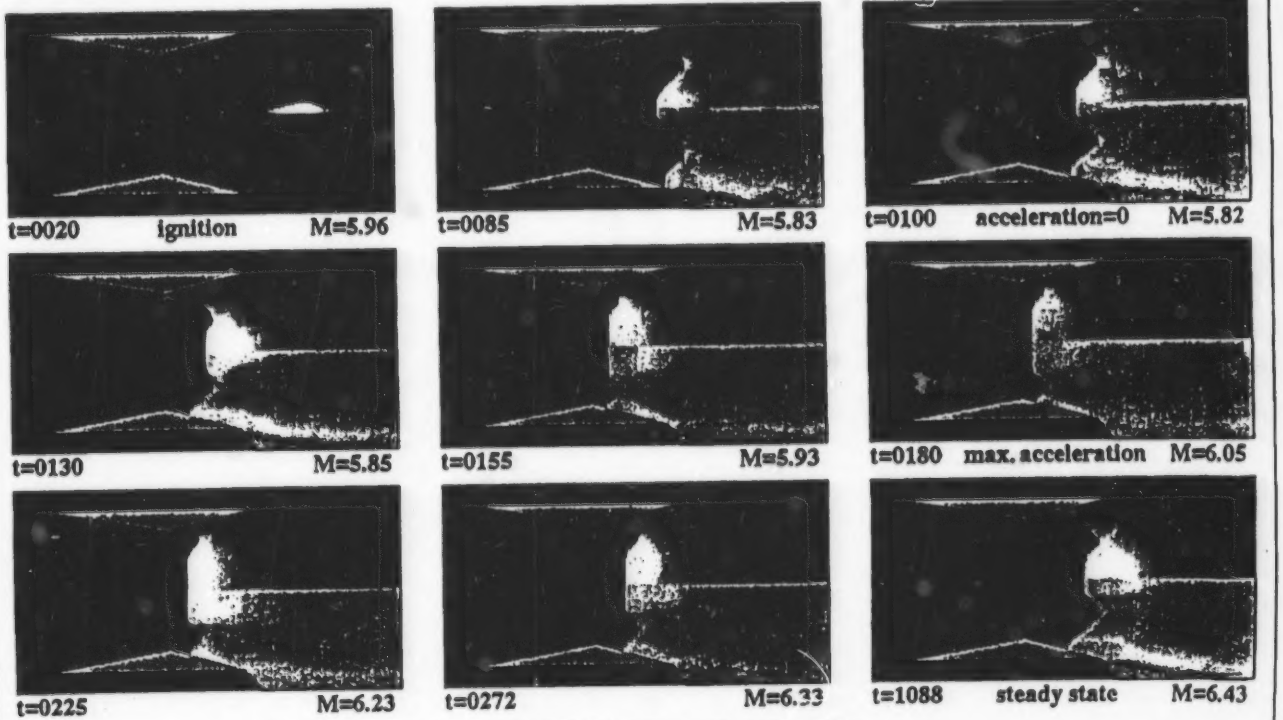

Figure 7 Fully Coupled Hollow Projectile Calculation
d/D = 0.75, l/L = 0.6, Initial Mach Number = 6

M_i = 6 and diameter ratios d/D = .75, .5 and .875. As in the previous comparison for different inlet Mach numbers, this comparison reveals a successful start up for d/D = .75, an unstart for d/D = .5, and detonation standoff for d/D = .875. The unstart condition for d/D = .5 is due to an increase in flow restriction, and to a larger inlet angle which results in a stronger bow shock and ignition upstream of the throat section. A similar unstart condition also occurs for d/D = .75 if the throat position is moved upstream (Fig. 6d). Figure 6e, on the other hand, shows that the throat position may be moved a great distance downstream without causing a standoff between the detonation and the nozzle surface. It is interesting to note that the geometries causing unstart in Figures 6b and 6d do not result in shock detachment in a "cold flow" calculation with the same initial and boundary conditions. Once again, this observation is consistent with the studies of Pratt et al. (1987) which show that the maximum turning angle is smaller for a standing oblique detonation than for an oblique shock.

The final frame in Figure 6 shows a successful start-up condition for the same projectile and inlet flow velocity as in Figure 6a with the exception that the projectile is confined to propagate in a solid tube. The confined and unconfined geometries display a very similar detonation structure. The main difference occurs downstream of the detonation front where the confined case exhibits a strong Mach disc structure.

4.3. Fully coupled computations

The above calculations have investigated various projectile configurations assuming that the projectile velocity remains constant throughout the transient flow process. An actual projectile may be expected to decelerate due to drag until the detonation front impinges on the nozzle surface. At this point, the positive net thrust will accelerate the projectile to a terminal velocity. This process is illustrated in Figure 7 which displays computational results for a fully coupled calculation that takes into account the acceleration of the projectile. Due to the long computational times involved, the approach to steady state was accelerated by using an artificially light projectile with a density 10 times less than aluminum. After an initial deceleration phase, the projectile suddenly accelerates when the detonation reaches the nozzle wall and propagates upstream to

Pressure

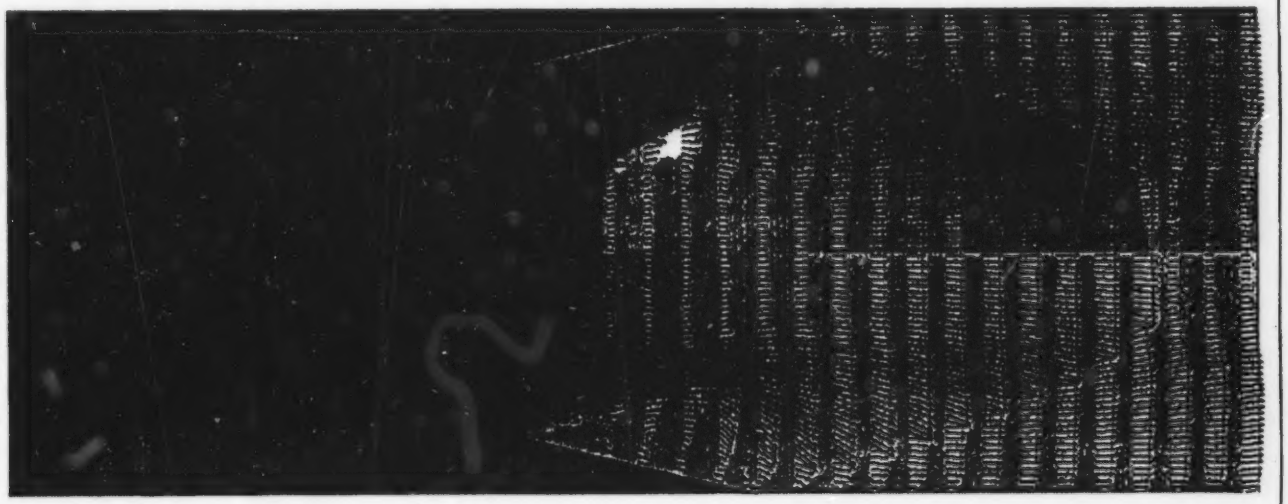

Temperature

Figure 8a Detailed Detonation Structure - Hollow Projectile Confined in Tube
$M_i = 6$, $d/D = 0.75$, $l/L = 0.6$

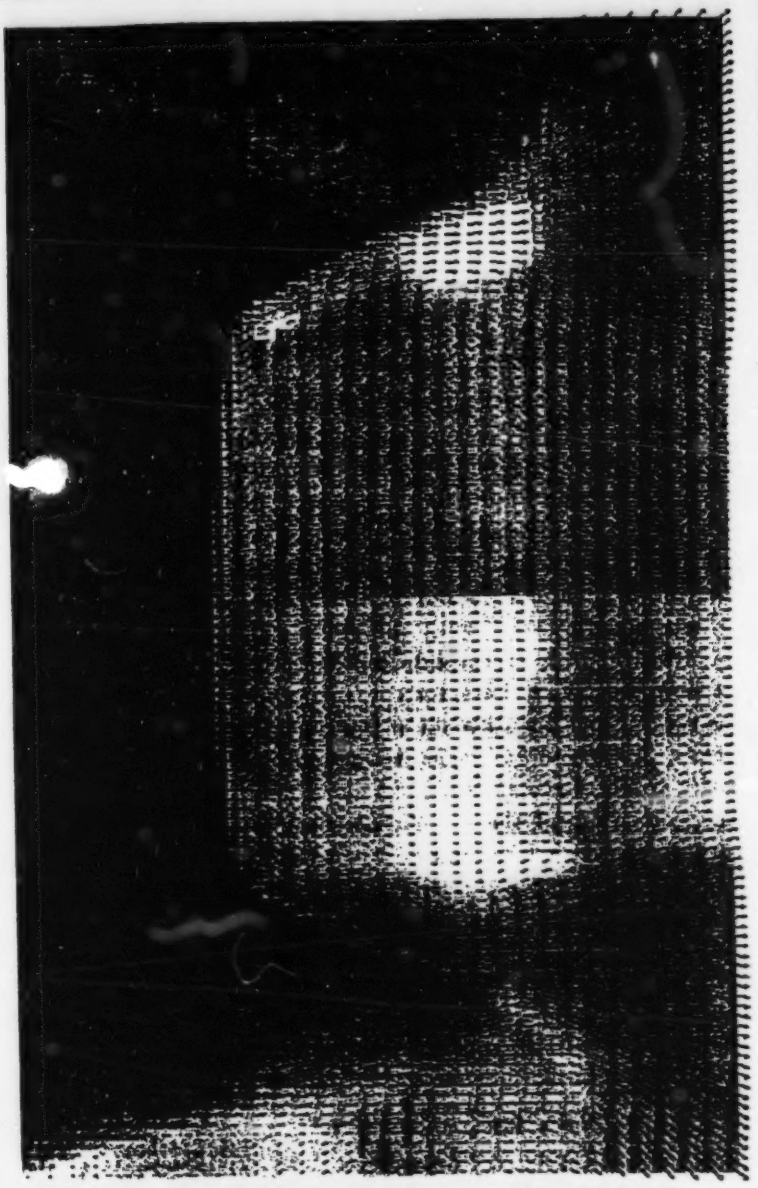

Figure 8b Detailed Detonation Structure (Zoomed Area)
Hollow Projectile Confined in Tube
$M_i = 6$, $d/D = 0.75$, $l/L = 0.6$

a position near the throat where maximum acceleration is achieved. Subsequent acceleration of the projectile then causes the detonation front to recede downstream in the nozzle. This gradually reduces the thrust surface and the acceleration until the projectile reaches a terminal Mach number of 6.43, which corresponds to an 18% overdrive of the central detonation branch.

4.4. Analysis of the detonation structure

In order to shed further light on the detonation structure in the hollow projectile, higher resolution calculations were performed for the case of a fully confined projectile with $M_i = 6.0$ and $d/D = .75$. The exothermic reaction time was also increased to further increase the number of computational cells in the reaction zone. Figure 8a displays the steady-state pressure and temperature contours overlaid on a velocity vector plot. The pressure distribution is also displayed as a 3-D carpet plot in Figure 9a. The overall flow field is characterized by a three-branch detonation front with a central and oblique detonation interacting with the imploding conical bow shock. The third detonation branch is anchored on the projectile just downstream of the throat and interacts with the oblique detonation to produce a large pressure peak at the intersection point. An underexpanded jet structure with a characteristic recompression shock and Mach disc is established downstream of the central and oblique detonation branches. A burned gas recirculating flow pattern is also produced near the nozzle surface behind the third detonation branch.

A closer view of the detonation front structure (Figs. 8b and 9b) highlights the interaction between the detonation branches and the conical bow shock. The flow behind the central detonation branch temporarily expands radially within the reaction zone and re-compresses due to the high pressure generated by the interaction of the two remaining branches. The latter "pinching" effect is responsible for the 11% velocity overdrive of the central detonation branch. The exact nature of the other two branches is more difficult to categorize due to the complex structure of the detonation front and the relatively thick reaction zone.

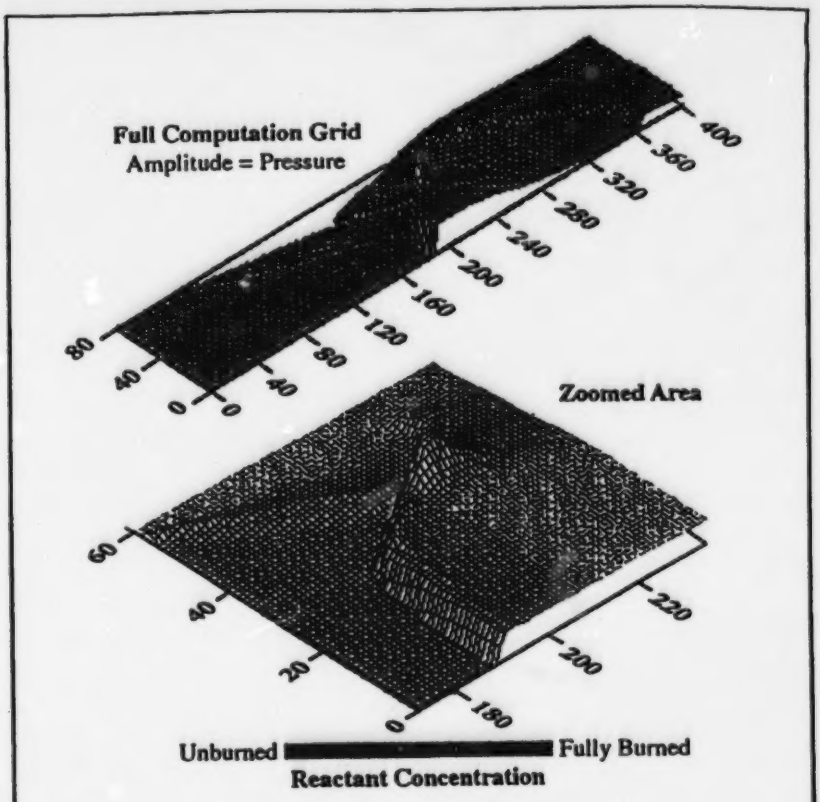

Figure 9 Detailed Detonation Structure

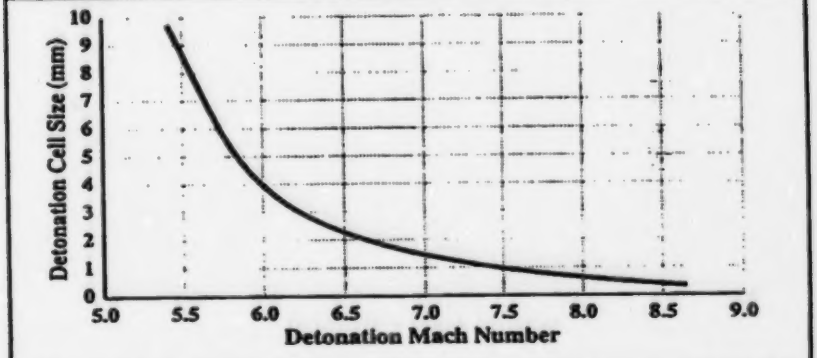

Figure 10 Detonation Cell Size Estimates - Overdriven Acetylene-Air
(Stoichiometric, Pressure = 1 atm., Temperature = 298.15 K)

4.5. Detonation cell size considerations

The above calculations have not resolved the important transverse wave structure of the three branches of the detonation front. The detonation cell size for a CJ detonation in stoichiometric acetylene-air with initial conditions P_o = 1 atm. and T_o = 298.15 K is approximately S = 10 mm (Moen et al., 1985). Due to the increase in shock pressure and temperature, the detonation cell size may be expected to decrease as the detonation becomes overdriven. The influence of overdrive on the cellular structure of fuel-oxygen detonations has been investigated by Meltzer et al. (1991), Edwards et al. (1984), and Gravilenko and Prokhorov (1982). Unfortunately, similar measurements have yet to be performed for overdriven fuel-air mixtures. In the absence of suitable experimental data, detonation cell sizes for overdriven acetylene-air detonations may be estimated on the basis of reaction-zone lengths computed using detailed kinetics and a one-dimensional ZND model. Using, as a reference point, the experimental cell size for a CJ detonation, the overdriven detonation cell size may then be computed as a function of the overdrive ratio M_{OD}/M_{CJ}. This approach assumes a constant ratio between the detonation cell size and the ZND reaction zone. Figure 10 shows the results of such an analysis based on computations performed by Shepherd (1993). These calculations indicate that the detonation cell size decreases from 10 mm to 2.4 mm for a 20% velocity overdrive. For a projectile outer diameter of 203 mm, this corresponds to a diameter to cell size ratio D/S = 85. In the fully coupled calculations displayed in Figure 7, the diameter of the central detonation branch, D_c, decreases by a factor of 2 from 88 mm to 44 mm during its acceleration to the steady-state velocity, whereas the ratio D_c/S decreases by only 22% from 23 to 18. These large ratios are certainly encouraging since they suggest that the central detonation branch will remain stable during the projectile acceleration process. More detailed computations would be required to assess the fate of the other two branches.

5. Conclusions

Numerical studies have investigated the feasibility of achieving detonation driven propulsion of a hollow tubular projectile in a premixed fuel-air mixture. The inviscid CFD computations based on a simple one-step combustion model indicate that such a concept

may indeed be feasible with the appropriate selection of a projectile geometry and an initial velocity which must be larger than the CJ detonation velocity of the mixture. The detonation structure inside the projectile is relatively complex and involves three connected detonation branches, two of which interact with the bow shock. The central branch is overdriven due to the flow contraction produced by the other two detonation branches. The flow field includes a recirculation zone near the nozzle wall which also contributes to the overall flow contraction downstream of the throat. A more accurate analysis taking into account viscous effects and turbulence will undoubtedly be required to accurately model the recirculation zone, and to investigate possible ignition in the inlet boundary layer. The combined use of adaptive gridding and detonation trackers would also be useful to explore the complex interactions between the detonation fronts, the bow shock, the recirculation zone, and the boundary layer.

Acknowledgement

The authors would like to thank Dr. J. E. Shepherd for his very helpful comments and for providing ZND reaction-zone computations that were used for detonation cell size estimates.

References

Atamanchuk, T. and Sislian, J., 1991. "Hypersonic detonation wave powered lifting-propulsive bodies," *AIAA Third International Aerospace Planes Conference*, Orlando, Florida.

Book, D. L. and Fry, M. A., 1984. "Airblast simulations using flux-corrected transport codes," Naval Research Laboratory Memorandum 5334.

Boris, J. P., 1976. "Flux-corrected transport modules for solving generalized continuity equations," Naval Research Laboratory Memorandum 3237.

Chan, C. K. and Greig, D. R., 1988. "Structure of fast deflagrations and quasi-detonations," *22nd Symposium (International) on Combustion*, p. 1733.

Edwards, D. H., Thomas, G. O., and Nettleton, M. A., 1979. "The diffraction of a planar detonation wave at an abrupt area change," *J. Fluid. Mech.* **95**, pp. 79-96.

Edwards, D. H., Walker, J. R., and Nettleton, M. A., 1984. "On the propagation of detonations along a wedge," *Archivum Combustion* **4**(3), pp. 197-209.

Evans, J. R. and Wardlaw, A. B., Jr., 1989. "Prediction of tubular projectile aerodynamics using the zeus euler code," *Journal of Spacecraft and Rockets* **26**(5), pp. 314-321.

Gravilenko, T. P. and Prokhorov, E. S., 1982. "Compressed detonation wave in a real gas," *Combustion, Explosion, and Shock Waves* **17**(6), pp. 689-692.

Hertzberg, A., Bruckner, A. P., and Bogdanoff, D. W., 1988. "Ram accelerator: A new chemical method for accelerating projectiles to ultrahigh velocities," AIAA Journal **26**(2), pp. 195-203.

Hinkey, J. B., Burnham, E. A., and Bruckner, A. P., 1992. "High spatial resolution measurements of ram accelerator gas dynamic phenomena," *AIAA/SAE/ASME/ASEE 28th Joint Propulsion Conference and Exhibit*, Nashville, Tennessee, AIAA 92-3244.

Lehr, H. F., 1972. "Experiments on shock-induced combustion," *Astronautica Acta* **17**, pp. 589-597.

Meltzer, J., Shepherd, J. E., Akbar, R., and Sabet, A., 1991. "Mach reflection of detonation waves," *13th ICDERS*, Nagoya, Japan.

Moen, I. O, Funk, J. W., Ward, S. A., Rude, G. M., and Thibault, P. A., 1985. "Detonation length scales for fuel-air explosives," *Progress in Astronautics and Aeronautics* **94**.

Moen, I. O., Sulmistras, A., Thomas, G. O., Bjerketvedt, D., and Thibault, P. A., 1986. "The influence of cellular regularity on the behavior of gaseous detonations," *Progress in Astronautics and Aeronautics* **106**, pp. 220-243.

Morrison, R. B., 1978. "Evaluation of the oblique detonation wave ramjet," Universal Systems Inc., NASA CR NAS1-14771.

Murray, S. B. and Lee, J. H., 1986. "The influence of physical boundaries on gaseous detonation waves," *Progress in Astronautics and Aeronautics* 106, p. 325.

Ostrander, M. J., Hyde, J. C., Young, M. F., Kissinger, R. D., and Pratt, D. T., 1987. "Standing oblique detonation wave engine performance," Aerojet TechSystems Co., PRA-SA-AFAL, published by the American Institute of Aeronautics and Astronautics Inc.

Pratt, D. T., Humphrey, J. W., and Glenn, D. E., 1987. "Morphology of a standing oblique detonation wave," *Colloquium on Supersonic Combustion, AIAA/ASME/SAE/ASEE 23rd Joint Propulsion Conference*, Paper No. AIAA-87-1785.

Sargent, W. H. and Gross, R. A., 1960. "Detonation wave hypersonic ramjet," *ARS Journal.*

Shapiro, A. H., 1953. "The dynamics and thermodynamics of compressible fluid flow, Volume 1," John Wiley and Sons.

Shepherd, J. E., 1993. Private communication.

CFD MODELING OF FLUID-STRUCTURE AND LIQUID-GAS INTERACTIONS

Tran, D., Link, R., Penrose, J., and
Thibault, P.A.
Combustion Dynamics Ltd.,
132 - 4th Avenue S.E.
Medicine Hat, Alberta, Canada T1A-8B5

Abstract

Purpose: To develop an approach to model fluid-structure and fluid-gas interaction problems.
Methods: An explicit Lax-Wendroff FCT Eulerian finite difference model is used to compute fluid and gas motion. An explicit Lagrangian finite element code is adopted to calculate the structural response. A Riemann solver is used to compute the solution variables at the interface between different media, and ensure free slip conditions at the boundary. The proposed formulation is used to analyze the case of a shock propagating through water contacting a cylindrical object. Three cases of cylinder material composition are analyzed; rigid solid, deformable shell filled with air, and air bubble.
Results: Comparison of peak reflected pressures shows that the rigid solid sustains the highest reflected pressure, and the air bubble sustains the lowest, which is consistent with expected results. Shock wave transmission through the air in the deformable solid and air bubbles was evident. The transmission of the shock wave through the deformable shell caused reflection of a rarefaction wave at the front, and a compression wave in back. The air bubble case sent back a rarefaction wave, which again is consistent with expected results.
Conclusions: A mixed Eulerian-Lagrangian technique is presented here to solve fluid/solid and fluid/interface interaction problems. Calculations performed on the above three test problems yielded very distinct wave reflection and transmission characteristics which were consistent with expected behavior.

Introduction

Many engineering problems involve material interfaces that pose a serious challenge for CFD modeling. In the simplest case, the interfaces separate materials of the same phase, with different densities and thermodynamic properties. The more difficult problems involve materials of different phases characterized by very distinct equations of state. In the case of fluid-structure interactions, the problem is further compounded by the fact that completely different numerical schemes are often preferred for the fluid and structural calculations.

A flexible approach to the above problem is to develop front tracking techniques that can be adapted to a wide range of materials and numerical descriptions. A number of interface construction techniques have been developed that rely on artificial "mixture" rules between the various materials [1], [2]. A serious drawback of these rules is that free slip between materials is not allowed. A more accurate approach involves the use of front trackers [3], [4] that truly separate the materials without the use of mixture rules. Such techniques are used in this paper.

This paper presents 2-D numerical calculations for problems involving interfaces between gas, water, and solid materials. These include shock transmission through water over a rigid solid cylinder, a deformable solid shell, and an air bubble. The fluid and gas flow is modeled using a Lax-Wendroff/FCT algorithm by solving the Euler equations on a fixed grid. The deformable solid shell is modeled using an explicit Lagrangian finite element formulation. The material interfaces are resolved as sharp discontinuities that can be "slanted" with respect to the underlying grid, and Riemann solvers are used to solve the wave transmission problem while maintaining free slip conditions along the interface.

Methods

CFD Calculation

Governing Equations

The calculations presented in this paper assume the flow to be inviscid and compressible. The air obeys the ideal gas law with a constant specific heat ratio, whereas the water is modeled using Tait and modified Tait equation of state. Based on these assumptions, the governing equations for the two fluids may be written as follows:

Air:

The gas phase obeys the following Euler equations for mass, momentum, and energy for a Cartesian coordinate system:

$$\frac{\partial \rho}{\partial t} + \frac{\partial \rho v_x}{\partial x} + \frac{\partial \rho v_y}{\partial y} = 0 \qquad [1]$$

$$\frac{\partial \rho v_x}{\partial t} + \frac{\partial \rho v_x^2}{\partial x} + \frac{\partial \rho v_x v_y}{\partial y} = -\frac{\partial p}{\partial x} \qquad [2]$$

$$\frac{\partial \rho v_y}{\partial t} + \frac{\partial \rho v_x v_y}{\partial x} + \frac{\partial \rho v_y^2}{\partial y} = -\frac{\partial p}{\partial y} \qquad [3]$$

$$\frac{\partial \rho e}{\partial t} + \frac{\partial \rho e v_x}{\partial x} + \frac{\partial \rho e v_y}{\partial y} = -\left[\frac{\partial p v_x}{\partial x} + \frac{\partial p v_y}{\partial y}\right] \qquad [4]$$

where p and ρ are pressure and density, and v_x and v_y denote the velocity components in the x and y directions, respectively. The energy density, e, for an ideal gas follows the equation

$$e = \frac{p}{\rho(\gamma - 1)} + \frac{1}{2}(v_x^2 + v_y^2) \qquad [5]$$

where γ is the specific heat ratio.

Water:

The water follows the same mass and momentum equations (1-3) as for air, but does not require an energy equation, since the pressure is solely a function of the density through the Tait and modified Tait equations of state [5], written as:

$$\text{Tait: } \frac{p}{p_0} = \left(\frac{B}{p_0}\right)\left[\left(\frac{\rho}{\rho_0}\right)^n - 1\right] + 1 \text{ for } \frac{\rho}{\rho_0} \geq 1 \qquad [6]$$

$$\text{Modified Tait: } \frac{p}{p_0} = \left(\frac{\rho}{\rho_0}\right)^m \text{ for } \frac{\rho}{\rho_0} < 1 \qquad [7]$$

where p_0 and ρ_0 are pressure and density at standard conditions, taken as 1 atm and 1000 kg/m^3, respectively. The quantities B, n, and m are constants that are taken as 3010 atm, 7.14, and 21457.15 respectively.

Solution Method

The above equations are solved using a fixed Cartesian grid, and a front tracker for the solid-water or gas-water interfaces. The finite difference approach is based on the explicit Lax-Wendroff algorithm, which is used in conjunction with the 6th order (phase error) version [6] of the Flux Corrected Transport (FCT) scheme [7]. The 2-D solution is constructed using a "split" approach which uses separate sweeps in the x and y directions. The front tracker follows the motion of the interface through the grid, and can resolve displacements that are much smaller than the Cartesian mesh size. As illustrated in Figure 1, the method maintains free-slip conditions in the direction tangent to the interface, and solves a Riemann problem in the normal direction. The integration of the interface tracker with the CFD and solid response code is discussed in a later section.

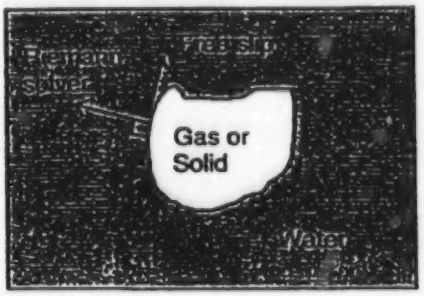

Figure 1 Problem illustration

Solid Calculation

In the solution of thin shell fluid-structure interaction problems, it is often desirable to adopt a Lagrangian frame of reference for the thin shell. This is because it is difficult to track the material advection for the shell in an Eulerian reference frame.

Governing Equations

In the Lagrangian solid problem, the momentum equation is solved for a specified set of boundary conditions. The solids problem can be written in a weak form as:

$$\int_V \rho \ddot{x} \delta x_i dV = \int_{S_\sigma} T_i \delta x_i dS + \int_V \rho f_i \delta x_i dV - \int_V \sigma_{ij} \delta x_{i,j} dV \qquad [8]$$

subject to the boundary conditions

$$\sigma_{ij} n_j = T_i(t) \text{ on } S_\sigma \qquad [9]$$

where ρ is the material density, σ_{ij} is the internal stress tensor, S_σ is the boundary where surface tractions are applied, T is the applied surface traction, n represents the normal to the boundary of S_σ, x is the current spatial position, f are body forces per unit mass (e.g. gravity, spin), δx refers to an arbitrary variation in position, and V refers to the body volume. Physically, the term on the left hand side of Equation 8 represents the inertia forces in the body, and those on the right hand side represent forces due to surface tractions, body forces, and internal stresses.

Solution Method

Closed form solutions for Equation 8 only exist for very simple problems. It is therefore necessary to solve the equations using numerical methods. The finite element method is used here because of its ability to handle non-regular mesh types. Equation 8 can be rewritten in terms of discrete (nodal) points as follows:

$$[M]\{\ddot{x}\} = \{T\} + \{B\} - \{S\} \qquad [10]$$

where [M] is a mass matrix, and {T}, {B}, and {S} are surface traction, body, and internal stress forces respectively. If a lumped mass system is used, the mass matrix is diagonal, and an explicit solution form can be used. This is necessary in order to maintain high speed on the structural calculations. A central difference scheme is used here to advance the solution from time t^n to time t^{n+1} [8]. It is briefly described as follows:

1) Calculate T and S forces. The surface tractions are obtained from the CFD segment. The stresses are computed from the strains assuming linear elastic behavior i.e.

$$\sigma = E\varepsilon \qquad [11]$$

where ε is the axial strain in a given shell segment, and E is the material Young's modulus. In this paper, shell segments are considered to be linear pieces.

2) Accelerations are calculated by dividing the right hand side of Equation 10 by the nodal masses.

3) The acceleration is integrated to give the velocity at $t^{n+1/2}$.

4) The velocity is integrated to give the displacement at t^{n+1}.

5) The strains and stresses in the shell segments are computed, now that the incremental motion of the nodes is known.

6) A new time step is computed based on the sound speed, c, of the shortest shell segment, given by

$$c = \sqrt{\frac{E}{\rho}} \qquad [12]$$

Integration of Solid and Fluid Codes

Figure 2 shows the overall flow used in the calculation procedure. It is assumed in this study that the shock propagates through the fluid media first, although this is not necessarily the case.

The computation starts with the assignment of fluid boundary conditions, which is performed in the Riemann solver portion of the interface tracker. Next, the fluid boundary conditions are used by the CFD computational module, which solves the inviscid Euler equations, and calculates particle densities, pressures, and velocities. At this point, the problem is checked to determine whether a deformable solid exists. If a solid exists, the pressures at the solid boundary are sent to the solid response module, where the boundary velocities and positions are updated by solving the equations of motion for the solid. The fluid state variables at or near the boundary are used by the material tracker portion of the interface tracker. This module updates the position and state of fluid and/or gaseous material on the computational grid.

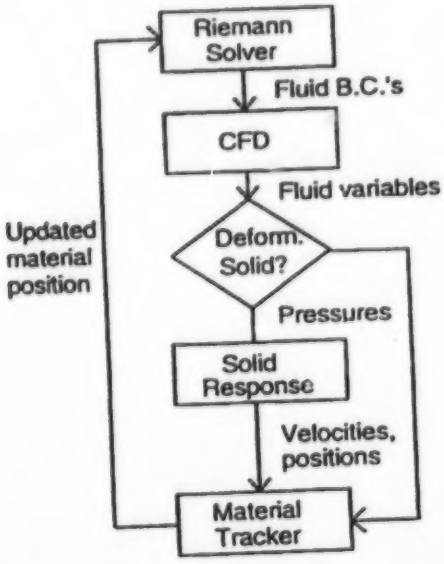

Figure 2 Calculation flowchart

Riemann Solver Calculation

The Riemann solver used here has many desirable features. The solver can accommodate slanted boundaries, and therefore ensure free-slip conditions along the boundary. This eliminates the problem of "stair casing", which is prevalent in earlier CFD codes. In addition, the solver is implicit and exact, therefore ensuring stability and accuracy of the solution.

Three different material interface conditions are considered in this study:

1) Water/rigid solid
2) Water/air and deformable shell
3) Water/air

For the water/air case, the boundary conditions at the interface are determined on the basis of conditions at cells lying on both sides of the interface along the normal. The solver determines the pressure and velocity of the interface, from which the density of each medium can be computed from the knowledge of the wave condition (expansion or shock).

For the water/rigid solid case, the boundary normal velocity is set to zero. Pressure and density of the water is then computed.

The deformable solid adds one more complication to the rigid solid case. The wall velocity is incorporated in the solution. If the wall moves in a direction opposite the water flow, the resultant pressure is larger than that developed by the rigid solid object. Conversely, if the wall moves away from the water, the pressures become lower than that of the surrounding flow, and cavitation is possible.

Material Tracker Calculation

At the end of a given time step, the location of the material interface is updated through the use of a first order interface tracker. The interface is linearly interpolated using the Eulerian computational grid as reference points. The position of the material interface is updated in a

similar way for both water/air and water/air/deformable shell interfaces. Interface velocities are integrated over the current time step to obtain the new position. Once the interface position has been determined, the redistribution of materials is ascertained, and the properties of any changed cells is computed.

Results

Figure 3 shows the analysis problem considered here. A cylindrical shape is submerged in water, and subjected to an absolute incident shock of 5 atm. The ambient conditions for the water were at 1 atm pressure and 298° K. Three different calculations were performed:

1) Fixed rigid cylinder.
2) Thin deformable shell filled with air.
3) Air bubble.

The ambient conditions for the air were identical to the ambient conditions for water. The shell thickness, density, and Young's modulus were 0.0003m, 7770 kg/m^3, and $2.0x10^{11}$ Pa respectively for Case 2. The boundary conditions on the horizontal edges of the grid were set as perfectly reflective. The CFD grid resolution was 120x90 cells, and the thin deformable shell resolution was 200 elements around the circumference.

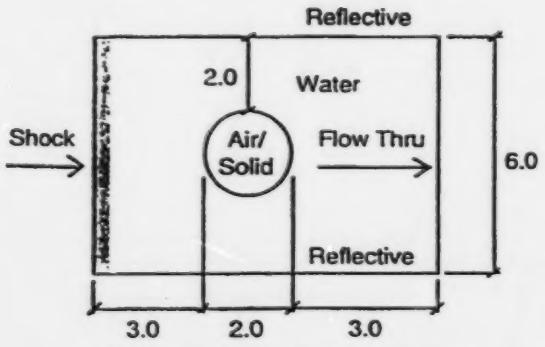

Note: All dimensions in metres

Figure 3 Calculation geometry

Figures 4a-c are carpet plots of pressure for the three cases at a time of 1100 microseconds, and Figures 5a-c are profile plots of pressure through the center of the cylinder. The fixed rigid cylinder reflects a shock wave, as evidenced by Figures 4a and 5a. The peak pressure reached at the front of the cylinder was computed as 8.60 atm., which is below the theoretical value of 9.00 atm. The lower pressure is probably due to a lack of resoulution in the calculation.

From investigation of Figures 4b and 5b, it is evident that the thin deformable shell reflects a rarefaction wave in the cylinder front, and generates a compression wave in the cylinder back. The shell is relatively thin, and the air is of significantly different acoustic impedance than the water. These two factors combine to create sufficient movement at the front to produce a rarefaction wave. The compression wave at the back is created by shock transmission through the solid. When the water shock contacts the cylinder front, a compression wave is sent through the cylinder. This causes movement throughout the cylinder in the vicinity of the shock front. When the wave reaches the cylinder back, this region is forced to move in the shock direction. This resultant movement causes the compression wave.

It is seen from Figure 4b that there are pressure "spikes" at the cylinder front. This may be due to localized shell deformation. As the shock acts on the front of the shell, some portions of the shell may develop a small negative velocity component in the x or y direction. This causes a negative change of the water particle velocity at the interface, and consequently results in a small, local density increase in the water. Because of the low compressibility of the water, considerable pressure amplification can be induced by this slight density increase. It is uncertain at this time whether the "spikes" are real, or a result of numerical instability.

Figures 4c and 5c show the development of a rarefaction wave in the air bubble that is significantly different than that of the deformable shell. The slope of the rarefaction wave is steeper. This is because the air bubble has a massless, fully compressible interface, allowing greater movement

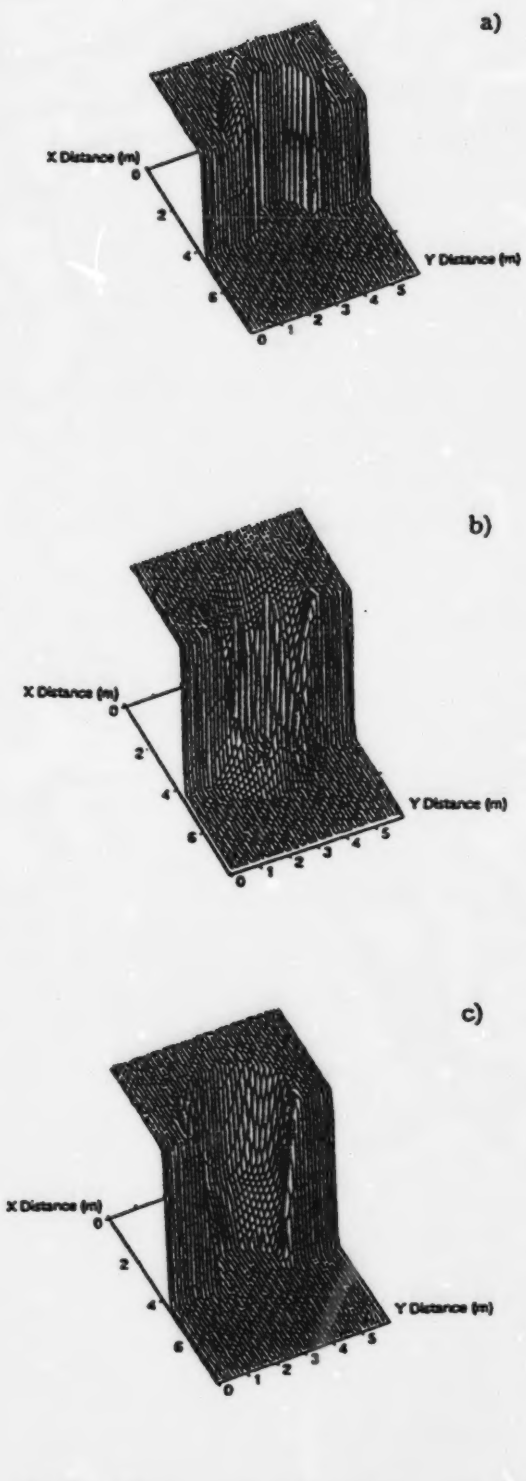

Figure 4 Pressure plots of analysis cases

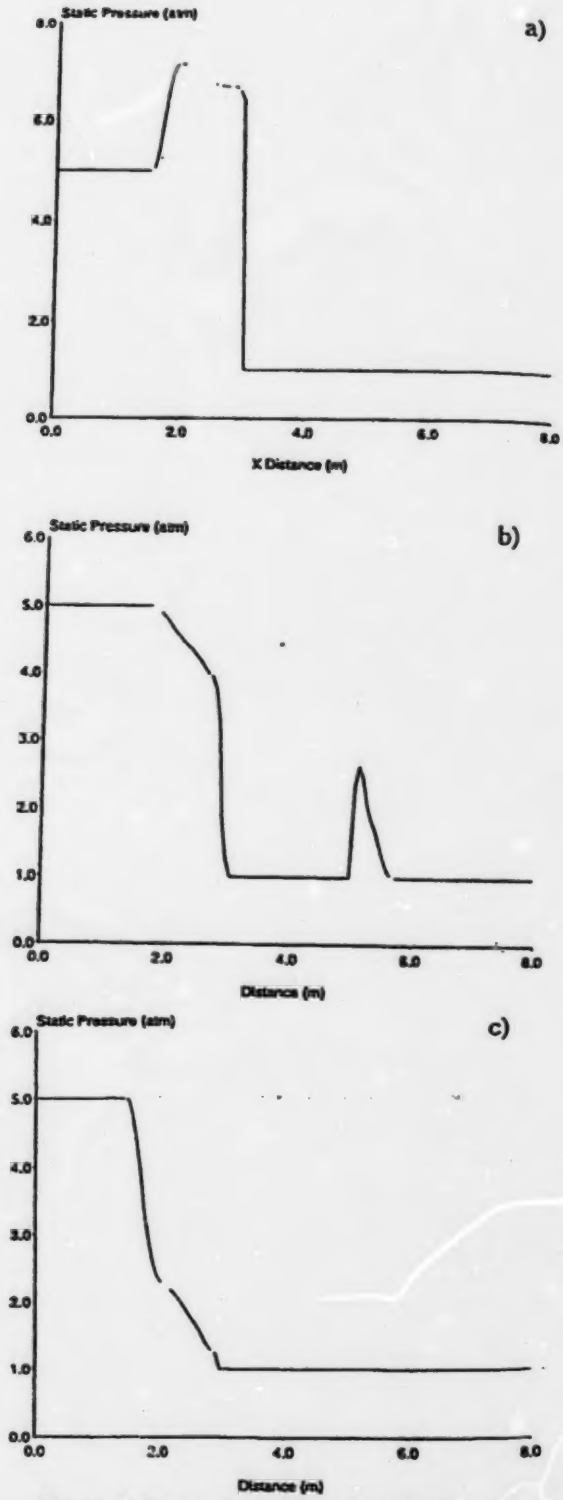

Figure 5 Pressure profiles of analysis cases

than the deformable shell, and hence a much sharper rarefaction wave.

To summarize, the three cases analyzed display shock wave transmission characteristics which are consistent with expected behavior.

Summary and Conclusions

This paper has presented an Eulerian-Lagrangian technique to solve fluid-structure and fluid-interface interaction problems. The main components of the scheme include:

1) An explicit finite difference Lax-Wendroff/FCT scheme that computes the fluid flow on an Eulerian grid.

2) An explicit finite element Lagrangian technique for the solid response calculation.

3) A front tracker that monitors the solid (or interface) position, and maps it onto the Eulerian grid.

4) An exact Riemann solver that computes the new boundary conditions in the fluid calculations.

Calculations were performed on three test problems involving a flat shock in water which interacts with a rigid cylinder, a deformable cylindrical shell filled with air, and a cylindrical air bubble. Due to the differences in density (and acoustic impedance) between the various materials, the three problems are characterized by very distinct wave reflection and transmission patterns that are clearly captured in the calculations . The proposed approach offers the following advantages over conventional front trackers based on mixture rules:

1) The "slanted boundary" algorithm allows free slip along interfaces not aligned with the Eulerian grid.

2) The exact Riemann solver can be applied to a wide variety of materials without any changes to the underlying algorithm.

Further improvements would also be required to fully exploit this technique, and improve its accuracy. These include:

1) The front tracker does not currently allow for major changes in the interface shape and topology. In particular, further enhancements are required to accommodate interface rupture and merging.

2) Although the Eulerian finite difference and Lagrangian finite element algorithms are second order accurate, the interface algorithm remains first order.

3) The accuracy of shock reflection and transmission calculations could be improved considerably by combining the interface tracker with available shock tracking techniques.

4) Investigation of the stability of the modified Tait equation of state should be performed to determine whether localized pressure oscillations are due to numerical instability.

Fluid-structure interaction problems that simultaneously involve a gas, a liquid, and a solid remain challenging due to the large differences in sound speed between the materials. In an explicit code, this results in large differences in the time step criteria for numerical stability. Furthermore, any numerical instability at an interface separating a solid and water can be greatly amplified due to the low compressibility of the water which is characterized by a very stiff equation of state. Consequently, the distinction between real physical oscillations and numerical instabilities must be clarified through numerical sensitivity analyses and code validation experiments.

References

[1] Noh, W.F., and Woodward, P. (1976). SLIC (Simple Line Interface Calculation). Lecture Notes in Physics, v. 59, Springer, Berlin.

[2] Youngs, D.L. (1987). An interface tracking method for a 3-D Eulerian hydrodynamics code. AWRE Design Mathematics Division, AWRE/44/92/35.

[3] Chern, I.L., Glimm, J., McBryan, O., Plohr, B., and Yaniv, S. (1986). Front tracking for gas dynamics. Journal of Computational Physics, v. 62, pp. 83-110.

[4] Charrier, P., and Tessieras, B. (1986). On front-tracking methods applied to hyperbolic systems of nonlinear conservation laws. SIAM J. Numerical Analysis, v. 23, No. 3, pp. 461-472.

[5] Hains, F.D. (1983). Fluid-structure interaction by the method of characteristics. Shock and Vibration Bulletin, Naval Research Lab, Washington, D.C., v. 53, pp. 23-32.

[6] Book, D.L., and Fry, M.A. (1984). Airblast simulations using flux corrected transport codes. Naval Research Laboratory Memorandum 5334.

[7] Boris, J.P. (1976). Flux corrected transport modules for solving generalized continuity equations. Naval Research Laboratory Memorandum 3237.

[8] Hallquist, J.O. (1983). Theoretical manual for DYNA3D. Report No. UCID-19401, Lawrence Livermore Laboratories.